Università degli studi di Padova

DIPARTIMENTO DI INGEGNERIA DELL'INFORMAZIONE

Corso di Laurea Magistrale in Ingegneria Elettronica

Optimization of HIT solar cell

Supervisors:

Dr. Prof. Andrea Cester
Dr. Prof. Nils Peter Harder

Candidate:

Michael Corazza

Co-examiner:

Dr. Prof. Fabrizio Dughiero

Academic year 2012-2013

Abstract

This thesis focuses on the optimization of silicon heterojunction (SHJ) solar cells. The main investigation regards hydrogenated amorphous silicon (a-Si:H) layer depositions and their influence on the solar cell performance. Therefore SHJ solar cells with different deposition parameters for the a-Si:H layers were fabricated and analysed in this work.

We find that the thickness of the intrinsic and (p)-doped a-Si:H layers deeply influences the quality of passivation and the transport properties. An optimal (i)a-Si:H thickness of 8.7-15 nm has been found for textured surfaces and for (p)a-Si:H. We find optimal gas flux parameters for the deposition of the (p)a-Si:H layer. We present a rough model to calculate the conductivity of the (i)a-Si:H layer. We find that these conductivities are injection dependent. The model also allows us to calculate the (excess) carrier concentration in the (i)a-Si:H layers.

We observe that an H_2 plasma post treatment does not improve the passivation quality of our cells and that an HF treatment does not exclude oxygen bondings in the amorphous silicon network.

Acknowledgements

First of all, I would like to thank my supervisors and co-supervisor: Prof. Dr. Nils Peter Harder, Prof. Dr. Andrea Cester and Dr. Ralf Gogolin, for their guide and suggestions. Their skills and attitude will always be an example for my professional future.

I would like to thank my family for allowing me to pursue my life goals and for the support during tough moments, without their help this achievement would have been hardly accomplished.

In addition, I would like to thank everyone else being close to me during my life at the university and during the writing of the thesis. I'd like to mention my closest friends and colleagues Sergio, Alessandro, Martina and Matteo, for the time spent both studying together but also for the great night spent having fun. I sincerely thank Madison because of what she meant to me.

Contents

1

Introduction

Solar energy is one of the most promising field for renewable energy production in the future. Sun is an endless[1] energy source which provides on Earth much more energy than the total amount of electrical energy consumed in the world.
Despite the great potential of this field many problems must still be solved:

- limited surface available for cell installations, related with cell efficiency;
- supply and cost of materials;
- time production of the cells;
- smart store of energy produced.

We search for an opportunity to make solar cells more efficient and/or cheaper. One approach to reach this goal is the Silicon HeterosJunction (SHJ) solar cell. In particular we use a type of solar cells called "HIT" (Heterojunction with Intrinsic Thin layer) cell [23] which are produced by Sanyo. This cell concept uses a crystalline silicon substrate whereas the emitter as well as the Back Surface Field (BSF) are realized with hydrogenated amorphous silicon (a-Si:H) layers.

This cell is relative new as can been seen in Figure 1.1. In the graph the best research-cell efficiency are shown in function of time, for the past 35 years.
HIT cells are represented with blue circles. Sanyo is the leader in this field and all the best results belong to its work. The first marked result in 2001 shows an efficiency above 20 %, which has been improved to 23 % in 2009. Some parameters of the best solar cell are shown in tab. 1.1 [23].

[1] At least for reasonable forward future.

Table 1.1: The best HIT solar cell.

V_{OC} [V]	J_{SC} [mA/cm^2]	FF	Efficiency	c-Si Thickness [μm]
0.729	39.5	0.8	23 %	> 200

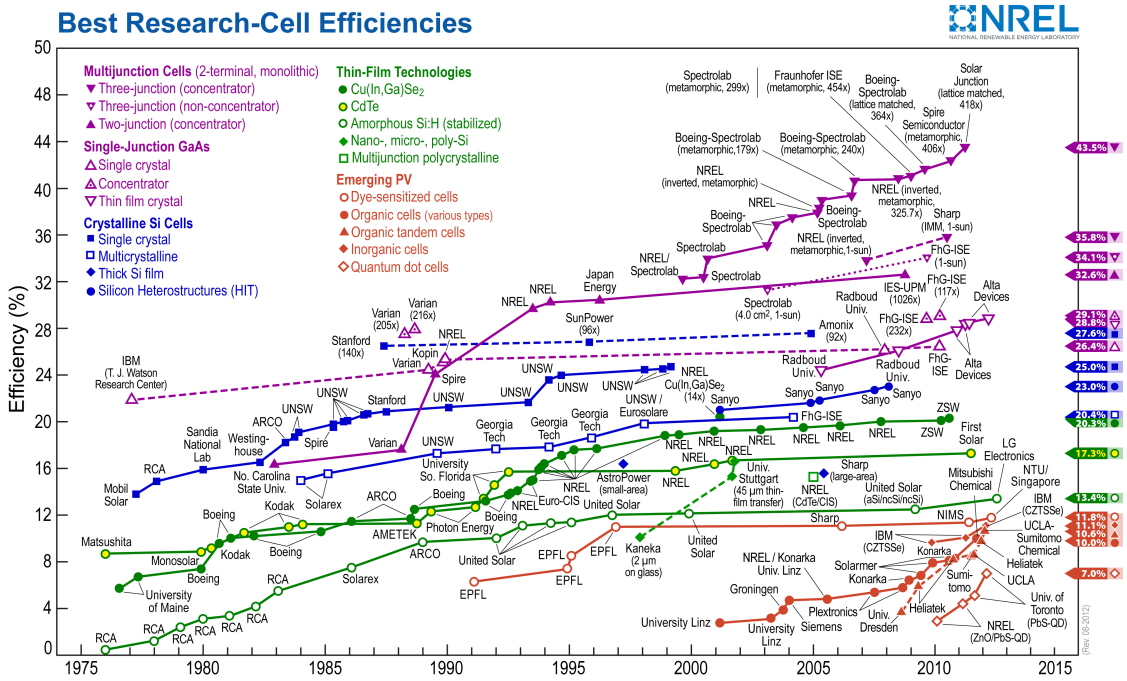

Figure 1.1: Solar cell efficiency - Conversion efficiencies of best research solar cells worldwide from 1976 through 2012 for various photovoltaic technologies. Efficiencies determined by certified agencies/laboratories, taken from [22].

Heterojunction contacts allow combination of surface passivation and electrical contacting. Further on, the advantages of HIT cells are the following:

- Simple structure. High efficiency cells can be obtained without complicated structural techniques, such as optical mask or partial heavy doping.
- Simple, low temperature process. Due to the simple structure, the process is quite simple. The low process temperature also does not degrade the carrier lifetime of the substrate even for low quality Si materials.
- Realization of both good passivation and contacting (combined use of intrinsic and doped amorphous silicon layers ($a-Si$) are needed in order to reach this result).

Some open field for optimization are shown in Fig. 1.2. Improvement of HIT junction quality is the main topic of this work.

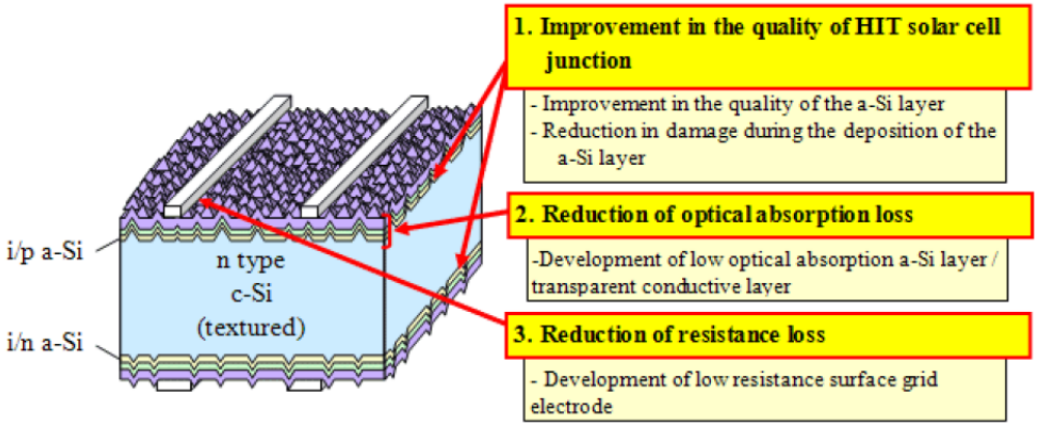

Figure 1.2: HIT cell - Structure of an HIT textured solar cell with possibilities of optimization. Figure taken from [23].

The thesis reviews aspects that goes from a theoretical introduction to amorphous solids, towards a presentation of the measurement techniques employed. It follows with an overview of the sample preparation process, with focus on the deposition of a-Si:H layers. The experimental results are then reported.

2

Theory

This chapter gives a brief introduction about hydrogenated amorphous silicon and heterojuction solar cells.

2.1 Amorphous Solids Concept

The main feature of an amorphous solid is its disordered structure.
The lack of periodicity does not allow using the simpler and well known semiconductor crystalline theory. Short range bonding interactions rather than long range order have to be taken into considerations to explain the behaviour of the material.
The electronic properties of the semiconductor are deeply influenced by its disordered structure. A resume of the correspondence between the atomic structure and the electronic properties can be summarized as shown in fig. 2.1. The presence of the same covalent bonds both in amorphous and crystalline silicon leads to a similar overall electronic structure, i.e. amorphous and crystalline phases of the same material tend to have comparable band gaps.[1] The disorder represented by deviations in the bond lengths and bond angles broadens the electron distribution of states and causes electrons and holes localization as well as strong scattering of the carriers.
Structural defects (such as broken bonds) have corresponding electronic states which normally lie in the band gap. Alternating the bonding configurations for each atom leads to a strong relation between electronic states and structural configurations.

[1] Bandgap of a-Si alloys can be varied in a wide range (1.1 to 3.7 eV) by the incorporation of hydrogen, oxygen, carbon, and germanium etc. [24]

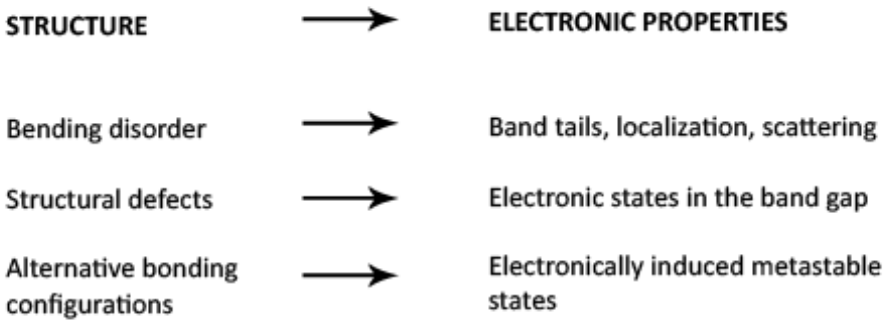

Figure 2.1: Disorder influences electronic transport - The correlation between atomic structure and electronic properties. [2]

2.1.1 Atomic structure

Amorphous semiconductors are not completely disordered. In silicon, covalent bonds are mostly the same for crystalline and amorphous solids, with the same number of neighbours atoms and the same average bonding lengths and angles. Although the disorder can be shown with the atom pair distribution function, which is the probability of finding an atom at a distance R from another atom. A schematic presentation of the pair distribution functions for crystalline, amorphous (or liquid) and gaseous phases is shown in Fig. 2.2.[1]. The relative positions of atoms in a dilute gas are random (except at very close distance), whereas a perfect crystal is completed ordered to large pair distances. The amorphous material has about the same short range order as the crystal but lacks completely of long range order. Amorphous and crystalline phase of the same material in fact share the same material properties because of the same short range.
The behaviour of an amorphous solids is described by the continuous random network model. The periodic crystalline structure is replaced by a random network in which each atom has a specific number of bonds to its immediate neighbours. In fig. 2.3 a 2-D representation of such a network is shown. The random network has the property of easily adapt its structure to atoms having different coordination number, even if in small concentration. This is in marked contrast with the crystalline lattice in which impurities are constrained to have the same coordination of the host.

[1]The interested reader can read more about the distribution function on the reference *Physics of Amorphous Solids* [1]

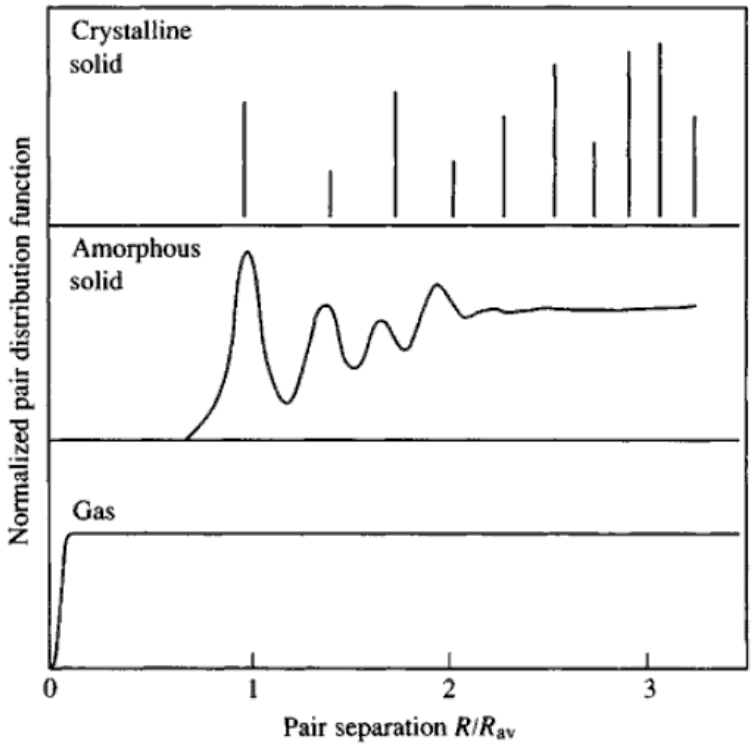

Figure 2.2: Radial distribution function - Schematic of the atom pair distribution functions for a crystalline and amorphous solid, and a gas. The values are scaled by the average distance R_{av} with the nearest atoms. The figure shows the different degree of structural (dis)order.[2]

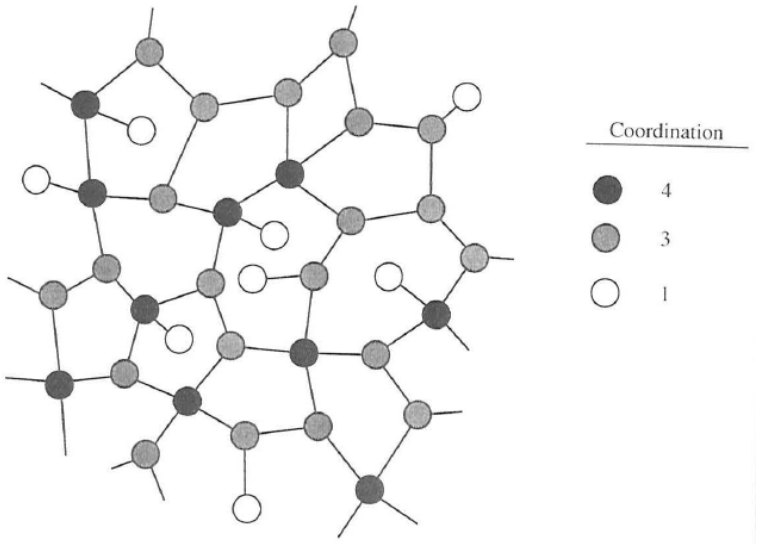

Figure 2.3: Continuous Random Network - An example of a continuous random network containing atoms with different bonding coordinations. [2]

The definition of defect in an amorphous solid is different from the one of a crystalline network. In a crystal every atom which is not in the right position is a defect. On the contrary, since there is not a *right position* for an amorphous solid, other characteristics have to be considered in order to evaluate the presence of defects, e.g. the lack of a bonding. It is possible to describe the amorphous network *order* with the coordination number, which is defined as the number of neighbours of an atom. The elementary defect of an amorphous semiconductor is a coordination defect, i.e. when an atom has too many or too few bonds. The ability of the disordered network to adapt to any atomic coordination allows an isolated coordination defect, which is not possible in a crystal (leading to free carriers, i.e. doping). The different defects are illustrated in fig. 2.4.

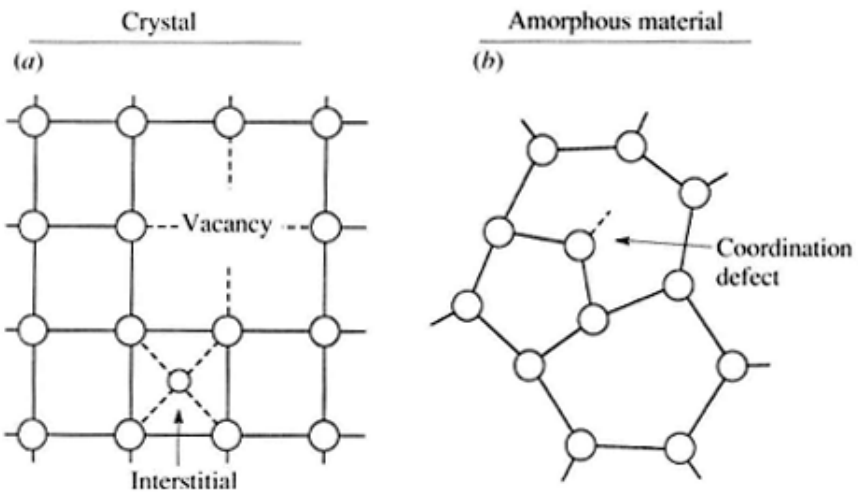

Figure 2.4: Defects in crystalline and amorphous network - This schematic representation shows different types of simple defects in (a) crystalline and (b) amorphous networks. [2]

A brief resume follows. The intrinsic disorder of a continuous network is less easily classified in terms of defects. The network has many different configurations, but if it provides the same atomic coordination, all these structures are equivalent and represent the natural variability of the material. Since there is no correct position of an atom, one cannot say whether a specific structure is a defect or not. Long range disorder is also intrinsic of an amorphous material and it's described by randomly varying the disorder potential.

2.1.2 Chemical bonding, the 8 - N rule and defect reactions

The continuous random network model deals with local chemical bonding. a-Si:H and most of the other amorphous semiconductors are covalently bonded, with well-defined bonding geometries and coordination. A molecular orbital model for silicon is illustrated in Fig. 2.5. Valence electrons of an isolated silicon atom occupy $3s_2$ and $3p_2$ states, in addition to the deeper core states which are not involved in the bonding. When the atoms combine to form a solid, interactions between electrons split the valence states into bonding and anti-bonding levels, as illustrated in fig. 2.5. Chemical bondings

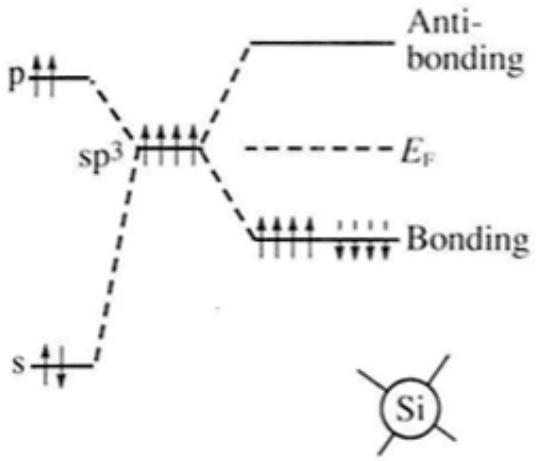

Figure 2.5: Silicon chemical configuration - Illustration of the bonding configuration of Silicon atom which is formed from hybridized molecular orbitals. The position of the Fermi energy E_F is indicated. [2]

occur because the bonding state has lower energy than the isolated atomic levels. The material has the lowest total energy when the maximum number of electrons fill bonding states. The amount is constrained by the Pauli exclusion principle which prevents more than two electrons occupying one state. To optimize the number of bonding states, the atomic wavefunctions combine to form hybrid molecular orbitals, described by,

$$\Phi_{hyb} = a\Phi(3s) + b\Phi(3p) \tag{2.1}$$

where a and b are constants. The four silicon valence electrons combine to give four sp^3 orbitals. Each orbital has a tetrahedral form and it comprises 1/4 of an s-type state and 3/4 of a p-type state. These four orbitals tend to form four bondings with the adjacent atoms. The hybridization minimizes the total energy of the system by arranging as many

electrons as possible in the bonding orbitals.
In general, the behaviour of a group of atoms which bond to each other depends on the number of valence electrons. Hybridization is not always the better energetic solution: e.g. Selenium which has 6 valence electrons does not create any hybrid orbitals because in that case it would have to fill some anti-bonding orbitals, which would increase the total energy of the system.
It follows that the optimal number, Z, of covalent bonds for an element is,

$$Z = 8 - N \quad (\text{for } N \geq 4 \text{ and } Z = N \text{ for } N < 4) \tag{2.2}$$

where N is the number of valence electrons. This prediction of the atom coordination is known as the *8-N* rule.

In a crystalline network the lattice itself imposes the chemical bonding behaviour of the impurity which must adapt to the host structure, i.e. to its coordination number. This is the main reason why phosphorous in amorphous silicon theoretically should not be able to dope the host, because the network can adapt to its ideal coordination number (3) without letting any free electrons.
Experiments performed using hydrogenated amorphous silicon show the opposite anyway. Hydrogen, thanks to its healing effect, could be responsible for the much higher effective doping reached. The ability of effectively dope amorphous silicon was the key point for allowing the usage of amorphous silicon in electronic device fabrication. See section 2.3 for further details on doping of amorphous silicon.

2.1.3 Electronic Structure

The three main features of the structure of an amorphous semiconductors are: 1) short range order of the ideal network; 2) long range disorder; 3) coordination defects. We have already said how the preservation of the short range order results in a similar overall electronic structure of an amorphous material compared to the equivalent crystal. The abrupt band edges of a crystal are replaced by a broadened tail of states extending into the forbidden gap, which originates from the deviations of the bonding length and angle (long range structural disorder).
Electronic states deep within the band gap arise from departures of the ideal random network, such as coordination defects. Those defects determine a lot of electronic properties by controlling trapping and recombination. The electronic structure of an amorphous

semiconductor, see fig. 2.6, comprises bands, band tails and defect states within the band gap.

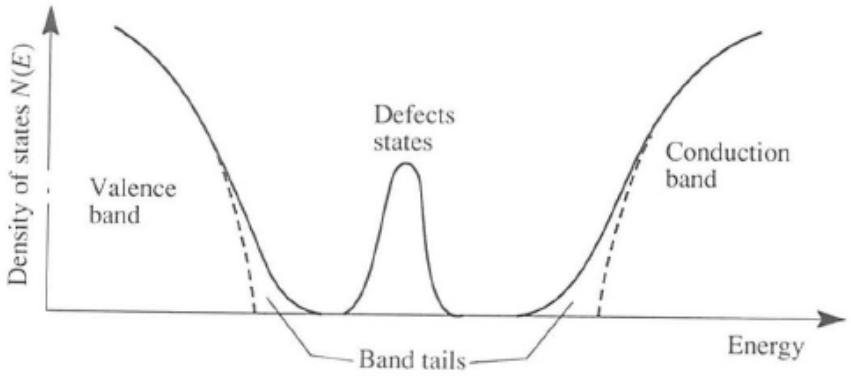

Figure 2.6: Density of states in an amorphous solids - A schematic distribution of the density of states for an amorphous semiconductor showing bands, band tails, and defect states in the band gap. The dashed curves are the equivalent density of states in a crystal. [2]

2.2 Growing of Amorphous Silicon

The gas used to grow (hydrogenated) amorphous silicon is normally silane (SiH_4); other gases can be added for doping and alloying.

Silane decomposes in the absence of plasma at about 450 °C and decomposition at such an high temperature is used to make polycrystalline or epitaxial silicon. Amorphous films can be grown in this way if the temperature is less than about 550 °C, but these films are mostly of low quality because the temperature is too high to retain hydrogen [2]. Deposition of hydrogenated films at lower temperatures requires a source of energy to dissociate silane and this is the role of the plasma. There are mainly two different types of reactor to generate the plasma. They are based on: 1) inductive electrode; 2) capacitor plates. Despite the type of reactor, there are a lot of variables in the deposition process which must be controlled. *Gas pressure* determines the mean free path between collisions and influences whether the reactions occur at the growing surface or in the gas. *Gas flowing rate* determines the residence time of the gas species in the reactor. *Rf power* controls the rate of dissociation of the gas and therefore also the film growth rate. *Temperature* of the substrate influences the chemical reactions on the growing surface.

The leading industrial technique for deposition of a-Si:H and μc-Si:H thin films is PECVD in capacitive coupling reactor operating at 13.56 MHz.[1] Fig. 2.7 shows a schematic diagram of such a parallel-plate PECVD reactor. Besides its simplicity, this

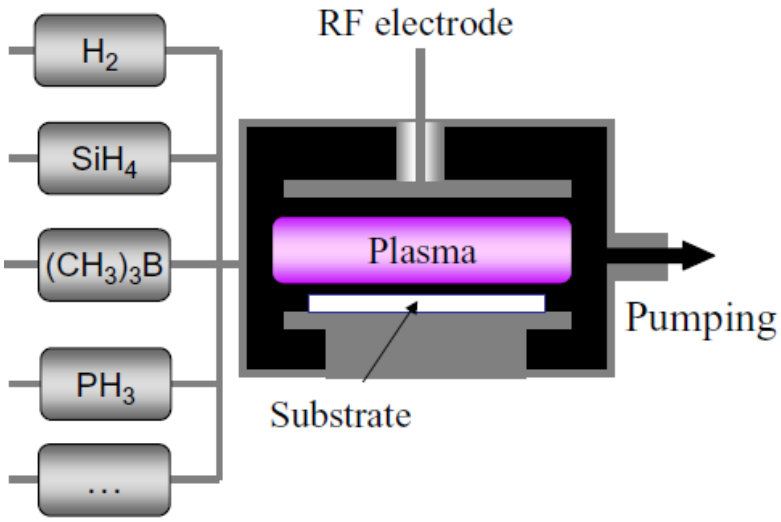

Figure 2.7: Capacitive reactor for PECVD - Schematic diagram of a plasma enhanced chemical vapour deposition reactor. It consists of a gas handling system, a vacuum system, a RF power electrode and a substrate holder, which is usually heated [28].

type of reactor also benefits from advantages associated to plasma processes [4], namely: i) Dissociation of gas precursors is produced by collisions with high energy electrons, and therefore deposition is possible at low temperature. ii) Ions are accelerated towards the substrate and thus can bring energy to the growth zone, which will generally lead to dense and smooth films. iii) Wide range of gas precursors can be formed which allows to produce a wide range of thin films: a-Si:H, a-SiGe:H, a-SiC:H, a-SiO_x, etc [4]. Moreover these films can be made p-type or n-type by adding either diboran or phosphine (or others) to the gas mixture and can be easily stacked on top of each other by changing the flow of gases into the reactor.[2]

2.2.1 Gas Phase Reactions

Once SiH_4 is injected in the reactor and the power is applied to the RF electrode, electrons will be accelerated by the electric field, gaining enough energy to dissociate. The primary reactions between electrons and silane can be: dissociation, ionization and attachment.

[1] The same technique is used for the deposition of amorphous silicon layers in our fabricated cells.

[2] In the system used in this work the process chamber is changed to make doped layer depositions, see section 4.3.

The relative importance of each reaction depends on the energy of electrons, which is a function of the electric field (from which they gain energy) and of their mean free path, which depends for example on the total pressure. Figure 2.8 shows the products of reaction between silane and electrons of 70 eV, as deduced from mass spectrometry measurements [21]. One can see that radicals are the main product, followed by ions, and that within each group SiH_3 is the most abundant products.

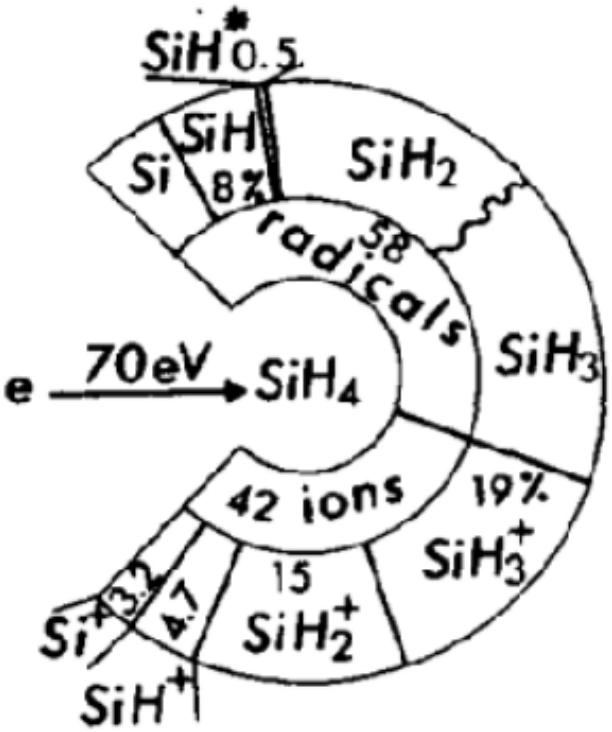

Figure 2.8: Production of Silane Plasma. - Dissociation pattern of a silane molecule upon impact of a 70 eV electron as deduced from mass spectrometry measurements. Taken from reference [5].

At low pressures (1-10 Pa) the mean free path of the products of silane dissociation is comparable or higher than the distance between the electrodes and thus primary reactions are dominant. However, besides primary reactions, one should also consider secondary reactions, that are reactions which result from the interaction of the products of primary reactions with the most abundant species in the discharge, i.e. silane molecules.

When trying to increase silane dissociation, for example by increasing the RF power coupled to the plasma, one also enhances those secondary reactions, which will gain importance and eventually dominate the plasma chemistry [7]. The complexity of plasma

processes is schematically illustrated in fig. 2.9 by the rich variety of species present in the plasma.

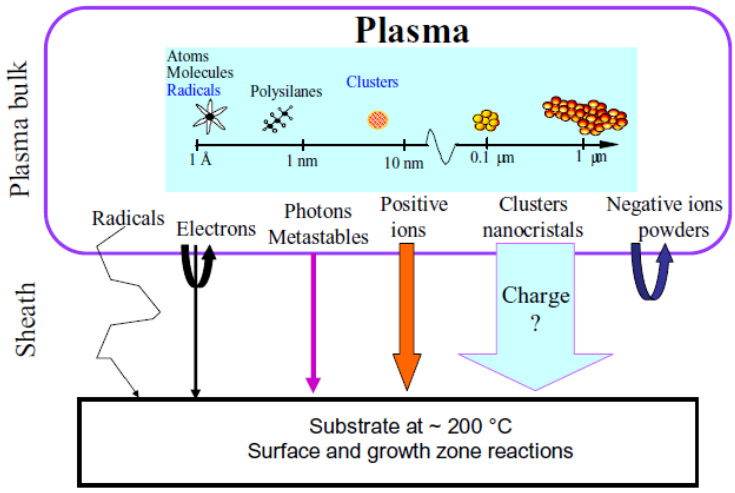

Figure 2.9: The different constituents of Plasma. - The plasma as a source of reactive species. Their interaction with the substrate depends on their charge [28].

However, it is important to keep in mind that growth models often correspond to a simplified case of the general situation presented in Fig. 2.9. In the ideal situation of only SiH_3 reacting with the substrate (considered the dominant product of dissociation reactions), it is possible to summarize the process with the picture shown in figure 2.10.

2.2.2 The Role of Hydrogen

The introduction of hydrogen into amorphous silicon decreases of several order of magnitude the number of defects, making possible the use of amorphous silicon as a semiconductor for electronic devices.

The formation of bonds between silicon and hydrogen decrease the number of dangling bonds, which are caused by the asymmetrical structure and coordination defects. Its concentration is normally found to be below the theoretic expectation (see ref. [12]) caused for example by the formation of micro-structure. Also, a lot of different Si-H bonds can be seen in terms of formation of new states that can be created and/or filled by the introduction of hydrogen. Some state can be close to trasport band leading hydrogen itself to be related with transport of charge.

Using IR spectroscopy and Nuclear Magnetic Resonance (NMR) it has been possible to learn more about hydrogen behaviour, namely its concentration into silicon and its

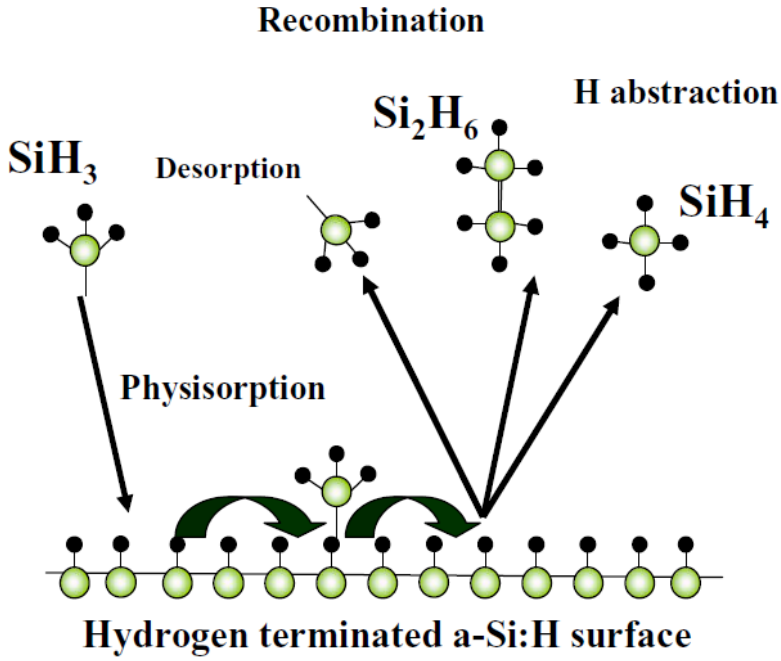

Figure 2.10: SiH_3 deposition. - Standard view for the deposition of a-Si:H based on the interaction of SiH_3 radicals with a hydrogen terminated silicon surface [28].

cluster aspect. An interesting result is shown in figure 2.11, where it can be seen how the distributed form of hydrogen into a-Si is quite independent from its concentration; instead the clustered hydrogen structures increase with hydrogen concentration. It is known that clustered hydrogen doesn't help network relaxation. After a certain concentration then, hydrogen does not give any more advantage, and it can rather take to an increment of defects.

2.3 Doping of Amorphous Silicon

Doping of an amorphous material is a very complicated subject and a deep discussion into this topic is out of the scope of this thesis. Though a short introduction is given.
Basic concepts of doping of amorphous silicon are highly related with the *coordination number*, which has been introduced earlier in this chapter.
In a crystalline silicon network the coordination number is 4 for all the atoms, and if an impurity is present, the network itself will force the impurity to obtain the same coordination number of the host. This is in fact what is happening in a crystalline doping process in which the doping atom will acquire the same configuration of the host giving an (almost) free electron or hole, depending on the doping type.

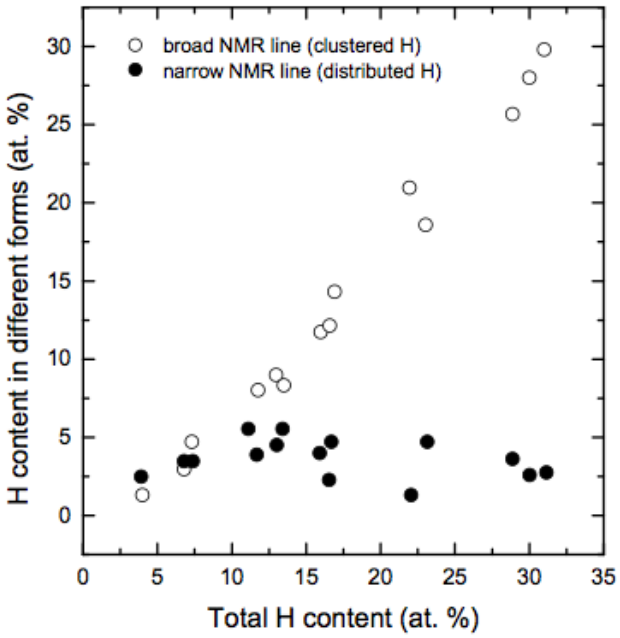

Figure 2.11: Hydrogen different structure. - Contributions of distributed and clustered hydrogen to the total a-Si:H hydrogen content as implied by nuclear magnetic resonance measurements. Taken from reference [13].

What is different in an amorphous solid is that the material lack of long distance order and that the network itself can easily *adapt* to a different configuration, this happens without requiring a lot of energy because the network does not have to change a lot of its configuration, rather only the closest atoms will have to adjust.

The network tends to act following the most energetically convenient way. Some basic concepts which take part in this process are treated here.
Let's consider as an explicative example the doping with phosphorous, which has normally 3 as coordination number (it doesn't hybridize). Its inclusion in a *crystalline silicon* network, supposing that the host won't force a changing of its coordination number, will need the following amount of energy:

$$E_c(P_3) = -3 \cdot E_B \cdot \gamma + E_D \tag{2.3}$$

where E_B is the favourable bonding energy and γ takes into account the lack of symmetric bonds into the host network (from which some bonding energy is lost) while E_D deals with the dangling bonds that inevitably come after adapting the network to a different coordination number. In the case instead of a change of the coordination number of

phosphorous , as to adapt to the silicon network, a different energy will be needed:

$$E_c(P_4) = E_{PRO} + E_{AB} - 4 \cdot E_B \tag{2.4}$$

where E_{PRO} is the cost to make hybrid orbitals for phosphorous (in this way it would be able to have 4 bondings), that means the energy to move an electron from a s to a p orbital; E_{AB} is the cost of having an electron in an anti-bonding orbital; while E_B is the energy earned by the bondings. If

$$E_c(P_3) > E_c(P_4) \tag{2.5}$$

then phosphorus will be included with 4 as coordination number giving an (almost) free carrier and working as an actively doping state. This is what happens in crystalline silicon.
In the amorphous structure the network doesn't require a lot of energy to adapt to a different coordination number thanks to its intrinsic disorder. This is why it's possible to consider:

$$E_a(P_3) \approx -3 \cdot E_B \tag{2.6}$$

and

$$E_a(P_4) \geq E_{PRO} - 4E_B + E_{AB} = E_c(P_4) \tag{2.7}$$

where the inequality has been used considering that disorder may influence bonding energy (which would be less than the ideal). Setting $E_a(P_3) < E_a(P_4)$ one obtain:

$$E_{PRO} - E_B + E_{AB} \geq 0 \tag{2.8}$$

Considering that $E_{PRO} > E_B$ [11], eq. 2.8 results always true. From this result comes that theoretically doping into amorphous silicon is not possible. But experimental results show the opposite.

Even if further models have been tried to be developed, this phenomenon has not yet been fully understood until today.
This model doesn't take into account that atoms in the interface can be easily ionized from plasma interaction which can make other reactions possible, eventually more energetic favourable. In this case a possible changing in the reaction could happen, leading to:

$$SI_4^0 + P_3^0 \leftrightarrow Si_3^- + P_4^- \tag{2.9}$$

with the right term representing an active doping configuration.

It should be clear by now how an increment of the dopant concentration (solid phase concentration) doesn't mean an effective higher doping. It is useful in fact to define the doping efficiency η_{tot}:

$$\eta_{tot} = \eta_{sol} \cdot \eta_{inc} = \frac{N_{act}}{N_{gas}} = \frac{N_{act}}{N_{sol}} \cdot \frac{N_{sol}}{N_{gas}} \tag{2.10}$$

where N_{act}, N_{sol} and N_{gas} are concentration respectively of active doping, solid phase doping and gas phase doping. Experimentally it has been found that η_{sol} (solid phase doping efficiency) decreases with N_{sol}. Instead η_{inc} (efficiency defined as the ratio between solid phase concentration and gas phase concentration of the dopant) stays quite constant.As a consequence the total efficiency appears to decrease with N_{gas} (gas phase dopant concentration) with a slope of ca. 1/2, see fig. 2.12 from [11].

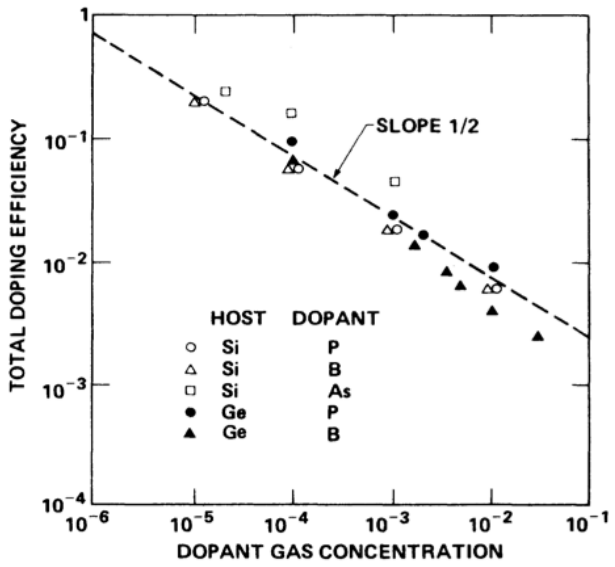

Figure 2.12: Total doping efficiency. - Total doping efficiency as a function of dopant gas concentration in PECVD.

2.4 Fundamentals of HJT cells

In this section a brief overview of the working mechanisms of an heterojunction c-Si/a-Si solar cell will be exploited.

The radiations passing through a solar cell produce couples of electron-hole photo-generated. During this phase chemical energy is acquired. When positive charges (holes) and negative charges (electrons) are effectively separated and collected at the electrodes, electrical energy is produced.

A solar cell contains an absorber layer in which photons of the incident radiation are absorbed, thereby generating electron-hole pairs. In order to separate electrons and holes from each other, a so-called "semi-permeable membranes" can be attached to both sides of the absorber in order to selectively allow only one type of charge carrier to pass through. An important issue for designing an efficient solar cell is that the electrons and holes generated in the absorber layer must reach the membranes. This requires that the thickness of the absorber layer is smaller than the diffusion lengths of the charge carriers. A membrane that lets electrons pass and blocks holes is a material that has a large conductivity for electrons and a small conductivity for holes. An example of such material is an n-type semiconductor, in which a large electron conductivity with respect to the hole conductivity is caused by a large difference in electron and hole concentrations. Electrons can easily move through the n-type semiconductor while the transport of holes, which are the minority carriers in such material, is very limited due to the recombination process. The opposite holds for electrons in a p-type semiconductor, which is an example of a hole membrane.
In order to minimize the injection of holes from the absorber into the n-type semiconductor an energy barrier should be introduced in the valence band, ΔE_V, at the interface between the n-type semiconductor and the absorber. Ideally, this can be achieved by choosing an n-type semiconductor that has a larger band gap than that of the absorber, where the energy difference between the band gaps is fully accommodated in the valence band of the two materials. Similarly, the injection of electrons from the absorber into the p-type semiconductor can be suppressed by use of a p-type semiconductor with a larger band gap than that of the absorber, with the band offset contained fully within the conduction band, ΔE_C. The requirement of having the band offset in the conduction band means that the electron affinity, X_e, of the p-type semiconductor is smaller that the electron affinity of the absorber. The additional advantage of applying membrane materials with large band gaps is to allow a larger fraction of photons in the solar spectrum to be transmitted through the membranes to the absorber. Figure 2.13 shows a schematic band diagram of an illuminated ideal solar cell structure with an absorber and semi-permeable membranes. When the absorber and membrane materials have different semiconductor properties, such as different energy band gaps, we describe the junction

as a heterojunction.

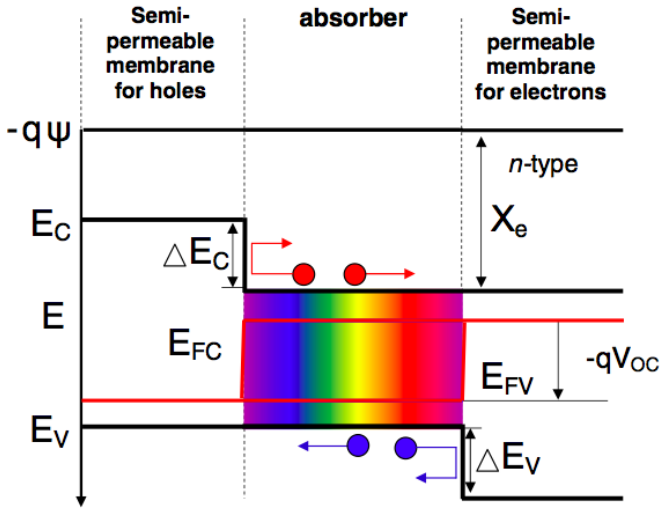

Figure 2.13: Ideal heterojunction. - Schematic band diagram of an idealized heterojunction solar cell structure at the open- circuit condition [28].

The quasi-Fermi level for electrons, E_{FC}, and the quasi-Fermi level for holes, E_{FV}, are used to describe the illuminated state of the solar cell. The energy difference between the quasi-Fermi levels is a measure of the efficient conversion of radiation energy into chemical energy. In Fig. 2.13 the illuminated solar cell is shown at the open-circuit condition, which is when the terminals of the solar cell are not connected to each other and therefore no electric current can flow through an external circuit. Under this condition, a voltage difference can be measured between the terminals of the solar cell. This voltage is denoted the open-circuit voltage, V_{OC}, and it is an important parameter to consider when characterizing the performance of solar cells.
In a heterojunction solar cell the injection of one type of charge carriers from the absorber into membrane materials, in which they become minority carriers and recombine, can be suppressed. This can result in a more efficient use of photo-generated carriers and consequently a higher photocurrent from the cell.

In practical heterojunction solar cells, the band offsets between different materials are accommodated in both the conduction band and the valence band. This can result in the formation of transport barriers between the absorber and the membrane for the majority carriers. This is illustrated in Fig. 2.14, which shows a heterojunction formed between n-type c-Si with a band gap of 1.1 eV and p-type a-Si:H with a band gap of 1.7

eV. A transport barrier is formed for the holes at the interface between the two materials. The holes can drift through narrow "spike" barriers by tunneling, trap-assisted tunneling and/or thermionic emission.

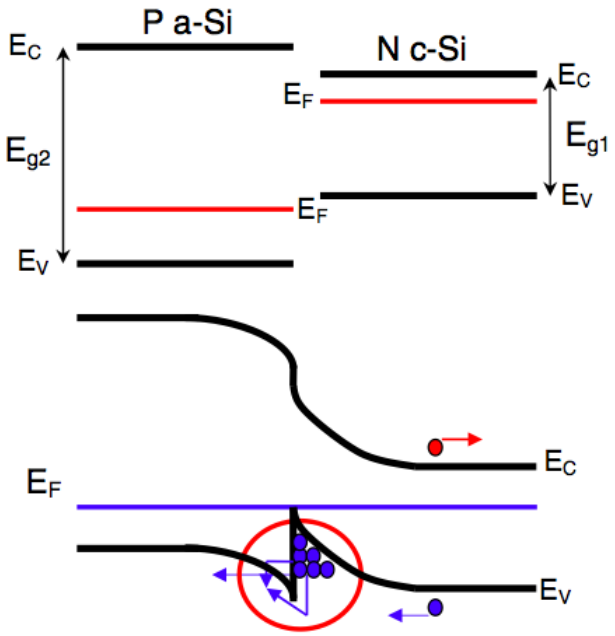

Figure 2.14: Band diagram. - Schematic band diagram of an a-Si:H/c-Si heterojunction. The red circle highlights the carrier transport through the energy barrier [28].

Due to the band gap of a-Si:H and c-Si differing by about 0.5-0.7 eV, offsets between the conduction and valence bands of a-Si:H and c-Si are present. The state of knowledge is that the valence band offset is larger than the conduction band offset by a factor of 2-3 [29]. This asymmetry in the band lineup can be understood from a fundamental point of view employing the "charge neutrality levels" for both a-Si:H and c-Si, which are aligned in forming the heterojunction [30]. The band bending in the structure adjusts such that charge neutrality is fulfilled, just as for c-Si homojunctions. Due to the large density of rechargeable states in a-Si:H, the band bending supported on the a-Si:H side is small, in fact the electric field coming from the c-Si dopant ions is shielded already close to the heterointerface. Thus, the bands in the a-Si:H are comparably flat, while the c-Si supports most of the overall band bending [31].

In a homojuction, the built-in potential amounts to $\Psi_{bi} = kT/q \log(N_A N_D/n_i^2)$, with N_A and N_D being the doping concentrations on both sides of the junction. In

order to ensure efficient separation of excess carriers by imposing a large Ψ_{bi} , the doping concentrations would have to be maximized. This, on the other hand, increases the recombination in the c-Si bulk. The resulting bulk recombination in the highly doped emitter regions limits the V_{OC} for c-Si homojunctions [32].

In a heterojunction, the Fermi level in the wide-band gap material does not need to be brought as close to the bands to yield the same overall band bending, due to the band offsets. The inherent asymmetry of the distribution of band bending in the heterojunction leads to the possibility of imposing a larger c-Si band bending for a given c-Si dopant concentration as compared to the c-Si homojunction. In SHJ solar cells, c-Si doping concentrations around 10^{15}-10^{16} cm^3 can be employed, leading to a much higher c-Si minority carrier lifetime, which contributes to a higher V_{OC} potential. The second crucial ingredient for the high V_{OC} potential is the outstandingly high potential for c-Si surface passivation by amorphous silicon, provided particularly by undoped a-Si:H. Surface recombination velocities well below 5 cm/s have been reported for (i)a-Si:H layers [33], and if made thin enough the undoped a-Si:H buffer layer seems not to significantly affect the charge carrier transport across the heterojunction [35]. Thus, combined with the advantageously low c-Si bulk recombination rates due to small doping concentrations, the surface passivation by a-Si:H yields very high V_{OC} potential of SHJ solar cells. The influence of the (i)-aSi:H thickness into passivation quality and transport properties is the main investigation of this thesis.

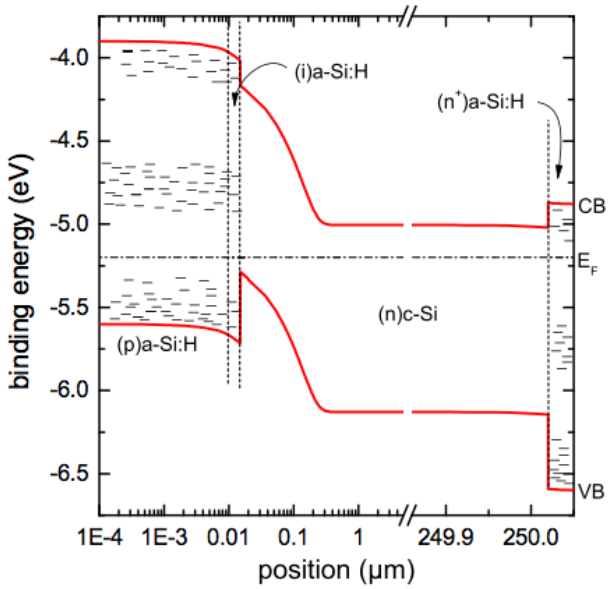

Figure 2.15: Band diagram with defects. - Band structure of an a-Si:H/c-Si heterojunction solar cell based on an (n)c-Si substrate as calculated with the numerical device simulator AFORS-HET. Small horizontal lines schematically indicate high densities of localized states. [12].

3

Measurement techniques

In this chapter a brief overview of the techniques employed to analyze the samples in this thesis is given.

The quasi-steady state photoconductance decay (QSSPC) method [15] is a well known method to evaluate effective lifetimes of wafers and solar cell during their fabrication process. The QSSPC method also allows to calculate an implied voltage [26] of the solar cells during their fabrication process, since this method does not require any contacting of the sample. Furthermore the solar cell characterization tool LOANA (Loss Analysis) from the company pv-tools is presented. This tool measures the I-V characteristics of the solar cell, i.e. light I-V curve, dark I-V and $J_{SC} - V_{OC}$. Furthermore the calculation of the series resistance of a solar cell by means of the I-V characteristics is presented. Electroluminescence is also presented, which has been used in order to characterise the electrical transport properties of the cell, together with the quality of the contacts. Moreover ellipsometry measurements are used to check the growing ratio of the deposition process. At last, the XPS technique is shown, which has been used in order to check the presence of unwanted elements in the cell.

3.1 Lifetime measurement

In this work the Sinton Instrument WCT-120, which is shown in fig. 3.1 is used to evaluate the lifetime of the fabricated samples. The measurement technique is called quasi steady state photoconductance decay (QSSPC) .

Figure 3.1: Sinton Instrument WCT-120 - Picture of the tool used for lifetime and implied V_{OC} measurement.

In the following sections a theoretical introduction is first given, then an overview about the different methods of measurement are presented.

3.1.1 Introduction

Photoconductance σ^* measurement allows determining the recombination lifetime of electron-hole-pairs in a semiconductor.
Photoconductance is measured through a coil inductive coupling with the sample. The instrument measures a voltage which is made proportional to the conductivity.
The increase of conductance thanks to the exited carrier (photoconductance) is measured together with the light intensity. The light intensity is measured through monitoring the current variation of a reference cell.
In general, the sheet conductance σ of a silicon wafer is a product of carrier's density, mobility and thickness of the cell:

$$\sigma = q \int_0^W (n\,\mu_n + p\,\mu_p)\,dz \tag{3.1}$$

where q is the elementary charge, W is the sample thickness, n and p are the electron and hole concentrations, while μ_n and μ_p their mobility. Note that the carrier concentrations are function of the position.
During a QSSPC measurement, the quantity of interest is the excess carrier density Δn,

and hence the photoconductance. It is convenient then to split σ into:

$$\sigma = \sigma_{dark} + \Delta\sigma \tag{3.2}$$

where σ_{dark} is measured at a fixed time before a trigger, which is activated by a certain value of light intensity.
Since the photogeneration of excess carriers is quite homogeneous, eq. 3.1 can be simplified by introducing an average excess carrier density Δn_{av}. The photoconductance $\Delta\sigma$ is then given by:

$$\Delta\sigma = q\,W\,(\mu_n + \mu_p)\,\Delta n_{av} \tag{3.3}$$

So the mobilities have to be known in order to obtain the excess carriers from the measured photoconductance. The mobilities themselves are dependent on Δn. Therefore an iterative routine is necessary to evaluate Δn with an excess carrier dependent mobility model [27].

The calibrated reference cell is used to obtain the light intensity at time t. Depending on the optical parameters of the sample (textured samples reflect less than polished ones) the generation rate G [$\mathrm{cm^{-3}s^{-1}}$] of excess carriers can be evaluated from measuring the current flowing on the reference cell.

Knowing both the excess carrier density Δn and the generation rate G allows to determine the carrier lifetime τ. The time dependence of the excess carrier density Δn is given by the continuity equation:

$$\frac{\partial \Delta n}{\partial t} = G(t) - U(t) + \frac{1}{q}\nabla J \tag{3.4}$$

where U is the recombination rate and J is the current density. Since it is possible to consider the photogeneration very homogeneous and the surfaces well passivated, the carrier density in the sample can be assumed to be spatially uniform. As a result, the last term in eq. 3.4 can be neglected. The recombination rate can be written as $U = \Delta n/\tau_{eff}$ which give the effective lifetime τ_{eff}:

$$\tau_{eff} = \frac{\Delta n}{G - \frac{\partial \Delta n}{\partial t}} \tag{3.5}$$

The lifetime measured is called an *effective lifetime*, in fact it includes various recombination factors:

1. Auger;
2. Radiative;
3. SRH;
4. Surface;
5. Emitters.

In formulas:

$$\frac{1}{\tau_{bulk}} = \frac{1}{\tau_{Auger}} + \frac{1}{\tau_{Rad}} + \frac{1}{\tau_{SRH}} \tag{3.6}$$

and

$$\frac{1}{\tau_{eff}} = \frac{1}{\tau_{bulk}} + \frac{S_{front}}{W} + \frac{S_{back}}{W} \tag{3.7}$$

where W is the sample thickness and S the surface recombination velocities.
Depending on the number of excess carriers one can have some recombination phenomenon to be dominant or negligible, making possible to obtain one particular recombination factor if the cell is analysed in a particular regime.

There are two possible measure configurations: 1) Quasi Steady State; 2) Transient.

3.1.1.1 Quasi Steady State

Quasi steady condition for the excess carriers indicates that the generation and recombination rates are in balance. This means that the decay constant of the flash light should be at least 10 times slower than the carrier lifetime. Since the flash utilized has a decay constant of approximately 2 ms, the QSSPC analysis is valid for lifetimes of approximately 200 μs or less. In the steady state condition $G = R$.

PROS:

The measure gives different lifetimes for a broad range of excess carriers, which basically are limited only by the light highest intensity.

CONS:

In order to correctly estimate the generation rate, the optical constant for reflection has to be known. In the samples used in this work a polished sample had an optical constant of 0.7, while a textured sample of 1. The optical constant is the proportionality factor between the photogeneration in the sample and the photogeneration in the reference cell that is measured by its short-circuit current.

3.1.1.2 Transient Mode Analyses

When the lifetime of the sample is too high to use the QSSPC, another type of measurement mode becomes useful, namely the transient mode. In this mode the measurement starts only when the light has almost completely switched off, so $G = 0$.

PROS:

The transient measurement mode does not require the knowledge of the generation rate, i.e. optical properties of the sample do not have to be known.

CONS:

The carrier lifetime has to be very long compared to the time needed to switch off the light source.

3.1.2 Further consideration

An important parameter is the *implied* V_{oc} which is estimated from the value of excess carriers, using the following expression:

$$V_{OC} = \frac{kT}{q} \ln\left(\frac{n \cdot p}{n_i^2}\right) \tag{3.8}$$

where n and p are the total concentration of electrons and holes. Making explicit these concentrations leads to:

$$V_{OC} = \frac{kT}{q} \ln\left(\frac{(n_0 + \Delta n) \cdot (p_0 + \Delta p)}{n_i^2}\right) \tag{3.9}$$

where n_0 and p_0 are the intrinsic carrier concentrations, while Δn and Δp are the excess carriers coming from the light absorption. From eq. 3.9, in the case of a p-type material, we obtain:

$$V_{OC} = \frac{kT}{q} \ln\left(\frac{\Delta n^2 + \Delta n(n_0 + N_A) + n_i^2}{n_i^2}\right) \tag{3.10}$$

where we have considered $\Delta n = \Delta p$ and $p_0 = N_A$. From eq. 3.10 we see how an higher amount of excess carriers leads to an higher V_{OC}. Since the measure does not come from a direct voltage measure (i.e. contacts do not play any role here) we refer to this voltage as to an *implied* V_{OC}.

Interpretation of lifetime data as implied current-voltage relation allows determining the IV-characteristics prior to actually contacting the device.

This is of main importance when checking the influence of the different a-Si layers. Considering the HIT cell, the implied V_{OC} can be measured:

1. after (i)a-Si:H;
2. after (n)a-Si:H;
3. after (p)a-Si:H.

It has been found that proceeding with the amorphous silicon depositions all in a row (i.e. without interrupting the process for measurements) leads to better quality cells. Interrupting the fabrication process for measurements may cause indeed influence from external factors such as oxygen and/or dust. So it is not beneficial for the final device to make a *passivation control* after each fabrication step, even though it may offer better opportunities for understanding the physical behaviour as well as a possible bottleneck.

3.2 Characterisation of solar cells

The tool used to characterise the behaviour of the fabricated solar cells is called LOANA, which stays for Loss Analysis. It is a product of the company *pv tools*, a spin-off of ISFH. LOANA is an automatized system which allows making several measurements on a solar cell, in order to check its behaviour and performance. A photo of the tool is shown in fig. 3.2.
In this work the following measurements have been used:

Figure 3.2: LOANA from *pv tools* - Picture of the tool used for IV measurements.

- light I-V, for 2 different light intensities;[1]
- dark I-V;
- $J_{SC} - V_{OC}$.

A shadow mask of an area $A = 4.25$ cm^2 is used during the measurement, which allows to easily convert I to J ($J = I/A$). Further on, the current density J will be considered, even if the current I is the value actually measured.
A short introduction is given in the following sections for each measurement. In the last section, the use of these curves to calculate the series resistance is presented.

3.2.1 Light I-V

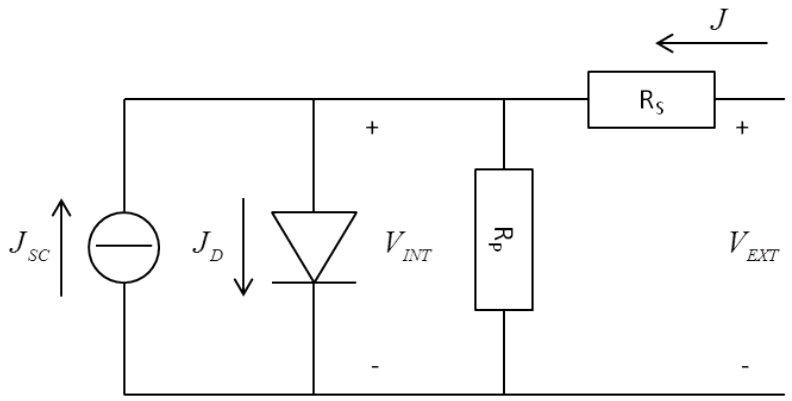

Figure 3.3: Solar cell model - A circuit which describe the cell behaviour in light condition.

In this measure the cell is illuminated through a LED-array which allows good tuning possibility and quite stable intensity.
The model of the cell is reported in Fig. 3.3, described by eq. 3.11:

$$J = -J_{SC} + J_0 \cdot \left[\exp\left(\frac{q \cdot (V_{EXT} - R_S \cdot J)}{kT} \right) - 1 \right] + \frac{V_{EXT} - R_S \cdot J}{R_P} \tag{3.11}$$

where J_{SC} is the current photo-generated, R_S is the series resistance and R_P is the shunt resistance.
The tool measures the current I and the external voltage V_{EXT}, see Fig. 3.3.

[1] Those two curves are used to obtain the series resistance from the "double light" method [19].

3.2.2 Dark I-V

The dark IV measurement evaluates the cell in dark condition. A voltage is applied between the contacts and the current is measured. The eq. describing the cell is similar to eq. 3.11, but it does not contain the term J_{SC} since we have no photogenerated current. A model of the cell in this condition is reported in Fig. 3.4.

$$J = J_0 \cdot \left[\exp\left(\frac{q \cdot (V_{EXT} - R_S \cdot J)}{kT} \right) - 1 \right] + \frac{V_{EXT} - R_S \cdot J}{R_P} \tag{3.12}$$

The tool measures the current I and the external voltage V_{EXT}, see Fig. 3.4.

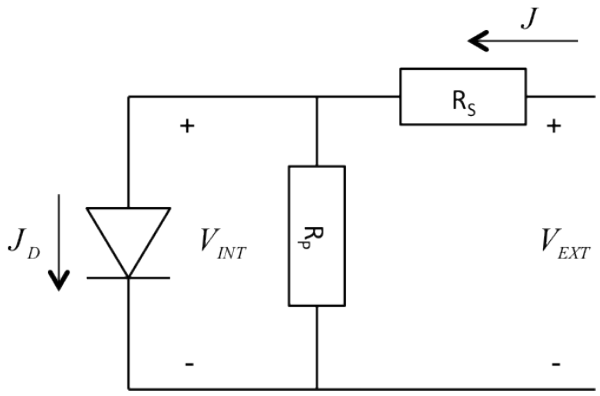

Figure 3.4: *Dark IV* **schematic** - A model representing the *dark IV* curve.

3.2.3 $J_{SC} - V_{OC}$

A Xe-flash lamp is used for this measurement. A $J_{SC} - V_{OC}$ curve is a valuable way of looking at an IV curve in the absence of series resistance. To trace a $J_{SC} - V_{OC}$ curve the intensity of the light is varied and the couple J_{SC} and V_{OC} are measured for each illumination level. The series resistance has no effect on the V_{OC} since no current is drawn from the cell. The series resistance has no effect on J_{SC} as long as the series resistance is less than 10 Ω/cm^2 since the IV curve is flat around J_{SC}. The curve that is traced is similar to the Dark IV curve but without the effects of series resistance.
The $J_{SC} - V_{OC}$ method measures:

$$J_{sc} = J_0 \cdot \left[\exp\left(\frac{q(V_{OC} - R_S \cdot J)}{kT} \right) - 1 \right] \approx J_0 \cdot \left[\exp\left(\frac{q \cdot V_{OC}}{kT} \right) - 1 \right] \tag{3.13}$$

3.2.4 Resistance analysis methods

In this section different methods to determine the series resistance are reported.
Shunt resistance is neglected in the following explanations, although even its consideration wouldn't change the value estimated for the series resistance. Intuitively in fact, since no use of the diode ideal equation is made, having a parallel resistance could just be included into the diode model.
The methods used are a comparison of IV curves measured in different conditions. We use:

1. Double light measure;
2. J_{SC}-V_{OC} / Light IV;
3. $J_{SC} - V_{OC}$ / Dark IV;
4. Light IV / Dark IV.

3.2.4.1 Double light

This method uses two different light IV curves in order to measure the series resistance. Considering in fact the cell equation :

$$I = I_0 \cdot \Big[\exp\Big(\frac{(V - R_S I)}{V_T} \Big) - 1 \Big] - I_L \tag{3.14}$$

Where I_0 is the saturation current, R_S is the series resistance, $V_T = kT/q$ is the thermal potential and I_L is the photo-generated current. If the product $R_S \cdot I$ is negligible, then a change of light intensity only leads to a change into I_L, which consists into a shift of I (the ordinate axis) but not into the shape of the curve, which would come instead from the exponential term.
If the influence of series resistance is not negligible, a change of the photo-generated current causes a shift of voltage, because the exponential term changes the shape of the curve. The shift of the curves is related to the series resistance. It is possible to consider:

$$J_{SC}(A) \qquad J_{SC}(B) \quad \rightarrow \quad \Delta J_{SC} = J_{SC}(A) - J_{SC}(B) \tag{3.15}$$

which are respectively the short-circuit current measured at light intensity A and light intensity B, see Fig. 3.5. After shifting one curve of the quantity ΔJ_{sc} along the current axis, it is possible to consider the displacement $\Delta V(J)$ along the voltage axis through the following equation:

$$R_S = \frac{\Delta V(J)}{\Delta J_{SC}} \tag{3.16}$$

which allows to determine the series resistance. A graphic explanation of the method is reported in Fig. 3.5.

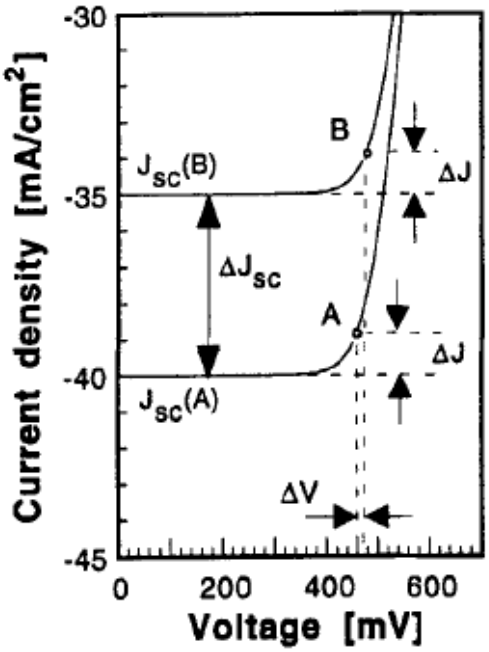

Figure 3.5: The double light method - Basic principle of the double light level method for measuring the series resistance.[25]

3.2.4.2 J_{SC}-V_{OC} / Light IV curves comparison

The comparison of the curves obtained through the light IV measure and the J_{SC}-V_{OC} technique is here shown in order to evaluate the series resistance. The model used are the same presented in section 3.2.1 and 3.2.3 respectively for light IV and J_{SC}-V_{OC}. The key here is to use the measures to obtain the voltage drop in the series resistance, namely $\Delta V = V_{EXT} - V_{INT}$, see Fig. 3.7. Knowing then the current flowing, it is possible to calculate the series resistance through Ohm's law:

$$\Delta V = R_S \cdot J \tag{3.17}$$

where R_S is the series resistance [Ωcm^2].

We consider first the J_{SC}-V_{OC} method and in particular eq. 3.13, it is possible to model the cell behaviour with the circuit shown in Fig. 3.6, where no influence of the

series resistance is remarked. We call the quantities measured through the J_{SC}-V_{OC}:

$$\hat{J}_{SC} \qquad \hat{V}_{OC} \tag{3.18}$$

We remark that those quantities are function only of the light intensity.

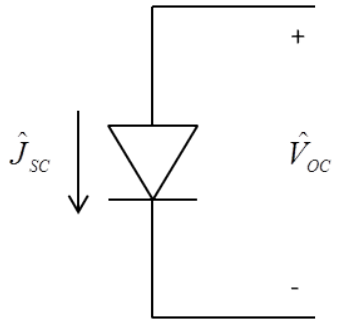

Figure 3.6: J_{SC}-V_{OC} **schematic** - A model representation of the measured J_{SC}-V_{OC} curve.

The light IV measurement can be described modelling the cell with the circuit shown in Fig. 3.7, where the quantity available, measured by the tool, are V_{EXT} and I. A shifted version of the light IV curve must be considereded in order to compare this measure with the J_{SC}-V_{OC} one. Shifting the IV light curve by a quantity J_{SC} allows to mathematically consider the IV curve without the influence of the photogenerated current. In fact, it is possible to write:

$$J' = J + J_{SC} \tag{3.19}$$

where J' is the resulting current shifted, see Fig. 3.8.

Clamping the same current, we will generally obtain two different voltages V_1 and V_2 for each IV curve, see Fig. 3.9. We can then write, considering the notation presented previously in eq. 3.19 and 3.18.

$$J'(V_1) = \hat{J}_{SC}(V_2) \tag{3.20}$$

where the 2 generic voltages measured, V_1 and V_2, are used to evaluate the voltage drop in the series resistance. In this way one is able to evaluate the series resistance. The voltages V_1 and V_2 are respectively measured through the *Light IV* mode and J_{SC}-V_{OC} mode. Considering the models developed in section 3.2.1 and 3.2.3 and keeping the same

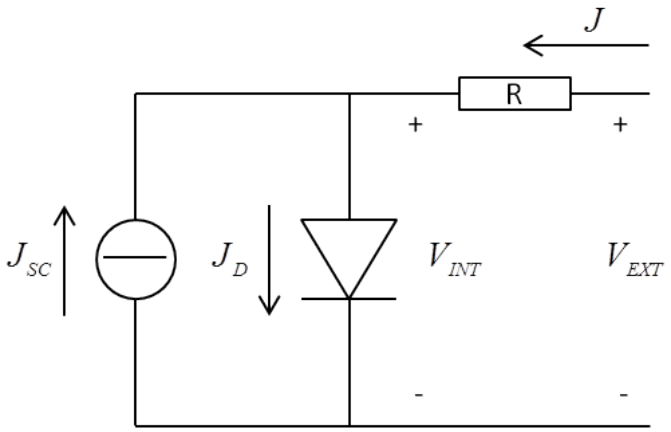

Figure 3.7: *Light IV* **schematic** - A model representation of the measured *light IV* curve.

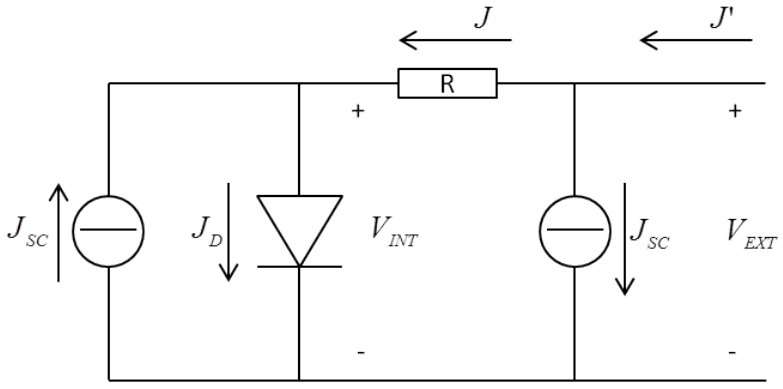

Figure 3.8: *Light IV shifted* **schematic** - A model representation of the shifted *light IV* curve.

notation, the values measured can be called V_{EXT} and $\hat{V}_{OC}$, respectively for the *light IV* curve and $J_{SC} - V_{OC}$ curve, that is:

$$V_1 = V_{EXT} \qquad V_2 = \hat{V}_{OC} \tag{3.21}$$

To evaluate the voltage drop caused by the series resistance, the voltage drop $\Delta V =$

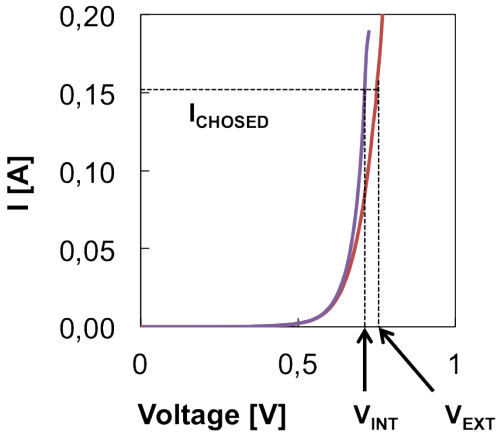

Figure 3.9: Fixing the same current - A schematic presentation of the method which confronts two different IV curves. The red curve correspond to the light IV measure shifted, while the purple curve to the $J_{SC} - V_{OC}$ measure.

$V_{EXT} - V_{INT}$ and the current density flowing J have to be known, see Fig. 3.8.
We said that V_{EXT} is the voltage measured through the light IV measure, while we will now prove that V_{INT} is equal to $\hat{V}_{OC}$ measured through the $J_{SC} - V_{OC}$ method.
Considering the diode of Fig. 3.7, if the current flowing in that diode J_D is equal to the current $\hat{J}_{SC}$ flowing in the diode of Fig. 3.6, then also the voltage drop of the diode is the same for the two circuit, that is $V_{INT} = \hat{V}_{OC}$. Since the voltage measured by the $J_{SC} - V_{OC}$ method is exactly the diode voltage drop (because we have already shown that the series resistance is negligible in this measure) then the $J_{SC} - V_{OC}$ measure gives also V_{INT}. In details:

$$\hat{V}_{OC} = V_{INT} \quad \text{only if} \quad J_D = \hat{J}_{SC} \tag{3.22}$$

and:

$$J_D = J_{SC} + J = \hat{J}_{SC} \tag{3.23}$$

Since $J_{SC} + J = J'$ for definition of J' (see eq. 3.19), and $J' = \hat{J}_{SC}$ because we are considering the same current for the two IV curves (see eq. 3.20), the statement

$J_D = \hat{J}_{SC}$ is proved and $\hat{V}_{OC} = V_{INT}$.
We now have all the data to evaluate R_S:

$$R_S = \frac{V_{EXT} - V_{INT}}{J} = \frac{V_{EXT} - \hat{V}_{OC}}{J} \tag{3.24}$$

It is worth to note that the diode drawn in the models developed could be a generic bipolar device, since no use of diode ideal equation has been done, but only measured quantities have been used. This widens the usefulness of the method described.

3.2.4.3 $J_{SC} - V_{OC}$ / Dark IV curves comparison

The models considered to describe the two different measurement settings are shown in Fig. 3.6 for the $J_{SC} - V_{OC}$ measure and in Fig. 3.10 for the dark IV measure.
Proceeding similarly with the way showed in the previous section, the series resistance

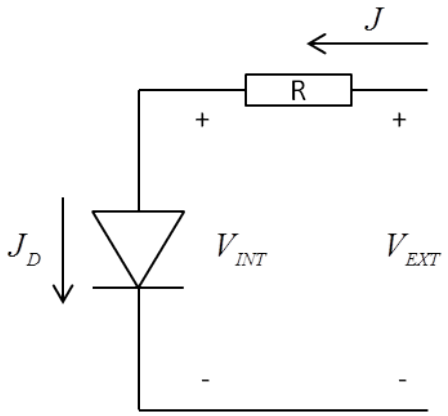

Figure 3.10: *Dark IV* **schematic** - A model representing the *dark IV* curve.

can be evaluated knowing the voltage drop $V_{EXT} - V_{INT}$ and the current flowing, see Fig. 3.10. Fixing the same current for the two measures, namely $\hat{J}_{SC} = J$, the measured voltages are $\hat{V}_{OC} = V_{INT}$ for $J_{SC} - V_{OC}$ measure and V_{EXT} for the dark IV measure. Which allows to calculate the series resistance R_S:

$$R_S = \frac{V_{EXT} - V_{INT}}{J} \tag{3.25}$$

3.2.4.4 Light IV / Dark IV curves comparison

The models which can be used to describe the two different measurement settings are shown in fig. 3.8 for the light IV measure (shifted, since we need to compare it with the dark condition) and 3.10 for the dark measure.
We proceed again similarly with the previous sections, with the only difference that the

current fixed now is the short circuit one, J_{SC}.

For the light IV measure, from setting $J' = J_{SC}$ comes $J = 0$ and as a direct consequence the drop on the resistance $V_R = R_S \cdot J = 0$. Which again means from Kirchoff that $J_D = J_{SC}$ and the measured voltage V_{EXT} (light condition)= V_{INT} (light condition)= V_{INT} (dark condition), because the current flowing in the diode is the same for the two circuits.

In the dark IV curve if we set the measured current to be equal to the short circuit one, $J = J_{SC}$, then the current flowing in the diode will be again J_{SC}, i.e. $J_D = J_{SC}$ and the measured voltage will be V_{EXT}(dark condition).
From these considerations, we again have all the data needed to evaluate the series resistance:

$$R_S = \frac{V_{EXT}(\text{dark condition}) - V_{INT}(\text{dark condition})}{J_{SC}} = \\ = \frac{V_{EXT}(\text{dark condition}) - V_{EXT}(\text{light condition})}{J_{SC}} \tag{3.26}$$

3.2.4.5 R_S as a function of voltage

In the previous sections, series resistance has been evaluated as a function of a fixed current. Since in literature the series resistance in function of the voltage $R_S = f(V)$ is a more common graph, a conversion of the dependence from current to voltage has been performed.
In the experimental chapter the changing of dependence has been done through an IV curve: that means, the voltage in order to obtain the current fixed has been chosen. In section 5.5, the light IV curve has been chosen for this procedure.
In this way the coherence is slightly lost, since the voltage of a light IV measurement does not imply the same current for other types of curves. Anyway the graph has mainly the aim of showing a visual dependence and anyway not very high incongruence should be caused by this calculation. A deeper analysis of the difference caused by the two different dependence (V and I) should be performed in order to better proof the latter statement.

3.3 Photoelectron Spectroscopy: ultraviolet and x-ray

Photoelectron spectroscopy is a technique used to analyse the atomic structure of the surface of a material. A beam of photons shines the layer under test, leading to an emission of electrons with a certain kinetic energy.

Tuning the energy of the beam it is possible to analyse different bonding energy in the atom (from core to more valence states) and different depth of the layer analysed. Two energies have been used:

- X-ray Photoelectron Spectroscopy (XPS), which uses soft x-rays (with a photon energy of 1253.6 eV) to examine core levels.
- Ultraviolet Photoelectron Spectroscopy (UPS), which uses vacuum UV radiation (with a photon energy of ca. 20 eV) to examine valence levels.

Photoelectron spectroscopy is based upon a single photon in/electron out process. The energy of a photon of the beam is given by the following relation:

$$E = h\nu \tag{3.27}$$

where h is the Planck constant $6.62 \cdot 10^{-34}$ [Js] and ν is the frequency [Hz] of the radiation. The source is monochromatic.
In XPS the photon is absorbed by an atom in a molecule, leading to ionization and emission of a core (inner) electron. By contrast, in UPS the photon interacts with valence levels of the molecule or solid, leading to ionization by removal of one of these valence electrons. The kinetic energy distribution of the emitted photoelectrons (i.e. the number of emitted photoelectrons as a function of their kinetic energy) can be measured using any appropriate electron energy analyser.

The energetic reaction during the process can be described as follow:

$$A + h\nu \rightarrow A^+ + e^- \tag{3.28}$$

where A represent the atoms in the material under test. Conservation of energy requires that:

$$E(A) + h\nu = E(A^+) + E(e^-) \tag{3.29}$$

Since the electron energy is present solely as kinetic energy this can be rearranged into the following:

$$E_K = h\nu - (E(A) - E(A^+)) \tag{3.30}$$

The final term in brackets, representing the difference in energy between the ionized and neutral atoms, is generally called the binding energy (E_B) of the electron:

$$E_K = h\nu - E_B \tag{3.31}$$

Which means that knowing the energy of photons hitting the sample and detecting the kinetik energy of the eletron photoemitted, it is possible to get information about the binding energy, which is related to a specific atom configuration.[1]

The requirements for a photoemission experiment (XPS or UPS) are:

1. a source of fixed-energy radiation;
2. an electron energy analyser, which can disperse the emitted electrons according to their kinetic energy, and thereby measure the flux of emitted electrons of a particular energy;
3. a ultra-high vacuum (UHV) environment, to enable the emitted photoelectrons to be analysed without interference from gas phase collisions, the order is 10^{-9} mbar.[2]

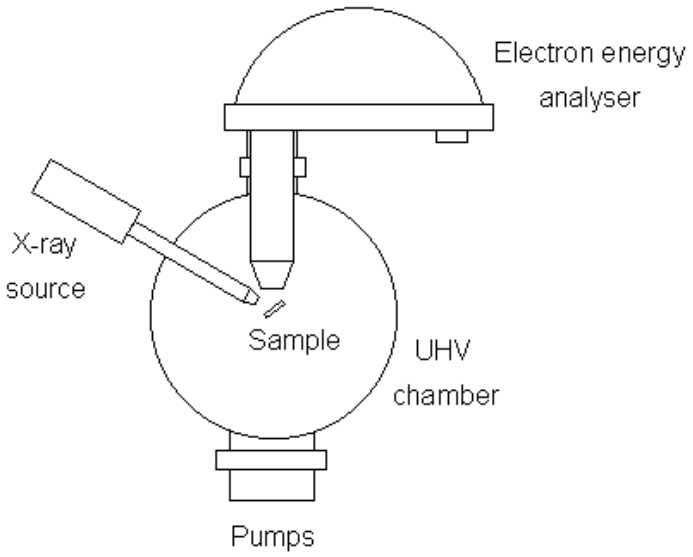

Figure 3.11: System for the XPS experiment - Schematic view of the tools needed for an XPS measurement.

[1] Xps database

[2] During the experiment which has been performed, the samples had to stay in the pumping chamber for more than 12 hours before starting the measure.

3.4 Ellipsometry Measurements

For different recipes we obtain different growing rates. Therefore we have to check the growing rate/thickness of each recipe to provide the same thickness. This technique has been used to check the growing rate of the amorphous silicon layers.

Ellipsometry is a way to evaluate thickness of a material on the nano-order. It is a very good measurement technique since it's contact-less and non destructive for the samples. It is also very sensitive to thickness variations (up to the atom-order).
The measurement exploits the effect of the variation of the polarization of light after hitting the sample.

3.4.1 Theory

Light is an electromagnetic wave travelling in a medium. General light is not polarized which means that electric field does not have any regular pattern as the light is moving. Let's consider the wave travelling as a sum of two perpendicular waves. If those are in phase, then the electrical field will be linear polarized since the sum of the waves will keep the direction of the vector $\vec{E}$ on the same line, see fig. 3.12. Instead if two perpendicular waves are out of phase of 90° then they will be in general elliptical polarized, see fig. 3.14, but in the special case of same amplitudes then the polarization will become circular, see fig. 3.13.

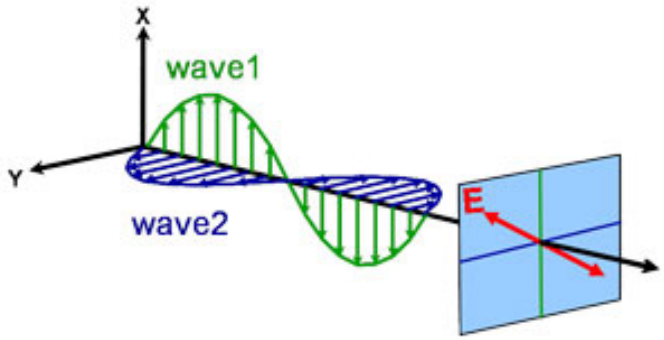

Figure 3.12: Linear Polarization - Orthogonal waves combined to demonstrate polarization: linear.

There are two numbers that describe the travel of the wave in a medium: the refractive index and the extinction coefficient, together they are called complex refractive index

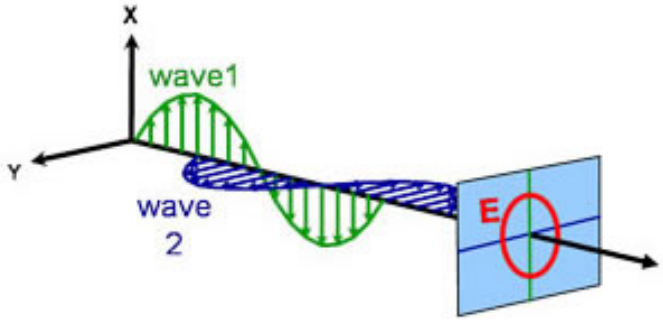

Figure 3.13: Circular Polarization - Orthogonal waves combined to demonstrate polarization: circular.

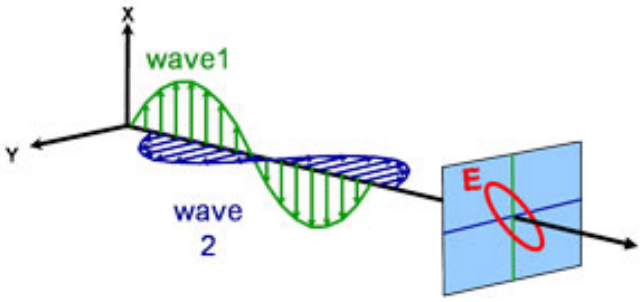

Figure 3.14: Elliptical Polarization - Orthogonal waves combined to demonstrate polarization: elliptical.

which can be written as follow:

$$\tilde{n} = n + i \cdot k \tag{3.32}$$

where n is the refraction index and k is the extinction coefficient.
These quantities describe the speed and the absorption of the wave in the medium. The speed of the wave:

$$v = \frac{c}{n} \tag{3.33}$$

where v is the speed and c is the speed of light. While the absorption coefficient:

$$\alpha = \frac{4\pi k}{\lambda} \tag{3.34}$$

where λ is the wave length.
The intensity of light travelling along the direction z can be described as follow:

$$I(z) = I(0)\exp(-\alpha z) \tag{3.35}$$

It is clear that if $k = 0 \rightarrow \alpha = 0$ (transparent material for that wavelenght) then the exponential is equal to unity and the wave intensity is constant.
The incident angle ϕ_i is equal to the reflection angle ϕ_r while the transmit angle ϕ_t depends on the refraction index through the Snell's law (see fig. 3.15):

$$n_0 \sin\phi_i = n_1 \sin\phi_t \tag{3.36}$$

where n_0 is the refraction index of the medium from which the light is coming from, while n_1 is the refraction index of the medium where the light is travelling toward.
The electrical field will also be reflected and transmitted in a precise way, described by

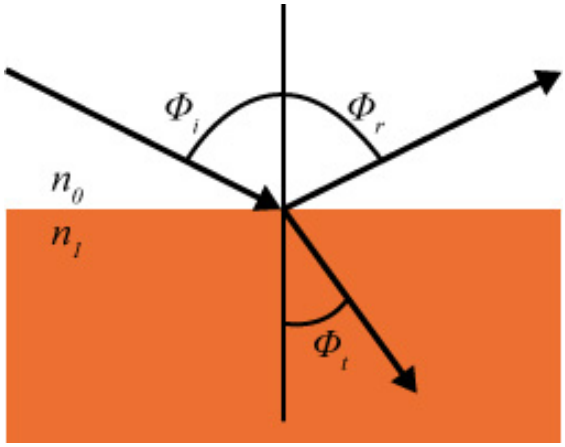

Figure 3.15: Snell's Law - Light reflects and refracts according to Snell's law.

the Fresnel's equations:

$$r_s = \left(\frac{E_{0r}}{E_{0i}}\right)_s = \frac{n_0 \cos\phi_i - n_1 \cos\phi_t}{n_0 \cos\phi_i + n_1 \cos\phi_t} \tag{3.37}$$

$$r_p = \left(\frac{E_{0r}}{E_{0i}}\right)_p = \frac{n_1 \cos\phi_i - n_0 \cos\phi_t}{n_0 \cos\phi_t + n_1 \cos\phi_i} \tag{3.38}$$

$$t_s = \left(\frac{E_{0t}}{E_{0i}}\right)_s = \frac{2n_0 \cos\phi_i}{n_0 \cos\phi_i + n_1 \cos\phi_t} \tag{3.39}$$

$$t_p = \left(\frac{E_{0t}}{E_{0i}}\right)_p = \frac{2n_0 \cos\phi_i}{n_0 \cos\phi_t + n_1 \cos\phi_i} \tag{3.40}$$

Where r and t are respectively the components reflected and transmitted, while s and p are respectively the components perpendicular and parallel to the plane of incident. The angles that the incident, reflected and refracted rays make to the normal of the interface are given as ϕ_i, ϕ_r and ϕ_t, respectively.

In the case of many layers the situation becomes more complicated as the ray will be subjected to several reflection and/or transmission, e.g. see fig. 3.16. The multi-layers

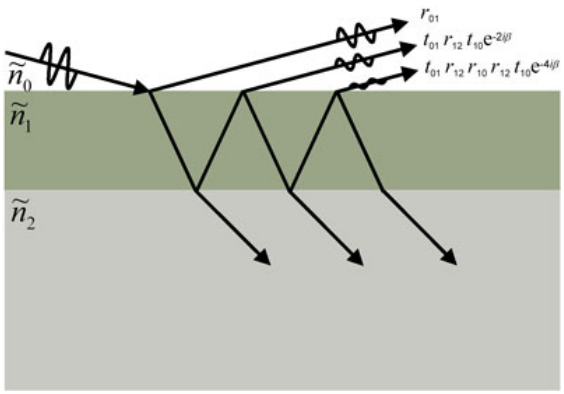

Figure 3.16: Optical interference into multi-layers sample - Light reflects and refracts at each interface, which leads to multiple beams in a thin film. Interference between beams depends on relative phase and amplitude of the electric fields. Fresnel reflection and transmission coefficients can be used to calculate the response from each contributing beam.

case applies to the HIT cells.

A summary of the measurement system is shown in fig. 3.17. The polarizer shown is used to select a certain polarization plane from the starting unpolarized light, this will lead to a linear polarized light which will then become in general elliptical after hitting

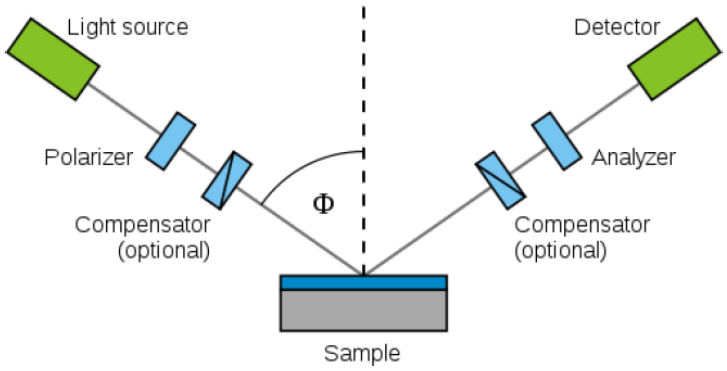

Figure 3.17: Schematic setup of an ellipsometry experiment - Rotating analyzer ellipsometer configuration: uses a polarizer to define the incoming polarization and a rotating polarizer after the sample to analyze the outgoing light. The detector converts light to a voltage whose yields the measure of the reflected polarization.

the sample (from this comes the name *ellipsometry*).
What the instrument measures is the quantity called ρ:

$$\rho = \frac{r_p}{r_s} = \tan(\Psi)\exp(j\Delta) \tag{3.41}$$

Where $\tan\Psi$ is the amplitude of the ratio between the two waves components and Δ measures the phase shift between them. The tool must know the starting polarization and intensity of the s and p components to correctly analyse the results.
Since the measure is sensible to ratios and subtraction between two values it is quite accurate and reproducible, also it is not very susceptible to scatter and lamp fluctuations.

3.4.2 Spectroscopic Ellipsometry

From eq. 3.41 comes clearly that it is possible to obtain two values for each wavelength and for each angle of incident.
In the spectroscopic ellipsometry (which is the tool used in this work) ρ is measured for a certain range of wavelengths (and for several incident angles), the more data acquired let to estimate more parameters through fitting. In fact it is not possible to evaluate optical index and/or thickness directly from ρ but a model has to be established. In the model it is important to indicate all the layers which are present and to put them in the right order, this will let an algorithm to estimate e.g. thickness and refraction index for the sample. If we increase the number of parameters to estimate then more data is

needed for a better fitting.

Data analysis proceeds as follows: after a sample is measured, a model is constructed to describe the sample. The model is used to calculate the predicted response from Fresnel's equations which describe each material with thickness and optical constants. If these values are not known, an estimate is given for the purpose of the preliminary calculation. The calculated values are compared to experimental data. Any unknown material properties can then be varied to improve the match between experiment and calculation. The number of unknown properties should not exceed the amount of information contained in the experimental data. For example, a single-wavelength ellipsometer produces two data points (Ψ,Δ) which allows a maximum of two material properties to be determined. Finding the best match between the model and the experiment is typically achieved through regression. An estimator, like the Mean Squared Error (MSE), is used to quantify the difference between curves. The unknown parameters are allowed to vary until the minimum MSE is reached. The best answer corresponds to the lowest MSE.

The film thickness is determined by interference between light reflected from the surface and light travelling through the film. Interference can be defined as constructive or destructive and it involves both amplitude and phase information. The phase information from Δ is very sensitive to films thickness down to monolayer.
Thickness measurements also require that a portion of the light travels through the entire film and returns to the surface. If the material absorbs light, thickness measurements by optical instruments will be limited to thin, semi-opaque layers. This limitation can be circumvented by targeting with a spectral region with lower absorption. For example, an organic film may strongly absorb UV and IR light, but remain transparent at mid-visible wavelengths. For metals, which strongly absorb at all wavelengths, the maximum layer for thickness determination is typically about 100 nm.

3.5 Electroluminescence

Electroluminescence (EL) is an optical and electrical phenomenon in which a material emits light in response to the passage of an electric current. It is the result of radiative recombination of electrons and holes in a semiconductor. The excited electrons release their energy as photons - light. Higher light intensity corresponds to higher current flow, i.e. higher carriers concentration.

In this work it has been used in order to evaluate the performance of the contact grid: high light emission far from the bus bar means good contacts, i.e. right trade-off between tight grid and diffusion length.

Considering that radiative recombination is dependent on carriers concentration by the factor B:

$$\text{Recombination} \sim B \cdot \frac{n\,p}{n_i^2} = B \cdot \exp\left(\frac{q\,V}{k\,T}\right) \tag{3.42}$$

This shows that EL signal tells (local) voltage.

4

Samples preparation

Preparation of samples is fundamental for a right evaluation of the results. An high repetitive process is required in order to correctly analyse variations of certain parameters. Anyway, since random influence can always be present (e.g. plasma reactions) statistic is also requested to correctly evaluate the results.

The process of cell fabrication is here summarized in order of procedure.

4.1 Laser

This is the first step of the preparation process. Different types of Czochralski (Cz) wafer substrates are used, which are all 3 Ωcm n-type:

- Polished wafers of 4", with a Miller index of $\langle 100 \rangle$.[1]
- Wire saw wafers of 3", having a Miller index of $\langle 100 \rangle$, used for textured samples.
- Wire saw wafers of $125 \cdot 125$ mm^2 pseudo square, and an orientation of $\langle 100 \rangle$, for single side texture.

Since our solar cells are 2.5·2.5 cm^2 the wafers have to be cut into samples of this size. This is done via laser.

Pictures describing the process of laser cutting are shown in figures 4.1, 4.2 and 4.3.

4.2 Texturing and cleaning process

The cleaning process is very important. Dust, oxygen and many other contaminants can ruin the quality of samples by affecting defects and passivation quality.

[1] The orientation of the crystal is defined by the Miller index.

Figure 4.1: Tool for laser cutting - The tool used for laser cutting. On the right side the interface software.

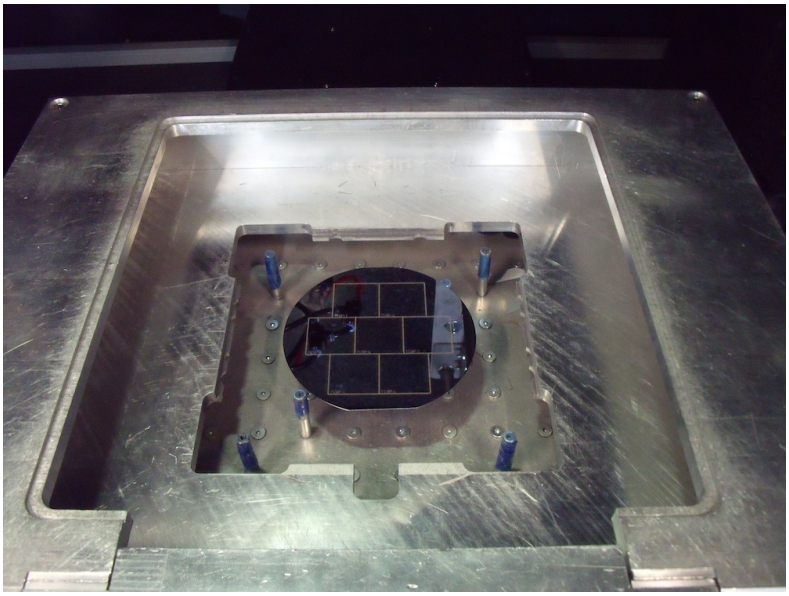

Figure 4.2: Wafer after laser cutting - The wafer is shown after laser cutting. Each cell is $2.5 \cdot 2.5$ cm^2.

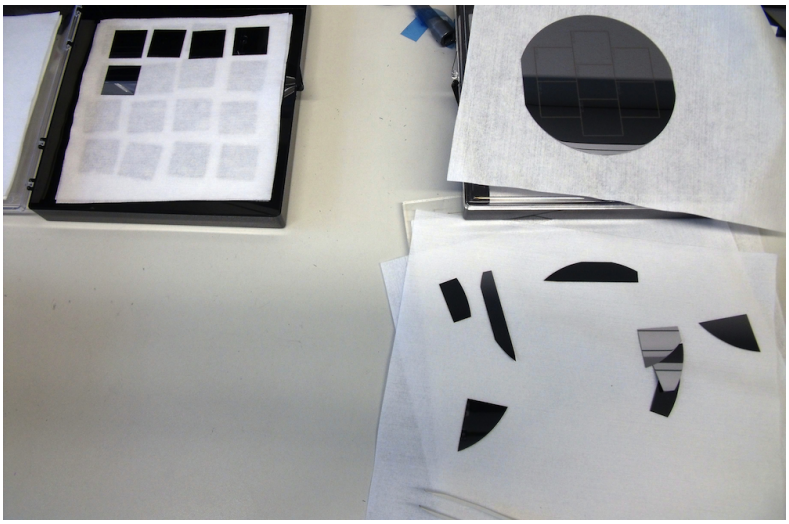

Figure 4.3: Cell polished substrate - Cut wafers have to be manually separated to get the cell substrate.

In the clean room the following steps are performed:

1. *Puratron* cleaning. It is used to remove oil from saw and dirt from laser process.

2. *KOH* cleaning. Potassium hydroxide is a strong base of inorganic compound. It is used to etch the samples removing eventual saw damage.

3. *Texturing* process. This step is *only* performed when we want a pyramidal with $\langle 111 \rangle$ oriented facets structure. A textured substrate improves light absorption, both reducing reflection and increasing internal path. But the interface surface between a-Si and c-Si is increased. This negative feature potentially increase interface defects causing higher recombination and so lower V_{OC}. The amount of (i)a-Si:H needed for passivation is increased. Both these consideration are qualitative shown in Fig. 4.5 and 4.4. For the texturing process KOH, H_2O, $2-Propanol$ and *Alkatex* are used.

4. *RCA* cleaning. The RCA cleaning is a standard cleaning process of silicon wafers in semiconductor manufacturing, which is here shortly reviewed.

   (a) Removal of the organic contaminants (*Organic Clean*). It is performed with $NH_4OH+H_2O_2$ for 10 minutes at ca. 80°C. Since this process may contribute to form oxide layer together with a certain degree of metallic contamination, further phases are needed.

   (b) Deionized H_20 dip for 1 minute.

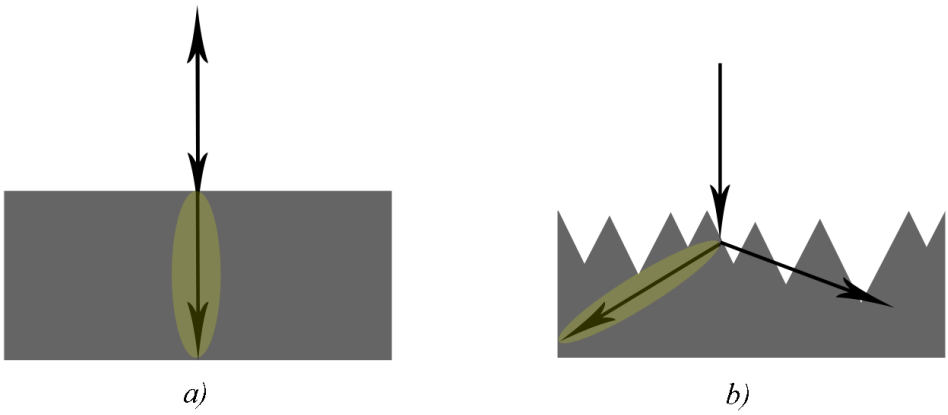

Figure 4.4: Textured vs. Polished: light patterns - A qualitative view of different light patterns rising from hitting polished (a) and textured (b) surface.

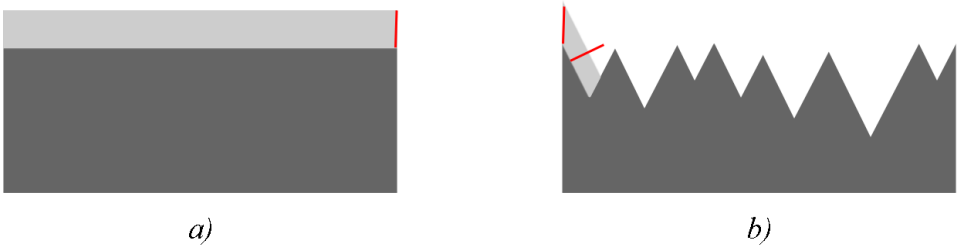

Figure 4.5: Textured vs. Polished: thickness (i)a-Si:H - A qualitative view of the increased thickness needed in a polished (a) and a textured sample (b). The red lines have the same length.

(c) Removal of thin oxide layer (*Oxide Strip*). This phase consists of an HF (1%) dip at ca. 25°C for 1 minute. This step can remove the thin oxide layer and some fraction of ionic contaminants.

(d) Deionized H_20 dip for 1 minute.

(e) Removal of ionic contamination (*Ionic Clean*). It is performed with $HCl + H_2O_2$ for 10 minutes at 75-80°C. This treatment removes the remaining traces of metallic (ionic) contaminants.

(f) Deionized H_20 dip for 1 minute.

(g) HF dip for 1 minute.

(h) Deionized H_20 dip for 1 minute.

(i) Drying with nitrogen.

After the cleaning process the samples are allowed to be introduced in the deposition tool.

An HF dip (followed by deionized H_20 dip and by a nitrogen drying) is always performed just before starting the first a-Si:H deposition and the ITO sputtering, in order to avoid oxygen content on the layers.

4.3 PECVD: a-Si depositions

After the RCA cleaning, the samples are deposited with intrinsic amorphous silicon. The thin (i)a-Si:H layer has mainly the function of improving passivation at the interface of the heterojunction. After that a phosphorous doped a-Si:H layer is deposited on the rear side of the sample. On our n-type wafers this (n)a-Si:H layer builds the base contact and envolves field effect passivation. After that a Boron doped a-Si:H layer is deposited onto the front side of the sample, which forms the emitter. p-aSi:H deposition is performed as the last PECVD step because the $< p >$ layer is more sensitive to high temperature, see table 4.1.

Figures 4.6, 4.7, 4.8 and 4.9 shows a schematic representation of the a-Si:H deposition processes.

We use a PECVD system by Von Ardenne (mod. CS400P) for the depositions of amorphous silicon. A photo of the system is shown in fig. 4.10.

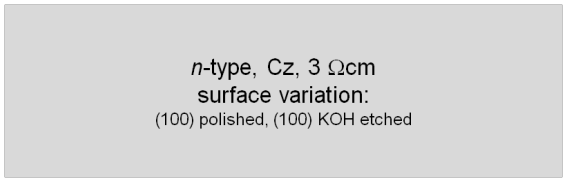

Figure 4.6: First step - Choice of the substrate.

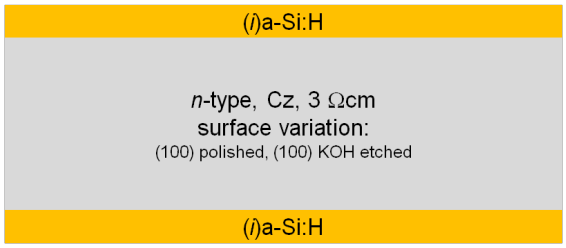

Figure 4.7: Second step - PECVD of the instrinsic a-Si:H layers.

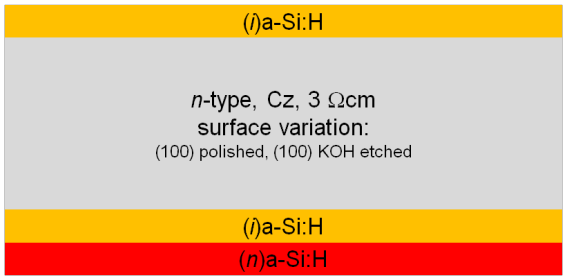

Figure 4.8: Third step - PECVD of the n type doped a-Si:H layers.

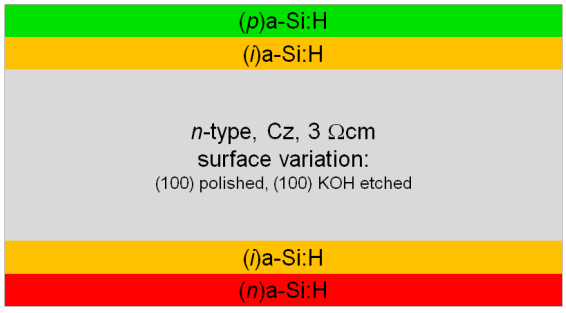

Figure 4.9: Fourth step - PECVD of the p type doped a-Si:H layers.

Figure 4.10: The PECVD system. - The PECVD system used in this work, from Von Ardenne.

For the intrinsic and doped a-Si:H depositions a 13.65 MHz parallel plate PECVD reactor is used respectively, with a diameter of 27 cm. The *standard* deposition parameters are given in tab. 4.1 and 4.2. Plasma power, electrode distance, gas flux and set temperature are the result of optimization of the cell properties. However it is possible to change those values for each deposition.

Table 4.1: Process parameters during a-Si:H depositions. The specified temperature is the set-temperature within the bottom electrode of the deposition system. The sample temperature is expected to be about 100°C lower.

	Set-temperature [°C]	Deposition pressure [mbar]	Electrode distance [mm]	Power density [mW/cm^2]
(i)-aSi:H	300	0.85	50	35
(n)-aSi:H	300	0.85	50	35
(p)-aSi:H	160	0.85	50	35

After the cleaning process the samples are allowed to be introduced in the deposition tool. The steps followed to allow the introduction in the process chambers are the followings.

Table 4.2: Process parameters during a-Si:H depositions.

	SiH_4 flow [sccm]	H_2 flow [sccm]	PH_3 flow [sccm]	B_2H_6 flow [sccm]
(i)-aSi:H	20	100	-	-
(n)-aSi:H	20	88	12	-
(p)-aSi:H	20	84	-	16

- **Load chamber.** This chamber is used to prepare the samples to be introduced into a high vacuum system. This chamber is drained and pumped every time samples are inserted or taken out from the system.

- **Transfer chamber.** This is an intermediate chamber, which keeps the high vacuum and allows to transfer the sample carrier into the correct process chamber.

- **Process chambers.** These are the chambers where the deposition process takes place. They are connected with the gases through valves. Each chamber is used for a particular type of deposition: this is to avoid contamination of gas that may stay in the chamber after the process is ended and which are unwanted for other depositions.
  The chambers contain electrodes to generate plasma, which can be moved to adjust the distance in between. Temperature can also be changed even if, in this work, fixed temperature has been used.

The deposition process consists in:

- Pre-heating steps (10') with H_2. Mainly used to bring the samples to an uniform temperature.

- Adjustment of electrodes distance.

- Process (time related to thickness of the layer). A recipe is used to set the parameters of deposition: after a preliminar adjustment of the gas flux/concentration the process can begin. The growing rate is related to many parameters: power, electrodes distance, gas flux and concentration, temperature. Therefore the process time of one certain recipe has to be adjusted to the wanted thickness of the layer.

- Cleaning. Argon is used to clean the chamber from residuals.

4.4 ITO sputtering

Figure 4.12 shows the tool of Von Ardenne used for sputtering. In figure 4.11 we present a schematic view of the cell at this point of the fabrication process.

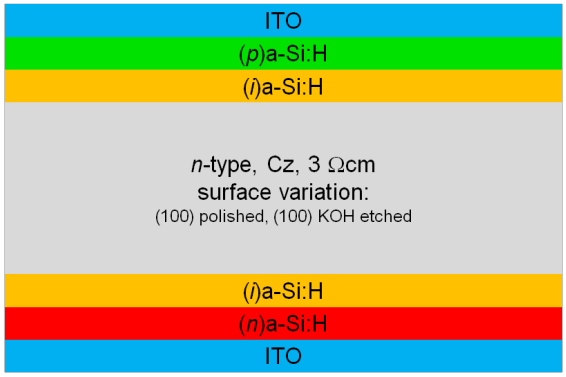

Figure 4.11: Fifth step - Sputtering of ITO.

A transparent conductive oxide is used both for its optical and electrical properties. In this work ITO is used for those purpose, it works as anti-reflection layer and as a good conductor for carrier transportation. An annealing step for 5 min at 175 °C follows the ITO deposition to provide good conductance. In fact the a-Si:H passivation suffers from the ITO sputtering and needs a thermal anneal to reach again excellent passivation quality.

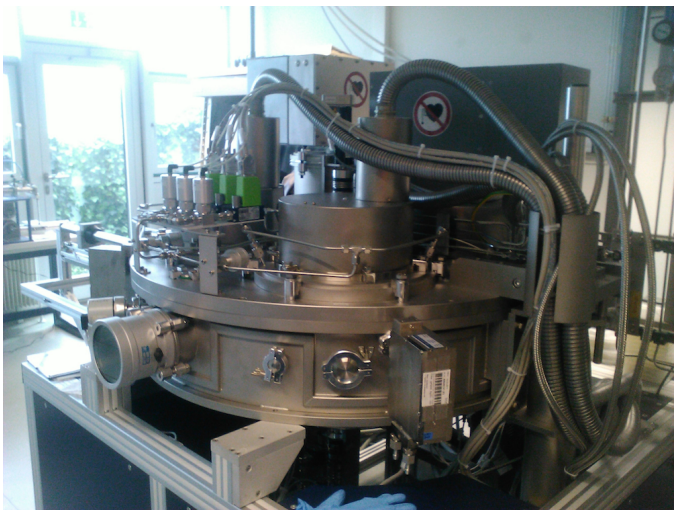

Figure 4.12: Sputtering tool - A picture of the sputtering tools *LS* 900*S* of Von Ardenne.

The sputtering tool uses:

- A *target* composed by 90% of Indium Oxide and 10% of Tin Oxide.[1] ⊘ 249 x 6 mm.
- *Gas* used to hit the target composed mainly by Argon and a small percentage (1-3 %) of Oxygen.

The process consists in:

- Pre-sputtering (2m). In this phase the substrate is screened by a shutter so that no ITO can grow on the sample, but the target is still subjected to plasma treatment. In this way the surface can be made fresher (older process could let unwanted residuals on the target).
- Gas adjustment. A recipe is used to set the parameters of the process (gas flux, time of reaction, power, electrodes distance). In this step the gases are set to the wanted values.
- The shutter is open and the samples can be sputtered with ITO.

4.5 Aluminium evaporation

Evaporation involves two basic processes: a hot source material *evaporates* and *condenses* on the substrate. Aluminium is the source which is evaporated on the cell. Enough vacuum has to be reached to avoid the collision of the particle during the path toward the substrate.
The tool used for aluminium evaporation is shown in fig. 4.13 e 4.14.

Figure 4.15 shows a schematic view of the final cell.

4.6 Screen Printing

In this technique a metal-containing conductive paste is forced through the openings of a screen on to a wafer to form the contacts.
The printing process begins as the cell is placed onto the printing table. A very fine-mesh print screen, mounted within a frame, is placed over the cell; the screen blocks off certain areas and leaves other areas open, where the paste can go through. After a measured amount of paste is dispensed onto the screen, a squeegee distributes the paste over the screen to uniformly fill the screen openings. As the rake moves across the screen, it

[1] The percentuals are based on the weight.

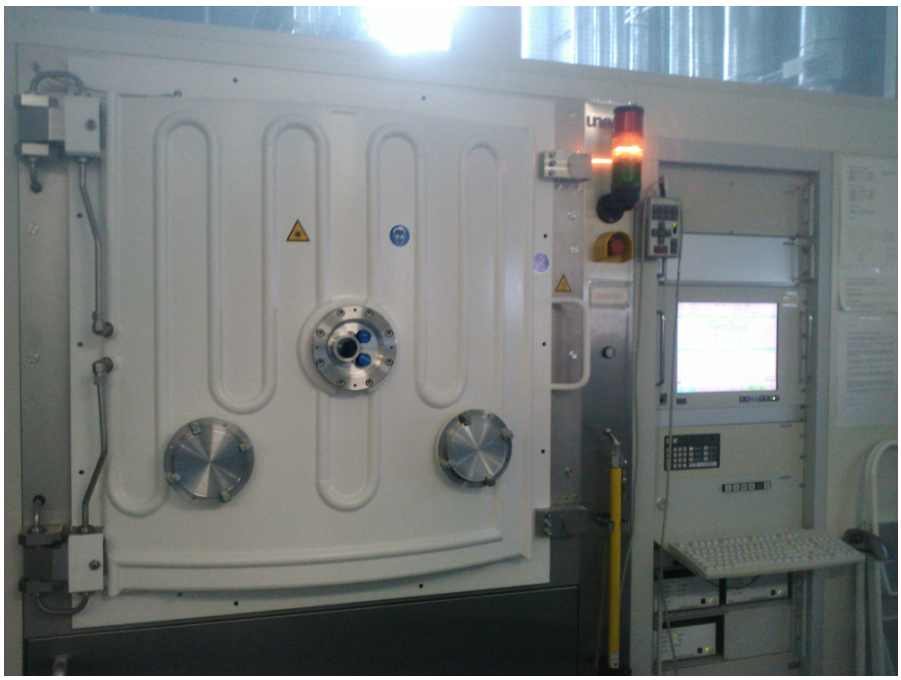

Figure 4.13: Evaporation tool close - The tool used for evaporation of aluminium, on the right the controlling software.

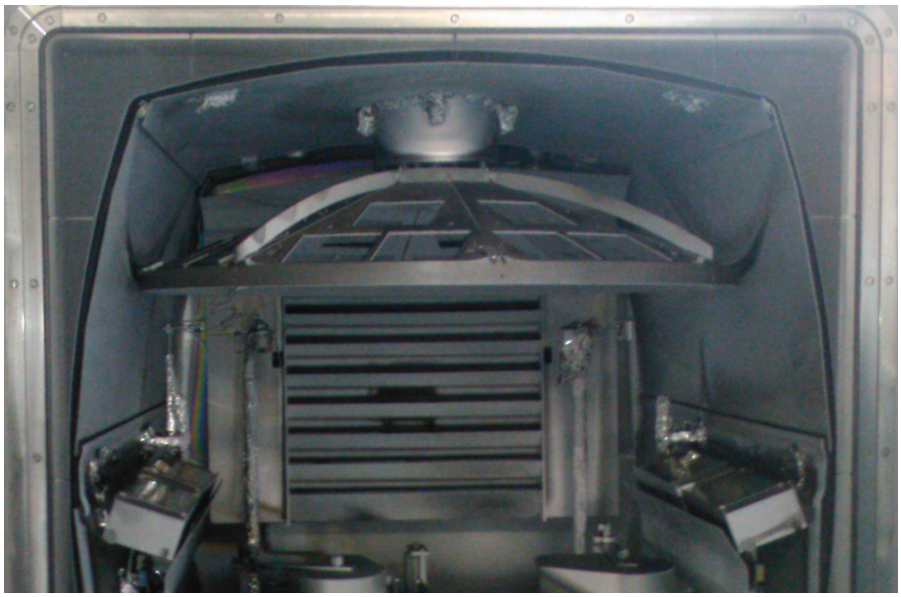

Figure 4.14: Evaporation tool open - The tool used for evaporation of aluminium. The cells are situated on the top and the evaporated aluminium is deposited from the bottom.

pushes the paste through the screen openings and onto the wafer surface. This process must be tightly controlled for temperature, pressure, speed, and many other variables. When all printing steps are completed, the wafer is annealed for 10-30 min at 175-200 °C to get the solvents out of the paste.

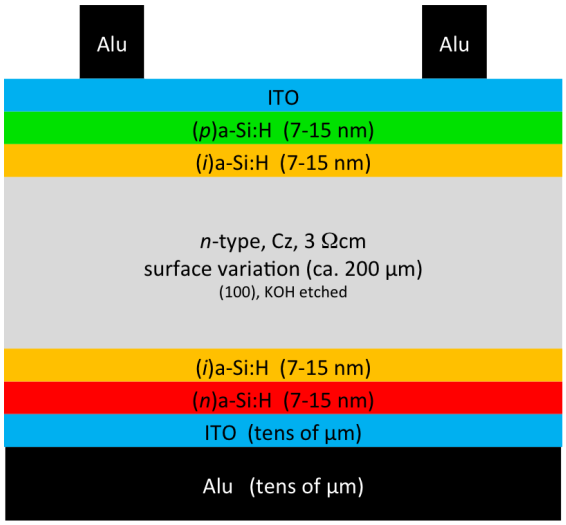

Figure 4.15: Sixth step - *Alu* contact evaporation.

Each step has been followed in this thesis, but most focus and work has been done in the PECVD system for amorphous silicon depositions.

5

Experiments, Results and Discussion

In this chapter the experimental work of the thesis is presented. The experiments have the aim of optimizing and investigating the amorphous silicon layers.

A lot of parameters deeply influence the performance of a HIT cell. Some parameters have then been investigating in order to understand their influence into the cell behaviour and to optimize their value.
The topics of the experiments performed are the followings:

1. Plasma H_2 post-treatment;
2. Oxygen bonding after *HF dip*;
3. Variation of gas time reaction;
4. Variation of the thickness of (i)-aSi:H;
5. Variation of the thickness of (p)-aSi:H.

5.1 H_2 plasma post-treatment investigation

Hydrogen plasma post-treatment is a process in which the samples are treated with H_2 plasma after growing the intrinsic amorphous silicon (SiH_4 + H_2). Hydrogen can diffuse into the a-Si layer, filling dangling bonds, decreasing defects and improving the passivation quality [20].

In previous experiments at ISFH an increase of V_{OC} was found after such an H_2 plasma treatment. Those samples anyway started with a low value of V_{OC} (around 650 mV), and were not used for over a year. The open question was so: is it an improvement that comes from temperature healing benefit? Does hydrogen effectively heal more defects with a further H_2 treatment?

5.1.1 Description

In this experiment we fabricate HIT type solar cells on textured and on polished wafers. We chose two different (i)a-Si layer thicknesses, 5 nm and 10 nm. The 10 nm (i)-layer provides an excellent passivation after the deposition. The question is, if an H_2 plasma treatment can even improve the passivation quality of such thick layers. The 5 nm samples have been chosen to evaluate if a thinner layer could improve hydrogen diffusion to the a-Si / c-Si interface, leading to further healing.
After the (i)a-Si layer deposition we perform the H_2 plasma treatment. We chose six different plasma conditions for the H_2 post treatment which are presented in figure 5.1. The colours from green to red indicate the strength of the plasma from week to strong. After the H_2 post treatment we finished the solar cell with our standard parameters given in section 4.3. The metallization was done via *Al* evaporation. Figure 5.1 shows a schematic representation of the solar cells fabricated in this experiment.
The experiment can be summarized as following:

i-aSi thickness	No PT	P=20 W d = 50 mm t = 180 s	P=50 W d = 50 mm t = 90 s	P=100 W d = 50 mm t = 180 s	P=50 W d = 30 mm t = 90 s	P=100 W d = 15 mm t = 180 s
5 nm (KOH textured and Polished)	x				x	
10 nm (KOH textured and Polished)	x	x	x	x		x

Figure 5.1: H_2 **post treatment investigation** - A schematic view of the experiment done to investigate the effect of hydrogen post-treatment.

- Variation of the plasma Post Treatment condition after fixed (i)a-Si:H deposition (see chapter 4 for details regarding sample preparation);
- Fixed conditions for all the other parameters;

- Monitoring of V_{OC} for passivation;
- Evaluate overall efficiency.

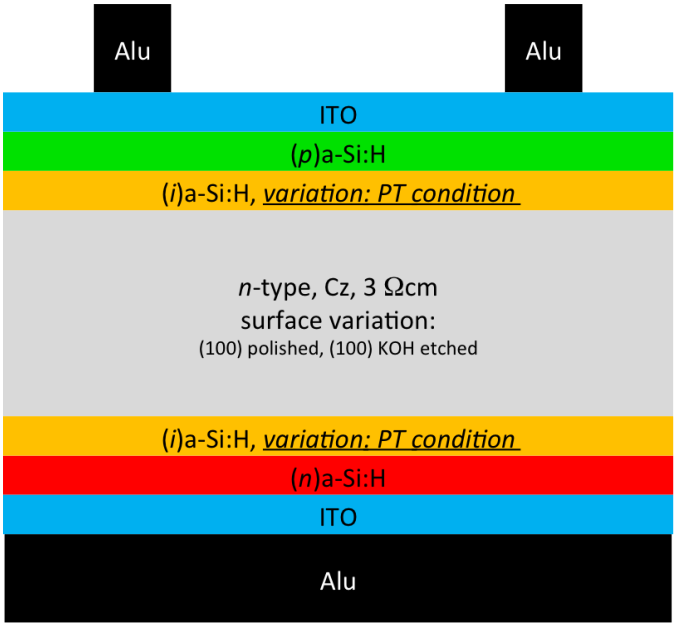

Figure 5.2: H_2 post treatment - Schematic representation of the solar cells fabricated in this experiment.

5.1.2 Results and Discussion

Monitoring of V_{OC} is shown in Fig. 5.3. Where 3 samples for each different condition are reported for a statistical evaluation of the results (some conditions do not provide 3 samples because breaking of some samples have also occurred). In Fig. 5.3 a visual indication of different plasma power is indicated by coloured square on the background; the colours refer to the same conditions reported in Fig. 5.1.

The two graphs on the left hand side show $V_{OC\,impl}$ data for samples with 10 nm (i)a-Si layer. The two graphs on the right hand side show $V_{OC\,impl}$ data for samples with 5 nm (i)a-Si layer. The two upper graphs show our results for textured samples and the two lower graphs for polished samples. The yellow data points represent the $V_{OC\,impl}$ after the (i)a-Si deposition, the green after the (p)a-Si deposition while the blue after the annealing performed after ITO sputtering. The final black points are after the last step, i.e. aluminium evaporation.

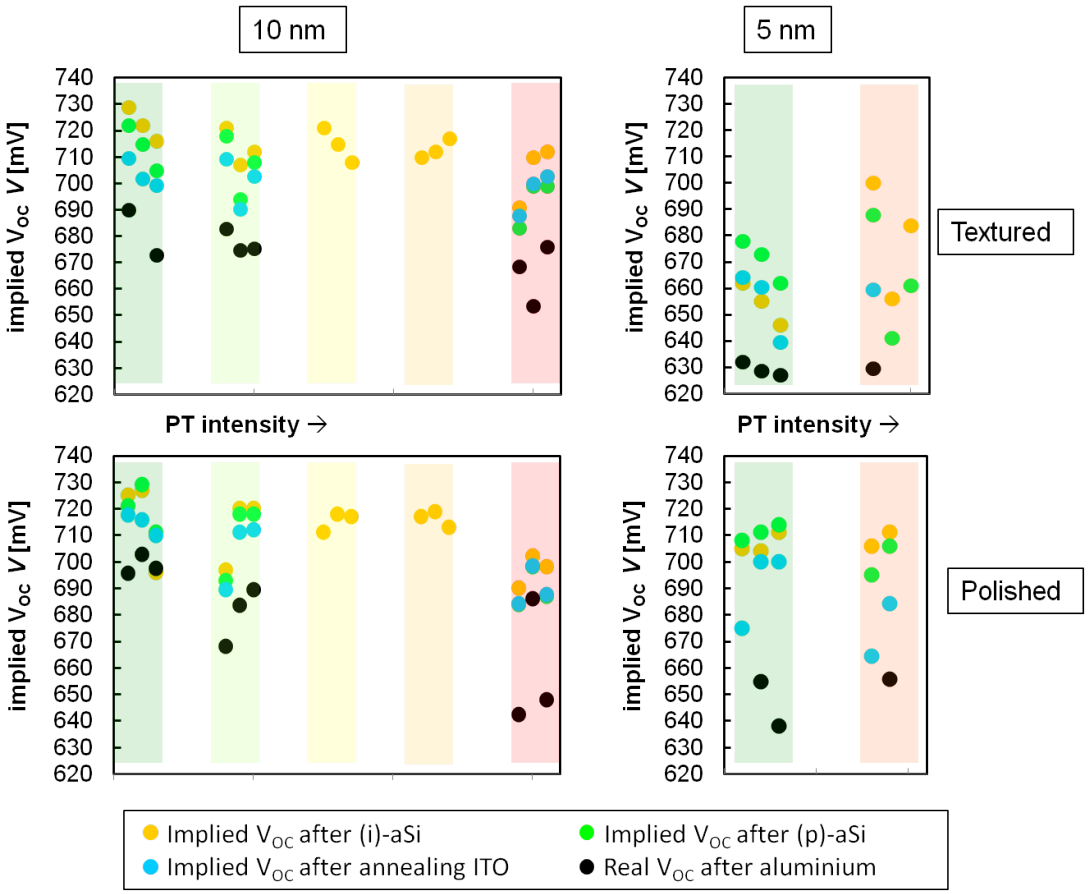

Figure 5.3: V_{OC} **monitoring** - Graph of V_{OC} values during sample preparation in function of different plasma post treatment intensity.

After the 10 nm (i)a-Si depositions (yellow data points in left graphs) we see a decrease of the passivation quality while increasing the plasma power. Nevertheless it is a fact that our samples were already very good even without the PT ($V_{OC} > 720$ mV for 10 nm samples), compared to samples which have been proved to benefit from this kind of treatment in literature [20]. This better starting behaviour can be explained by an high and effective hydrogen content in the amorphous network, already after the deposition process (pre-treatment).
For the 5 nm i-layers we observe a different behaviour. Since we see no decrease or increase of the passivation quality for the polished samples, we see a slight increase of the V_{OC} for the textured samples. The reason could be that the effective thickness of the 5 nm i-layer on textured samples is reduced by a factor of about 1.7 compared to planar surfaces due to the enlarged surface area (see Fig 4.5 in section 4.2). Therefore it could be much easier for the hydrogen to reach the a-Si / c-Si interface and saturate defect states. But it has also been proved that hydrogen is capable of diffuse very deep in the porous structure of the amorphous silicon, so a not very clear conclusion can be carried out. After the (n) and (p)a-Si depositions (green points) the trend for both 10 and 5 nm appears to be more similar, and it shows a slight decrease of the passivation quality while increasing the post-treatment power.
During ITO sputtering, plasma had instabilities and started flittering. Blue points show the implied V_{OC} after annealing of the samples. Their trend is unchanged both for 10 and 5 nm.
The implied V_{OC} of the completed solar cells is represented with black points. The trend for 10 nm samples shows a decrease of the passivation quality while increasing the power of the post treatment. For 5 nm samples, the points show that more power does not lead to a worse passivation.

Instabilities during the evaporation process caused a bad quality metallization, which drastically ruined the passivation. In Fig. 5.3 in fact black circles show (almost always) significantly lower voltages compared to the points of previous conditions. Normally metallization has a neutral or good influence in the passivation quality, because of the positive effect of thermal annealing.
Textured cells which have been fabricated with a standard procedure (without PT) show V_{OC} of about 710 mV.
Instabilities during sputtering and evaporation do not allow to make useful evaluations about other properties such as FF, series resistance and efficiency.

5.1.3 Conclusion

Our samples are already very good even without the PT (V_{OC} of 725 mV for 10 nm samples).This better starting behaviour can be explained by an high and effective hydrogen content in the amorphous network, which appear to be present already after the deposition process (pre-treatment). Also, since increasing plasma power brings to an even worse passivation quality, this could mean that the effect of the plasma is to release hydrogen from the network, increasing defects and dangling bonds.
Therefore for further experiments an hydrogen plasma post treatment will not be performed.

5.2 Oxygen bonding after HF dip

This experiment has been initially performed in order to evaluate possible different atomic structures of the amorphous silicon with and without H_2 plasma PT (e.g. a more or less crystalline silicon). This measurement has been performed in collaboration with the Leibniz University of Hannover.
During the initial measurements an unexpected high peak of oxygen was found, so the purpose of the experiment deviated for its original aim in order to better understand this presence.

5.2.1 Description

This experiment can be summarized as following:

1. n-type cSi substrate (CZ);
2. perform of RCA cleaning and HF dip;
3. deposition of (i)-aSi layer for 60 sec (around 13 nm);
4. HF dip;[1]
5. insertion into the XPS measurement system (about 5 minutes are needed to insert the sample in the controlled -oxygen free- atmosphere);
6. pumping until reaching ultra-high vacuum (approximately for 12 hours);
7. XPS meaurement;

[1]This step and the next ones have been performed at Leibniz University of Hannover.

8. annealing 300°C for 5 minutes (in sito);
9. XPS measurement;
10. annealing 600°C for 5 minutes (in sito);
11. XPS measurement;
12. annealing 800°C for 5 minutes (in sito);
13. XPS measurement.

5.2.2 Results

The first XPS measurement performed is shown in Fig. 5.4. The curve shows the number of electrons counted per second as a function of the bonding energy. Figure 5.5 shows

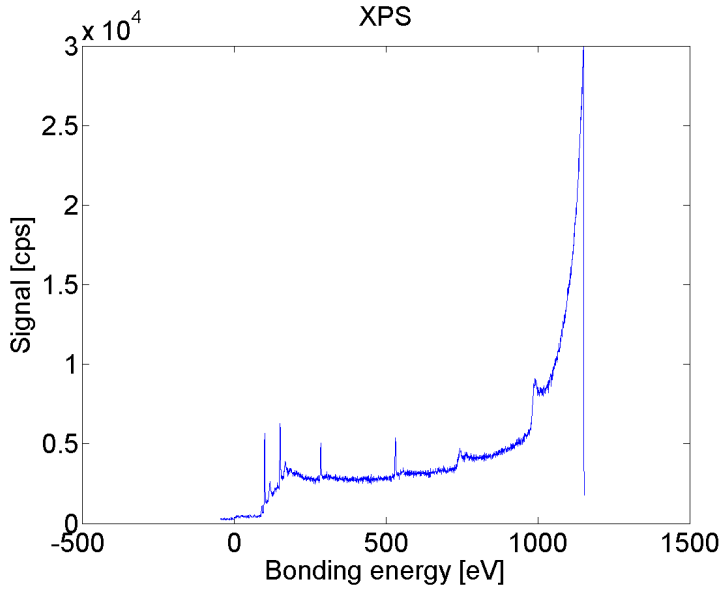

Figure 5.4: XPS - XPS measurement performed in the faculty of physics, Leibniz university of Hannover.

the data acquired after each annealing step.

The pictures show some peaks. Through an XPS database it is then possible to evaluate which atom belongs to the peak, see section 3.3.[1] Details of major relevance are shown in Fig. 5.7 and 5.6 where it is possible to see the presence of silicon, oxygen and carbon (i.e. dust).

In Fig. 5.7 is shown how, increasing the annealing temperature, silicon peaks slightly

[1]The increasing trend of the background is part of the measurement.

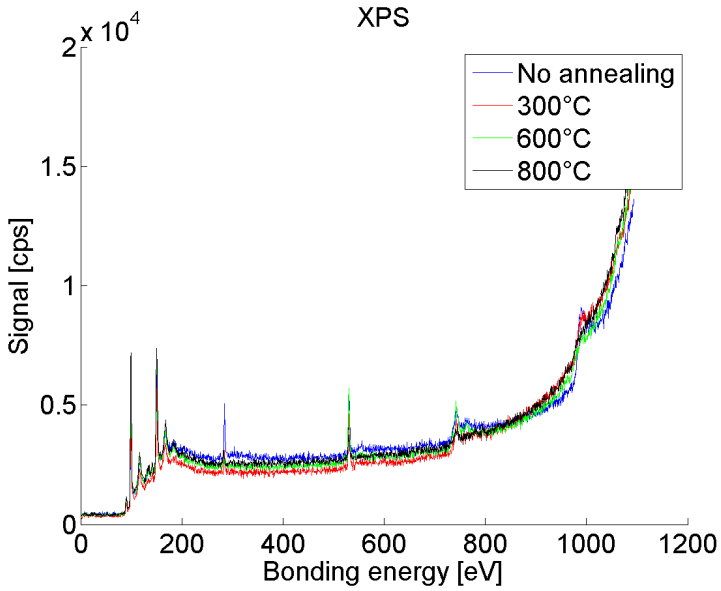

Figure 5.5: XPS - XPS measurement with annealing, including data from different annealing steps.

shift their energy. This is caused by the crystallization of a-Si:H[1], which changes the bonding properties of electrons in the network and so the kinetic energy revealed from the released particles.

Figure 5.6 shows how, increasing the annealing temperature, the oxygen doesn't leave completely the sample, not even for higher temperatures; the oxygen peak in fact changes its maximal value but it does not disappear. Carbon instead leaves almost completely the sample, even after the first annealing step, as proved by the vanish of the peak.

5.2.3 Discussion

The annealing steps help to understand the intensity of the bonding. Even after the highest temperature, a certain quantity of oxygen is still present (proved by the presence of the peak at 800°C, see Fig. 5.6. This proves that oxygen is bonded with silicon, even though not much can be said about the positions of the oxygen in the layer analysed. The depth sensitivity of the XPS goes on the range from 5 to 10 nm of distance from the surface. Which means that oxygen can be detected anywhere in that range. It is possible that oxygen bonds with atoms not at the very surface, thanks to the quite porous

[1]Silicon tends to crystalline after a temperature of 400° C.

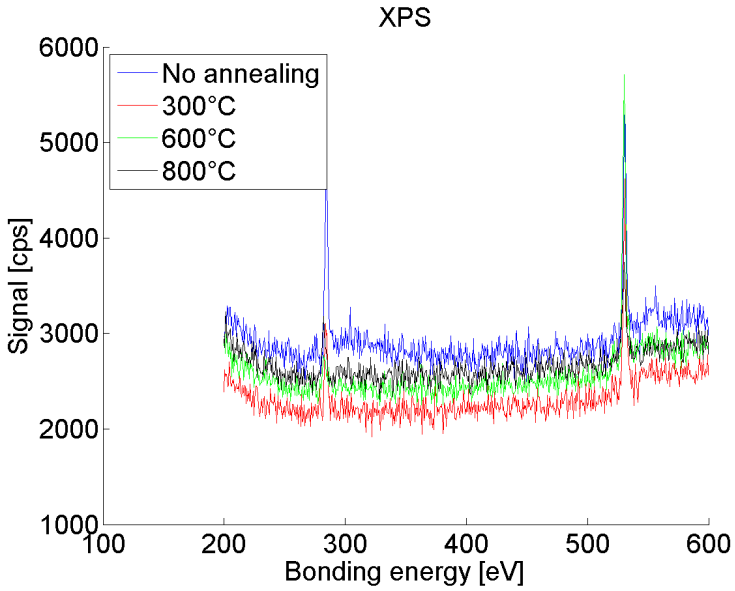

Figure 5.6: XPS measurement, zoom for Oxygen - Graph of the XPS measurement zoomed in the oxigen (ca. 535 eV) and carbon (ca. 275 eV) range.

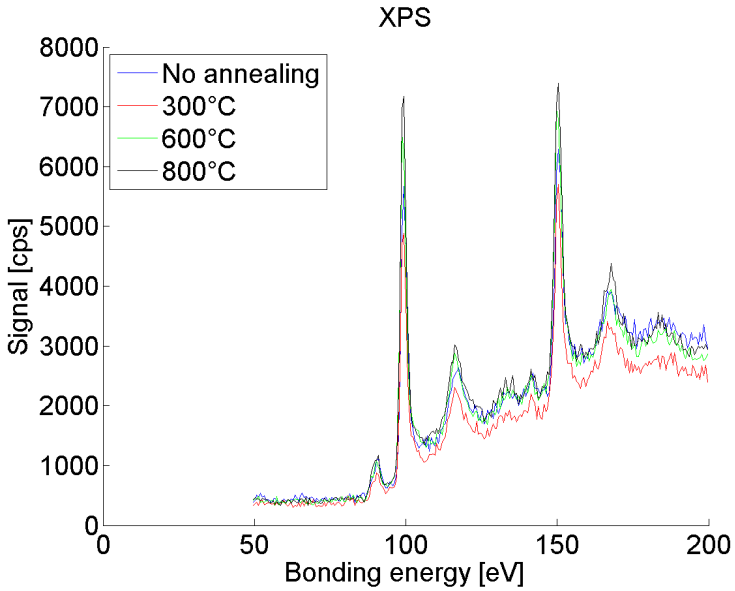

Figure 5.7: XPS measurement, zoom for Silicon - Graph of the XPS measurement zoomed in the silicon range.

structure of the amorphous silicon and that those are detected as difficult to release.

We can give an interpretation of the experiment related with the fabrication process. Analogue conditions of the experiment performed require the cell having an HF dip performed on the top of amorphous silicon. This happens in the fabrication process once the PECVD is completed, which means before the ITO sputtering.
The experiment could then mean that the HF dip performed after PECVD does not exclude the possibility of having oxygen in the amorphous silicon.
Oxygen presence in the amorphous Silicon could then influence: 1) the contact between ITO and a-Si; 2) localized electronic states in the a-Si:H caused by the different atomic structure of the bonding $Si - O$.

Further considerations are difficult to be carried out, and further analysis are required in order to prove other statements.

5.2.4 Conclusions

After the samples have been exposed to air, HF dip could be not enough to guarantee the absence of oxygen in the amorphous silicon layer, especially if the samples aren't inserted fast into a controlled atmosphere.
A fast insertion in vacuum should be performed in order to avoid oxygen diffusion into the layer, or a special container should be used in order to maintain more controlled conditions.

5.3 Gas time reaction variation

Doping of amorphous silicon is not very easily controlled (see section 2.3 and [11]). The concentration of dopant in the growing layer (solid phase concentration) increases with its concentration in the gas used during the deposition (gas phase concentration). Higher solid phase concentration also does not guarantee an higher effective doping, i.e. the dopant could bond without letting any free carrier (the network's coordination number adapts to the doping one).
Many different parameters can influence the effective dopant concentration during the process. For example parameters which could lead to an higher ionization of the molecules (see model in section 2.9), e.g. plasma power, gas concentration, gas time reaction, etc.

In this experiment the doping efficiency has been investigated with a variation of the gas time reaction, i.e. the gas flux inside the process chamber has been changed, while keeping the same pressure and the same ratios between different process gases.

5.3.1 Description

We fabricate solar cells with the standard parameters reported in section 4.3, except for the p-layer. The variation of the process parameters of the p-layer are shown in Fig. 5.9. The time of deposition is changed in order to maintain the same thickness, since the growing rates change with gas concentration.[1] The experiment can be summarized as following:

- Variation of gas concentration for (p)-layer deposition;
- Fixed conditions for all the other parameters;
- Monitoring of V_{OC} for passivation;
- Evaluate overall efficiency.

A schematic cross section of the solar cells is shown in Fig. 5.8.

5.3.2 Results

Monitoring of V_{OC} in function of gas flux quantity is shown in Fig. 5.10 where 3 samples have been produced for each different conditions for statistic purpose. Increasing gas flux quantity (from left to right) implies a reduction of time reaction. The colours of the squares on the background of the graphic remark the same conditions expressed in Fig. 5.9.
In Figure 5.10, 3 set of data points are shown. The yellow points are measured after the (i)a-Si:H deposition with the QSSPC technique and they report an implied V_{OC}; the same measurement is performed after the (p)a-Si:H deposition which is represented with green points, while the black points report a real V_{OC} and are performed with the LOANA tool after aluminium contacting evaporation.
The yellow points should ideally be identical since they are all treated with the same condition of deposition. For this reason, samples which are far from the average shouldn't be considered since they could have been damaged during the cutting or the cleaning

[1] Ellipsometry measurements have been performed for each recipe in order to evaluate the growing rates.

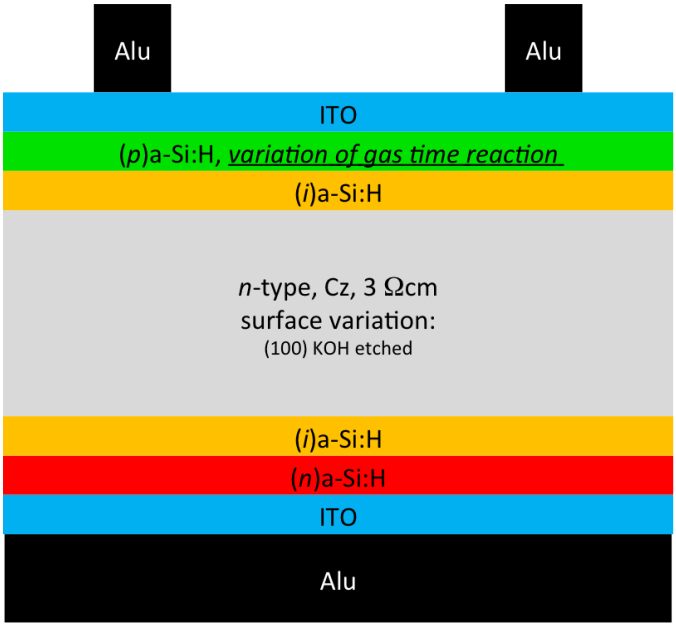

Figure 5.8: Gas time reaction - Schematic cross section of the solar cells fabricated in this experiment.

Long time gas reaction	Default time gas reaction	Short time gas reaction
Concentration = 10 sccm SiH_4, 8 sccm B_2H_6 , 42 sccm H_2. Time = 39s	Concentration = 20 sccm SiH_4, 16 sccm B_2H_6 , 84 sccm H_2. Time = 32s	Concentration = 40 sccm SiH_4, 32 sccm B_2H_6 , 168 sccm H_2. Time = 24s

Figure 5.9: Investigation of gas time reaction - A schematic view of the experiment investigating the effect of gas time reaction into the cell overall efficiency.

process and they would not give valuable information for the experimental purpose. In figure 5.10 one bad sample is cut out (red line). The average of the remaining yellow points has approximately a constant value, as shown by the yellow line.
After the (p)a-Si:H depositions we see a common lowering of implied V_{OC} for all the samples. This decrease of quality is less pronounced for samples which make use of the highest gas flux. As a consequence, the trend of the average shows a increase of the passivation quality for samples treated with less time reaction, shown by the green line. Aluminium evaporation seems to heal the bad sample which was not considered earlier. This singular improvement could come from a beneficial annealing treatment. The best values still come from the lowest time reaction (highest flux).

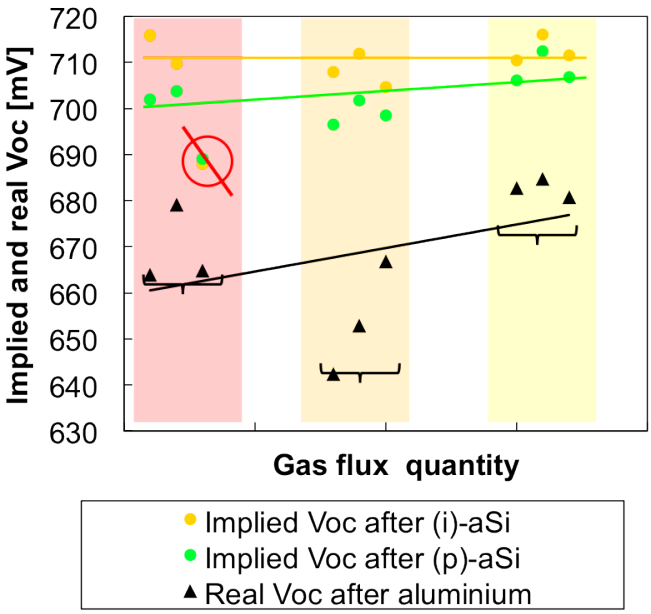

Figure 5.10: V_{OC} monitoring - V_{OC} monitoring for gas time reaction experiment. Different colours of the squares represent the different gas flux: from left to right the gas time reaction decreases.

5.3.3 Discussion

Different performances should come from a different efficiency of doping. A variation of the Fermi energy position leads in fact to a different field effect passivation, together with different influence on the bonding energy of silicon with hydrogen.
From the results, a changing on the V_{OC} is slightly seen. Comparing the implied V_{OC} after (i)-aSi (yellow points) and after (p)-aSi (green points) a general decrease of passivation

quality is constant. The doping layer in fact influences the defects of the (i)-aSi since the Fermi energy shifts. This consideration leads to consider that a changing of the passivation quality could come from a different Fermi position of the p-layer (we remark that thickness is not varied). Two different phenomenons could come from a different Fermi level position:

1. A less implied 'p' type (i)a-Si:H could have less interface defects. This is why in fact the intermediate intrinsic layer is needed.

2. A less effective doped (p)a-Si:H could give less electrical field at the junction.

The two effects appear to have opposite influence on the performance of the cell. Further investigation should be performed in order to evaluate the hypothesis of a different doping efficiency, e.g. XPS could give an estimate of the Fermi energy shifting, through monitor of the peak shifts.

5.3.4 Conclusion

Increasing the gas flux generally increases the quality of passivation. The highest gas flux is then used as our standard recipe for (p)-layer depositions.

5.4 Variation of the thickness of (i) and (p) aSi:H

This experiment has the aim of optimizing the thickness of the intrinsic and doped $< p >$ layers. The analysis has been done on the front side because of it's higher relevance for the cell behaviour.
Thickness of (i) and (p) layers has a lot of influence on the performance of the cell. For example thicker intrinsic layers should lead to a better passivation since they should heal an higher amount of interface defects. At the same time, the intrinsic layer has high resistivity, which implies higher series resistance and less FF for thicker layers.

5.4.1 Description

The experiment details are the following:

- Variation of the front side (i)a-Si:H layer thickness ($d_{<i>}$): 8.7 and 15 nm;

- Variation of the (p)a-Si:H layer thickness ($d_{<p>}$): 8.7 and 15 nm;

- Fixed thickness for (i)a-Si:H on rear side and (n)a-Si:H layer;
- Fixed values for all other parameters;
- Monitoring of V_{OC} for passivation;
- Evaluate overall efficiency.

A schematic cross section of the fabricated solar cells is shown in Fig. 5.11.

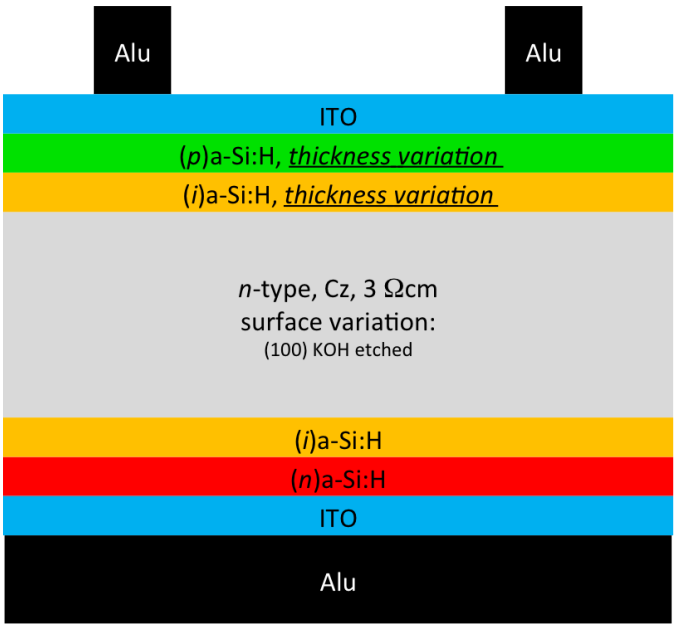

Figure 5.11: (i) thickness variation - A schematic cross section of the fabricated solar cells.

5.4.2 Results

Monitoring of V_{OC} is shown in Fig. 5.12, where 4 samples are analysed for each different condition.
Green points report the implied V_{OC} after (p)a-Si:H depositions, blue points after ITO sputtering. Black points report V_{OC} after aluminium evaporation. In this experiment we haven't performed measurements betweeen PECVD depositions: we were in fact interested in the overall performance, and the passivation quality is better when no measurements are performed between deposition processes.

The passivation quality appears to be good for all values used except for a thickness $d_{<p>} = d_{<i>} = 8.7$ nm.

The V_{OC} after aluminium evaporation (black points) is very good, expect for the worst

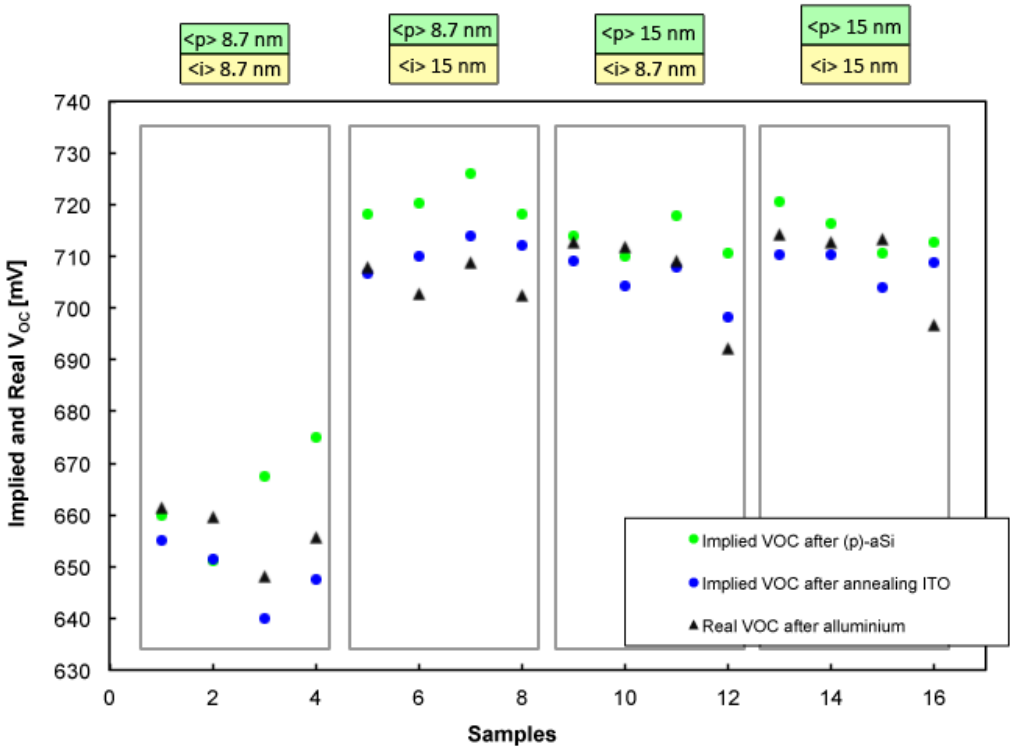

Figure 5.12: V_{OC} monitoring - V_{OC} monitoring for different $< i >$ and $< p >$ thickness.

condition i.e. double thin layers. The best value comes with 15 nm for both layers and it is above 714 mV.

Some issues occurred during the metallization process, indeed 2 different types of masks have been used: one with too thin and one with too thick fingers. That leads to different (electronic) properties like series resistance, contact ITO-grid, optical shading,... of the solar cells. It is therefore difficult to directly compare these cells with different aluminium grids.

Figure 5.13 shows the V_{OC}, J_{SC}, R_{series} and the efficiencies of all cells. Blue points refer to both 8.7 nm layers, red points to 15 nm $< i >$ and 8.7 nm $< p >$, green points to 8.7 nm $< i >$ and 15 nm $< p >$, purple points to both 15 nm.

J_{SC} is reported in Fig. 5.13 (b). Some scattering are evidently caused by the two different masks: lowest values of J_{SC} in the same thickness group has also the lowest value of series resistance, see Fig. 5.13 (c). That happens because with a thicker finger mask, the increased shadow decreases the J_{SC} but the thicker metal conductor decreases the

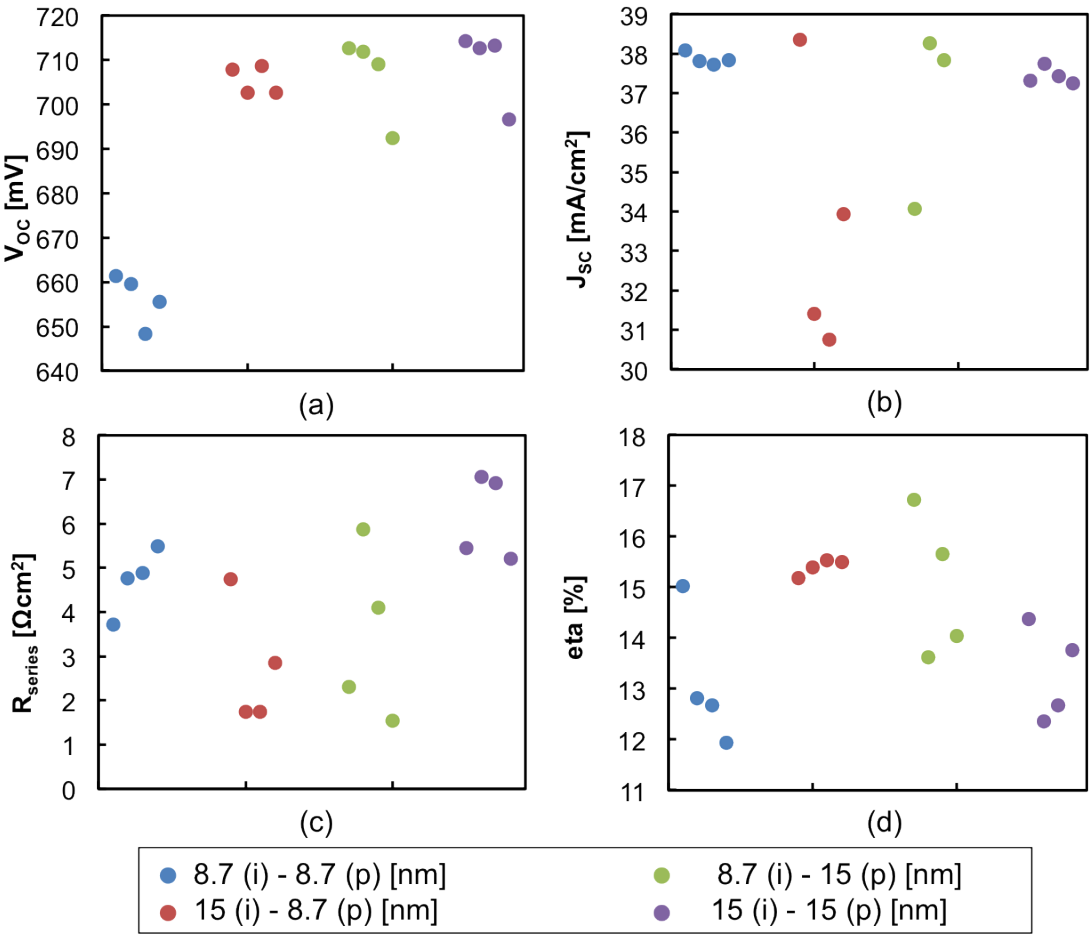

Figure 5.13: Overview - Overview of the cell performance for $< i >$ and $< p >$ thickness variation.

series resistance. The same is true for the opposite: thin fingers lead to high J_{SC} and high series resistance.

From the graph in Fig. 5.13 (b) we see that a **thick $< i >$ layer does not cause a reduction of current**. J_{SC} for both thick layers (purple points) in fact does not show a significant decrement. The best efficiency comes from an $< i >$ layer of 8.7 nm and a $< p >$ layer of 15 nm, as showed in Fig. 5.13 (d). In Fig. 5.13 (c) the series resistance is evaluated at the MPP and through the *double light* method.

5.4.3 Discussion of the experiment

Bad metallization makes difficult to correctly analyse the data. For this reason, another experiment (reported in section 5.5) has been performed, which anyway deals with a variation of the only (i)a-Si:H thickness.

A way to further analyse these results, possibly avoiding the effect of bad metallization is to analyse only samples which have been subjected to the same mask. Since not enough cells with thick fingers have been fabricated, sample with thin fingers are considered.
In Fig. 5.14 an overview of the performance for samples having the same finger thickness is reported.
Zooming into the short-circuit current (Figure 5.14 (b)) shows that J_{SC} slightly decreases while increasing the layers thickness. The series resistance shows the same (more evident) trend.
The FF analysis reported in Fig. 5.15 though, seems to show a not so clear trend. Better statistic would help to evaluate with less uncertainty the best value of FF. The average trend seems to show anyway a maximum FF for asymmetric thickness, which is coherent with η. The best efficiency comes in fact from a thin $< i >$ and a thick $< p >$.
The pFF shows best values for combination of both thick layers, which proves the best passivation achieved in this condition. Series resistance becomes the bigger problem to solve with a thick intrinsic layer, as shown in Fig. 5.14 (c), which limits the FF and so the efficiency.[1]

[1]Series resistance is altogether very high because of the very thin fingers.

To prove the potential of the cells obtained, a rough calculation of the expected efficiency is here presented. V_{OC} and J_{SC} of the solar cell having the best pFF are reported in tab. 5.1. If we pretend to have a FF of 75%, which has been achieved in a lot of other previous experiments, the efficiency obtained would be:

$$\eta = \frac{J_{SC}\, V_{OC}\, FF}{1\, Sun} = 20\% \tag{5.1}$$

which would be the best HIT cell fabricated until now at the ISFH. Issues reasonably referred to high resistance of thin fingers (see section 5.4.3.1) lead to a $FF = 53.96$ %, which implies an efficiency $\eta = 14.38$ %.

Table 5.1: Values of the best solar cell.

$< i >$ [nm]	$< p >$ [nm]	V_{OC} [mV]	J_{SC} [mA/cm^2]
15	15	714.2	37.32

5.4.3.1 Electroluminescence characterization

In order to prove the entity of the issues regarding metallization, electroluminescence measurement has been performed (see section 3.5 for more details about this measurement technique). The measures are shown in Fig. 5.16(a), 5.16(b) and 5.16(c). They show different electrical transport properties of a cell having: good metallization (from another experiment) in Fig. 5.16(c); too thick fingers in Fig. 5.16(a); too thin fingers in Fig. 5.16(b).

- In Fig. 5.16(a) the too thick fingers lead to a very thin red region (higher light emission) between the fingers, which proves the very thick shadow area. The fingers appear yellow in the figure: light emission comes from radiative carriers recombination below the fingers, the radiation is not completely absorbed by the metal above and so a yellow intensity is shown in the picture. The horizontal bus bar does not show much problems.

- In Fig. 5.16(b) the fingers seem not to transport much carriers. The radiative recombination occurs only thanks to the carriers flowing from the bus bar, since light emission mainly happens in the region around it.

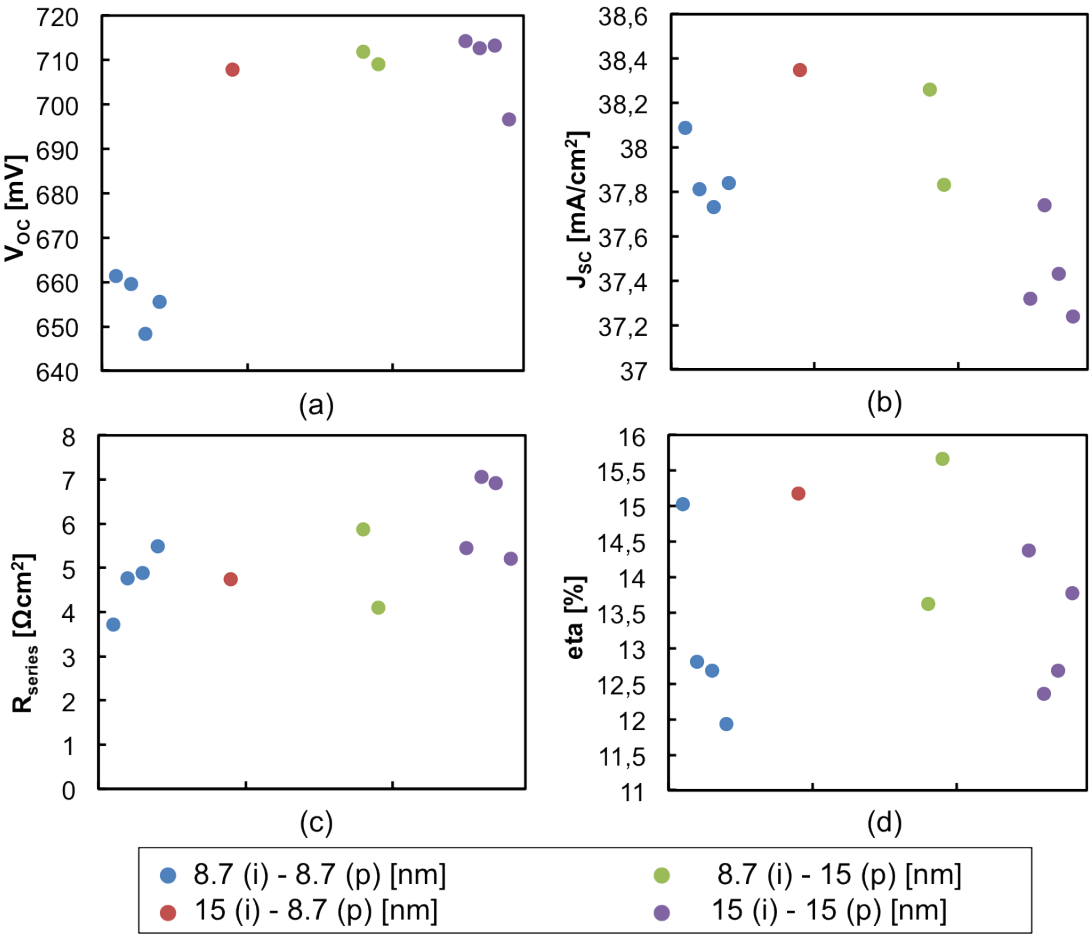

Figure 5.14: Overview - Overview of the cell performance for $< i >$ and $< p >$ thickness variation. Thick fingers samples are not shown.

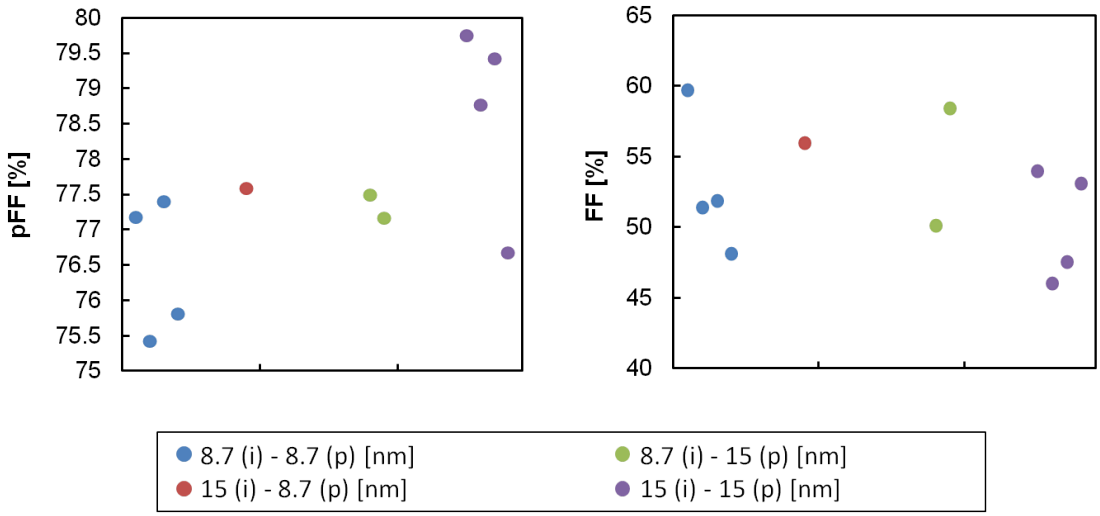

Figure 5.15: FF and pFF - Analysis of FF and pFF for different $< i >$ and $< p >$ thickness. Thick-finger samples are not shown.

- In Fig. 5.16(c) the carriers are able to reach in good quantity almost all the area of the cell. The intense radiative recombination (red) is also quite wide which prove that the fingers are not too thick.

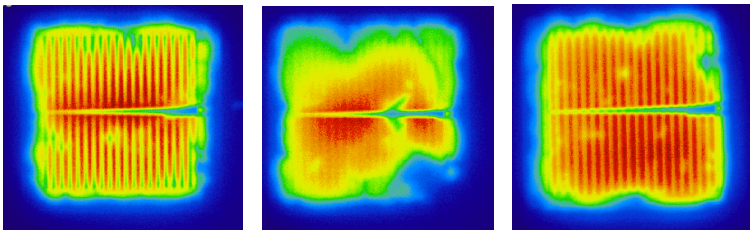

(a) A solar cell with too thick fingers.

(b) A solar cell with too thin fingers.

(c) A solar cell with good size fingers.

Figure 5.16: Electroluminescence measurements.

5.4.3.2 Series resistance analysis

The series resistances at the MPP in function of different thickness of the $< i >$ and $< p >$ layers are shown in Fig. 5.17.

The same graphs, without the samples having too thick fingers are reported in Fig. 5.18. The latter, having in fact an unique mask, will be considered in the next considerations.

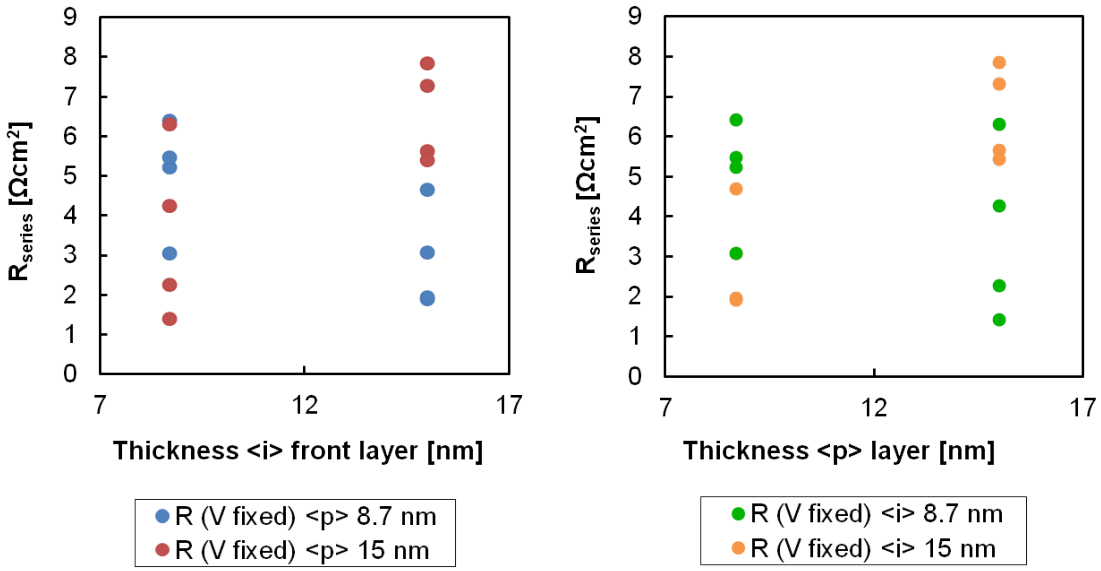

Figure 5.17: Series resistance - Series resistance analysis for different thickness of $< i >$ and $< p >$ layers. The voltage fixed is at MPP.

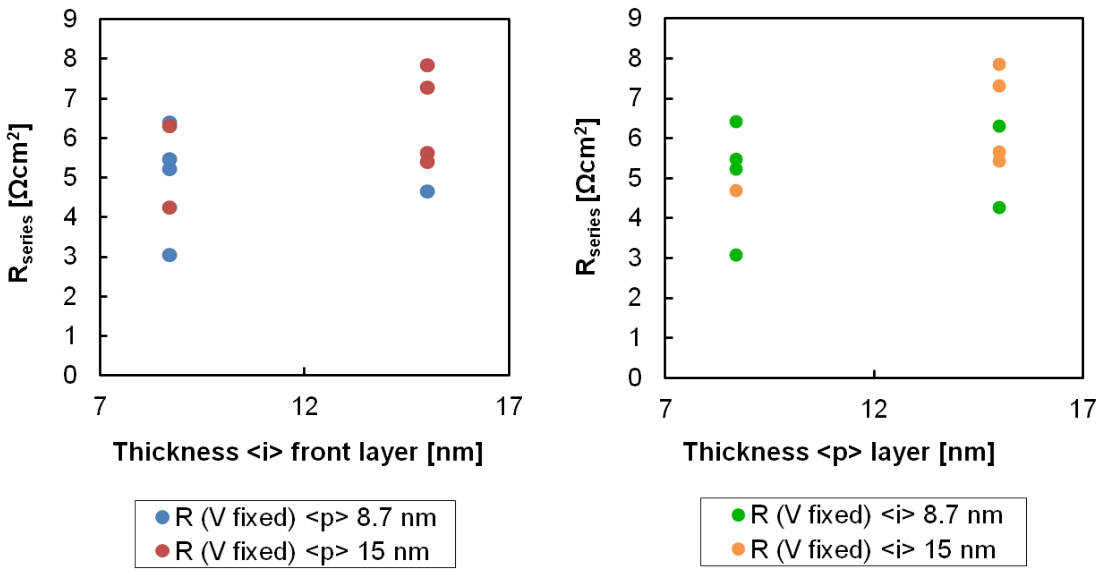

Figure 5.18: Series resistance - Series resistance analysis for different thickness of $< i >$ and $< p >$ layers. The voltage fixed is at MPP. Thick finger samples are not shown.

Each point in the graph represent the series resistance for one sample. The lack of statistics for some conditions unfortunately does not allow to draw much conclusions from the graphs. Anyway the series resistance seems to increase both increasing $< i >$ and $< p >$ layers.

Another plot is presented in Fig. 5.19 where the series resistance is obtained for different voltage and current through the *Light* IV/J_{SC}-V_{OC} method (see section 3.2.4). In these graphs a value of current $I = -100$ mA and a voltage $V = 0.55$ V are fixed, then the resistance is plotted in function of V_{OC} and pFF respectively.[1] In Fig. 5.18 (a),

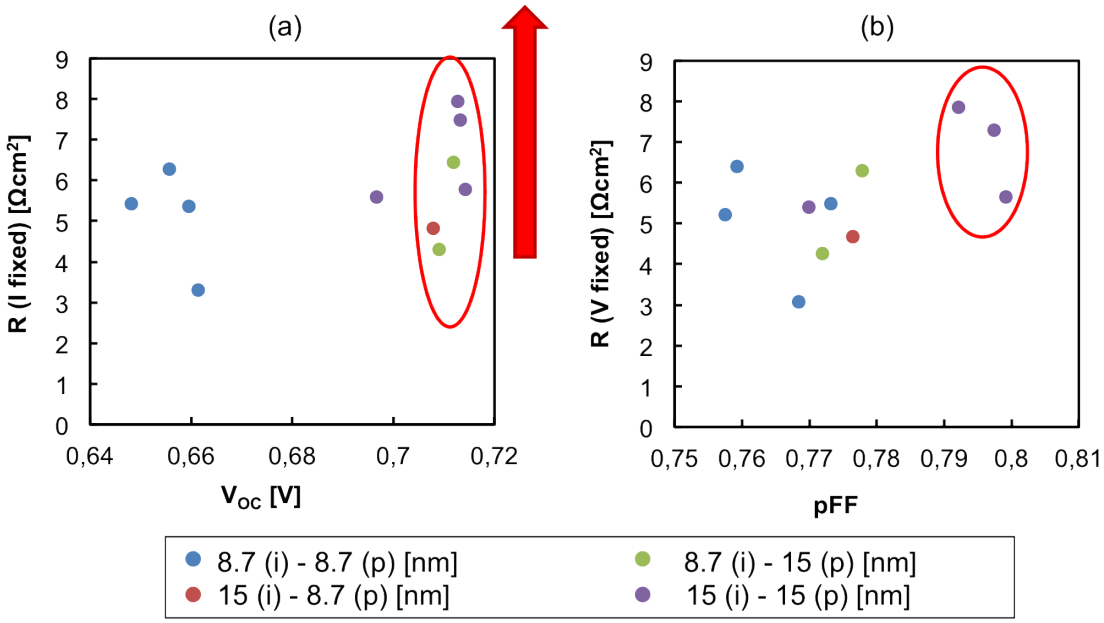

Figure 5.19: Series resistance - *a*) fixed value of current ($I = -100$ mA) - the series resistance is reported in function of the V_{OC}; *b*) fixed value of voltage ($V = 0.55$ V) - the series resistance is reported in function of the pFF.

for quite high V_{OC} the series resistance varies a lot in function of the different thickness. The red arrow shows a big increment of series resistance, while keeping almost the same V_{OC}. An optimal value for the resistance comes from a combination of thin $< i >$ and thick $< p >$ (green circles in Fig. 5.19). Even if the only value available for a thick $< i >$ and a thin $< p >$ appears to be very close to the optimal and the lack of statistic does not allow a clear conclusion.

The similar values of series resistance for thin $< i >$ and thick $< p >$ and the viceversa shows that the thickness rather than an eventual change of the carrier (holes) concentration is mainly responsible for the series resistance value. In Fig. 5.18 (b), the highest

[1] Changing the fixed values for voltage and current does not change the trends of the series resistance.

series resistance corresponds to the highest pFF, which implies that the good passivation which comes from the thickest (i)-aSi:H also causes the highest series resistance and a low FF. A compromise between those leads to an optimum.

5.4.4 Simulations of the different thickness conditions

To deeply investigate the different thickness conditions, the emitter of a HIT cell has been reproduced through the simulation tool *PC1D*. [1] The layers in the structure are, from left to right: ITO, (p)a-Si:H, (i)a-Si:H and (n)c-Si. It is worth to note that *PC1D* does not allow the inclusion of a pseudo-realistic distribution of states into the band gap to better simulate amorphous silicon. Beside that, the tool simulates quite good the heterostructure .
Some parameters chosen for the simulations are reported in tab. 5.2 ($*$ TCO doping is only used to simulate a metal).

Table 5.2: Parameters used for PC1D simulation.

	Doping [cm$^-$3]	Band Gap [eV]
(i)-aSi:H	-	1.7
(p)-aSi:H	10^{18}	1.7
(n)-cSi	10^{16}	1.12
TCO	$10^{21}*$	3.7

The simulations performed are shown in Fig. 5.20. Each condition will be analysed in more details in the following sections.

5.4.5 Discussion of different thickness conditions

1. **thin (p) - thin (i)** ($tp - ti$).[2]

   Real behaviour

   Experimentally this case has showed a bad passivation quality with a relative low

[1] PC1D is a simulation tool available for free from the website of the University of South Wales - Sydney.

[2] The qualitative presentation of the heterostructure does not require a thin and a thick dimension which matches the real values used in the experiment. Anyway a thin layer here is simulated with 8.7 nm while a thick layer with 25 nm, to make more evident the influence of a thicker layer.

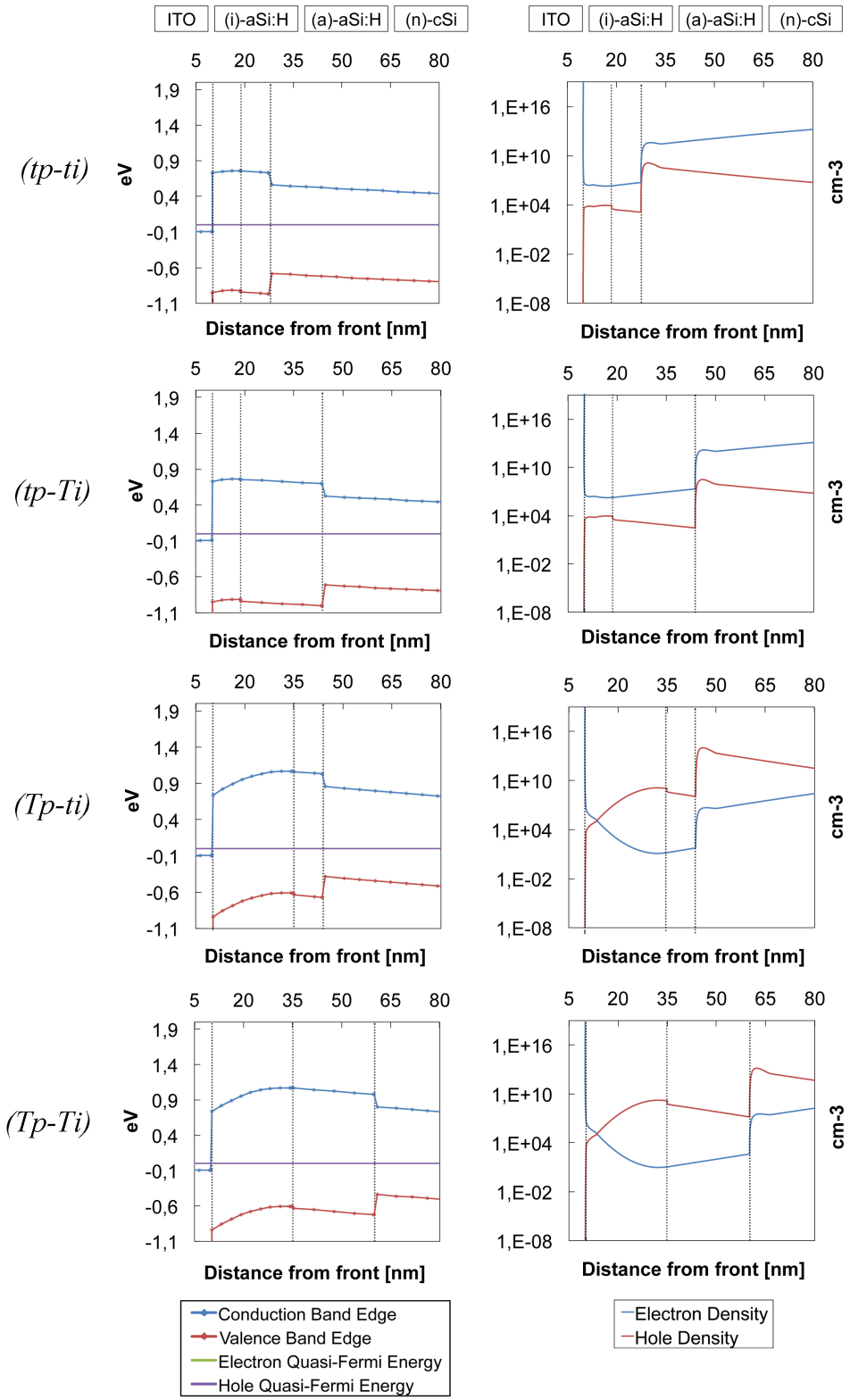

Figure 5.20: Simulations - Different thickness of $< i >$ and $< p >$ layers.

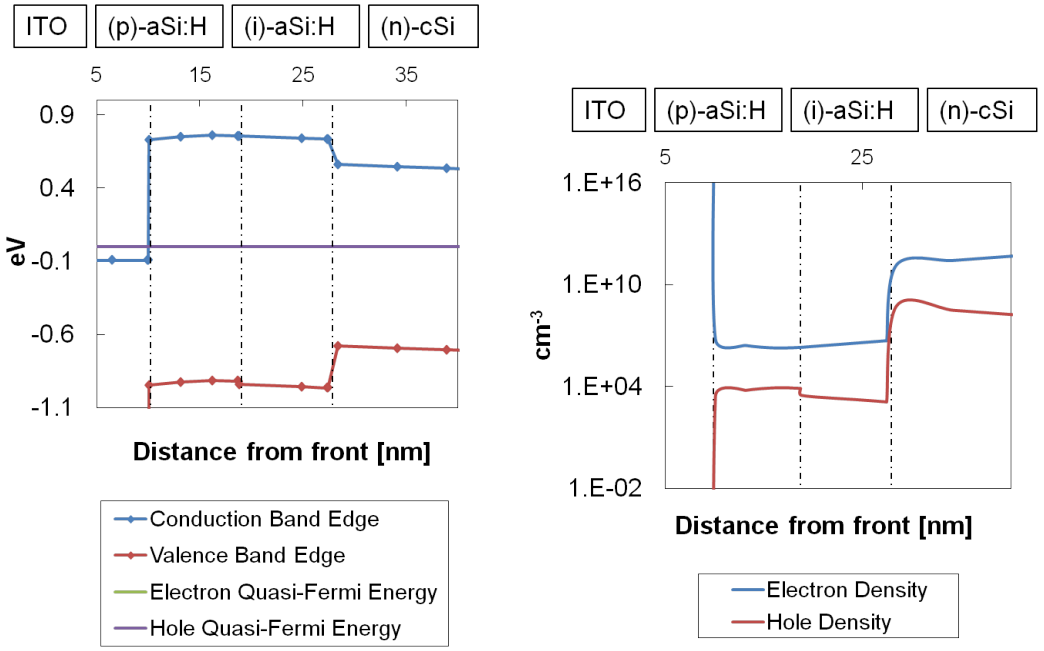

(a) Bands structure

(b) Carriers concentration

Figure 5.21: Simulations for $tp - ti$.

series resistance.

Discussion of simulation

From the simulation shown in Fig. 5.21, the $< p >$ layer results almost completely depleted. This is caused by the large diffusion of holes toward the ITO. Only very few holes are so responsible for diffusing toward the $< i >$ layer and generating the electrical field at the junction (the space charge region is very low). This can be seen by the almost flat bands in the intrinsic layer, see Fig. 5.21 (a).

In this case the holes available in the $< i >$ layer are so few that the concentration of electrons coming from the much less doped (n)-type substrate are dominant.

Having a thin $< i >$ (high resistivity) and a thin $< p >$ layers lower the series resistance. But lots of electrons at the emitter should kill the contact between (p)a-Si:H and ITO, which requires an heavily effective p-type material. This case does not match the experimental data though, since the measures of the *implied* V_{OC} and of the *real* V_{OC} match well. [1]

[1]This topic will not be treated in this thesis.

The almost flat bands lead to a very weak field that slows the carriers and could extend the time needed to reach the front contact , eventually increasing the recombination rate. Thinner $< i >$ layers have also been proved to lead to higher concentration of defects, which itself implies a lower V_{OC}.

2. **Thick (p) - thin (i)** $(Tp - ti)$.

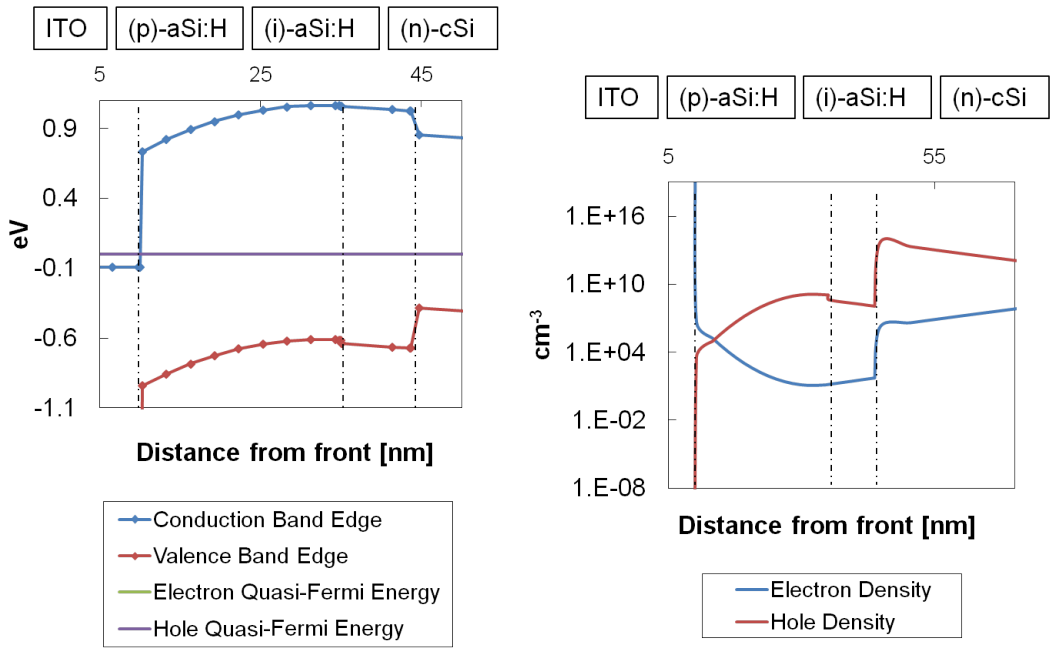

(a) Bands structure

(b) Carriers concentration

Figure 5.22: Simulations for $Tp - ti$.

Real behaviour

The best efficiency has been found in this condition. It shows also good current, good V_{OC} and low series resistance.

Discussion of simulation

It has been said that a thinner $< i >$ layer should decrease the quality of passivation. Why so do we see a good V_{OC} in the experimental results (different from the $tp - ti$)?

The simulation shows that increasing the $< p >$ layer, more holes are provided in the $< i >$ layer, see Fig. 5.22. That implies an increment of space charge region in

the $< p >$ layer, which increases the electrical field in the $< i >$ layer. The more intense field (neglecting phenomenons such as saturation of velocity) can increase the speed of carriers which pass through an higher defect layer in lower time, decreasing the probability of recombination.
The series resistance results low because a $< p >$ layer is not very highly resistive and its expansion does not deeply influence the total series resistance. Also, more carriers diffusing into the $< i >$ layer could decrease the resistivity of the intrinsic layer. Increasing p thickness also leads to a more effective $< p >$ layer because of the less depletion, which could allow a better contact with the TCO.

A comparison of charge density and electrical field for a thick and a thin $< p >$ layer, while keeping the same thin $< i >$ layer is shown in Fig. 5.23 and 5.24.[1]

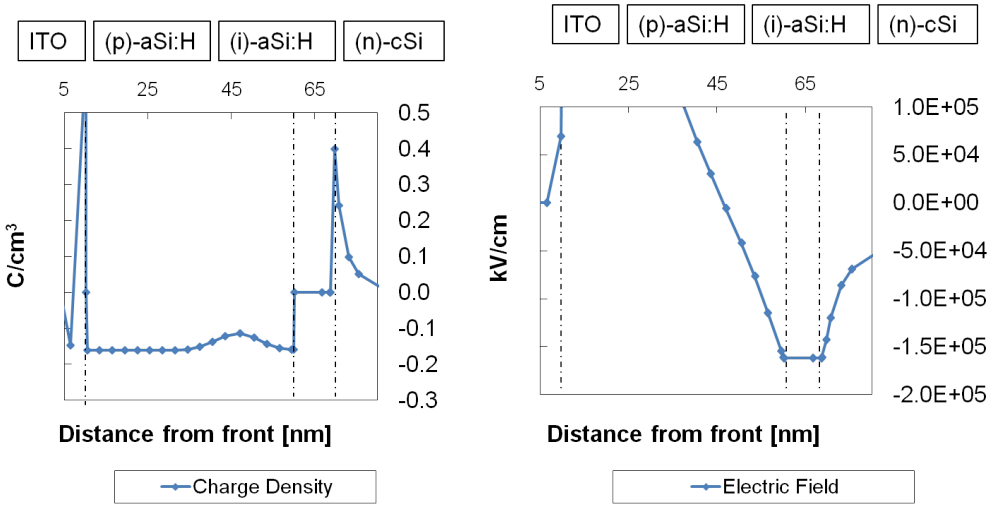

(a) Charge density

(b) Electrical field

Figure 5.23: Simulations for $Tp - ti$.

The figures show an increase of the electrical field with the thicker $< p >$ (from $-2.5 \cdot 10^4$ to $-1.6 \cdot 10^5$ [kV/cm]). The possibly higher amount of defects coming for a thinner and more p-type intrinsic layer, do not imply in this result a reduction of the V_{OC}.

3. **thin (p) - Thick (i)** $(tp - Ti)$.

[1] In this simulation a thick $< p >$ layer has a length of 50 nm.

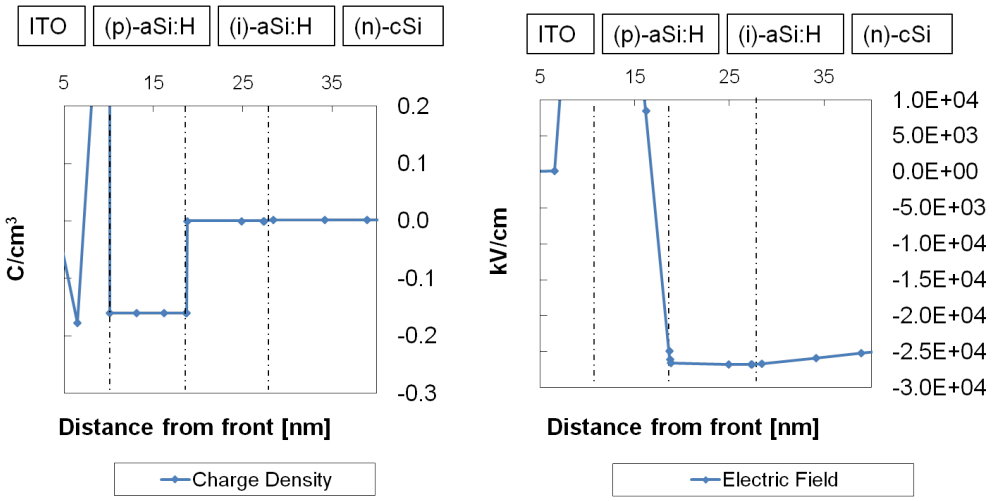

(a) Charge density

(b) Electrical field

Figure 5.24: Simulations for $tp - ti$.

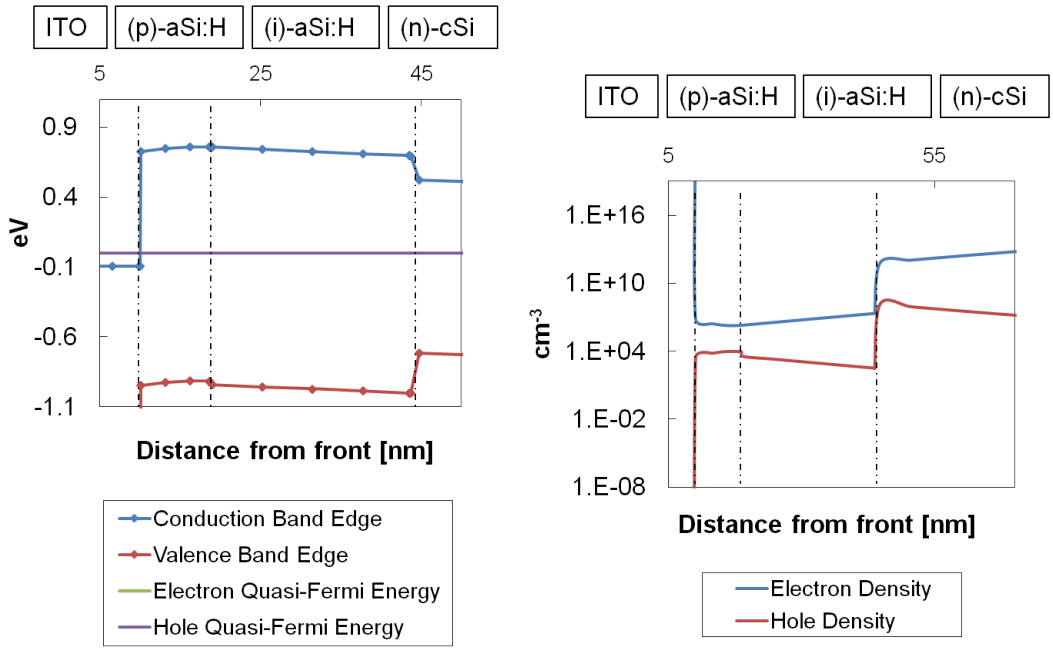

(a) Bands structure

(b) Carriers concentration

Figure 5.25: Simulations for $tp - Ti$.

Real behaviour

Considering a thin $< p >$ layer and increasing the thickness of the intrinsic layer, the series resistance increases, because it expands a region with high resistivity. The V_{OC} also increases in this condition as expected by the better passivation quality that should be achieved with a thicker $< i >$ layer.

Discussion of simulation

From the simulation shown in Fig. 5.25, the majority carriers in the $< i >$ layer are still electrons, because the doped $< p >$ is still very depleted and doesn't provide enough holes in the intrinsic layer.

The better passivation quality that comes from this condition could then be explained by a less number of defects. The simulation tool can't proof the role of defects in the behaviour of the emitter, even though in this case they may be the key to understand the behaviour.

Increasing the thickness of the $< i >$ layer leads normally to a reduction of defects, which is confirmed by the experimental data that show an higher V_{OC}. Decrease of defects can lead to different effects: for example from a different amount of charge trapped into defects state and/or from a lowering of the recombination rate due to a better quality interface between a-Si and c-Si.

4. **Thick (p) - Thick (i) ($Tp - Ti$).**

Real behaviour

This case experimentally provides the best pFF, which comes from the highest V_{OC} and the best passivation quality. Though the series resistance is the highest too.

Discussion of simulation

The thicker $< i >$ layer increases the recombination space, reducing the average carriers in the layer, see Fig. 5.26 (b). Also an increase of thickness inherently rises the series resistance because of the longer path travelled by the carriers.

The benefits that come from less defects (thicker $< i >$) lead to a good V_{OC} while the thick $< p >$ leads to more available carriers which would possibly allow a not too high series resistance.

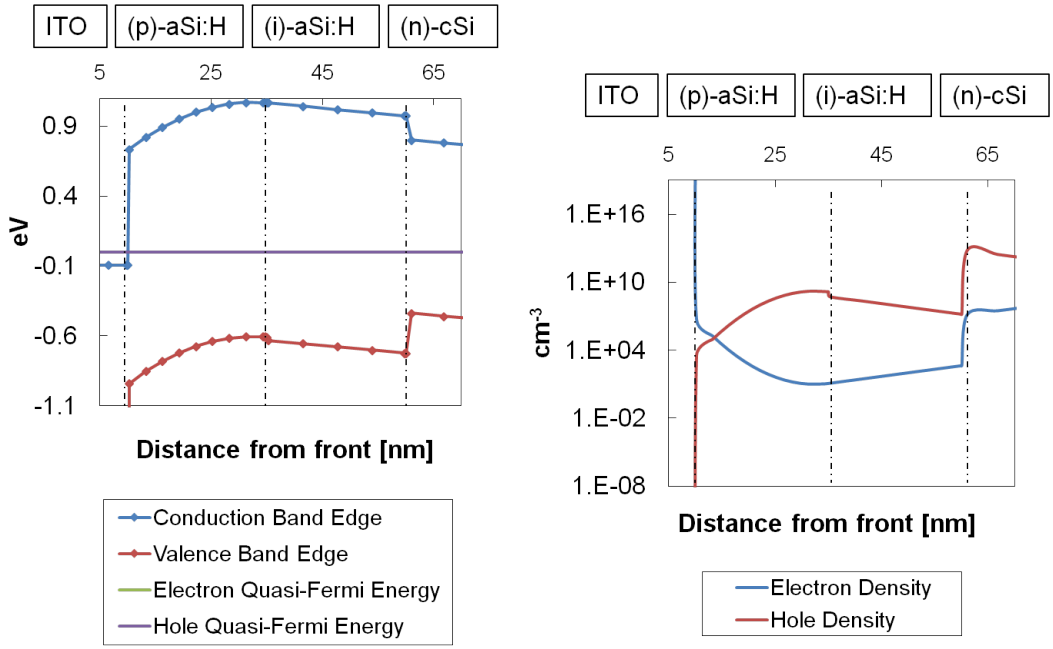

(a) Bands structure

(b) Carriers concentration

Figure 5.26: Simulations for $Tp - Ti$.

5.4.6 Conclusions

It has been seen that:

- A combination of thin $< i >$ and thin $< p >$ does not correctly passivate the cell, leading to a low V_{OC} .
- **Not only the intrinsic layer is responsible for the quality of passivation**. Otherwise $Tp - ti$ should imply a low V_{OC} as $tp - ti$.
  It is known anyway that Fermi level position influence defect concentrations of the $< i >$ layer. Since thicker $< p >$ layers imply a more "p-type" intrinsic layer (as was qualitatively shown with the simulations) the defects concentration should (from literature [12]) increase. Why is then the passivation quality better in this case? Does the higher electrical field induced by the thicker $< p >$ layer help to reduce the recombination probability? Or does the Fermi level position influence positively silicon-hydrogen bondings in this case? We could then say that a more "p-type" $< i >$ layer could also improve the passivation quality until a certain point.

- Thick intrinsic i-layers do not reduce much the short-circuit current, though increasing the series resistance.
- Series resistance can be influenced by $< p >$ carriers diffusion toward $< i >$ layer.
- Best pFF comes from $Ti - Tp$.
- Best efficiency comes from $ti - Tp$.

For the next experiment the optimum for $< p >$ layer is set at 15 nm and a deeper investigation on $< i >$ layer variation will be performed.

5.5 $< i >$ layer influence on FF

From the previous experiment it was found that a $< p >$ layer with a thickness of 15 nm is needed in order to assure the best performance of the cell. It was also found that a thick $< i >$ layer does not hurt the J_{SC} much. Since we had issues regarding metallization, further investigations are performed in order to evaluate how the $< i >$ layer affects the FF. In this experiment this inquiry has been conducted.

5.5.1 Description

The cells are fabricated with:

- variation of the (i)a-Si:H thickness for the front side, see Fig. 5.27 and 5.28 for a qualitative understanding of the experiment variation;
- same condition for all the other parameters;
- monitoring of V_{OC} for testing the passivation quality;
- evaluate overall efficiency with particular interest in FF and series resistance.

The substrate is single side textured, see Fig. 5.29.

The cell is realized following the steps reported in chapter 4. The contacts are made of silver and realized with *screen printing* in both sides. This change has been done since previous experiment showed very good results with this technique ($\eta > 19.7$).

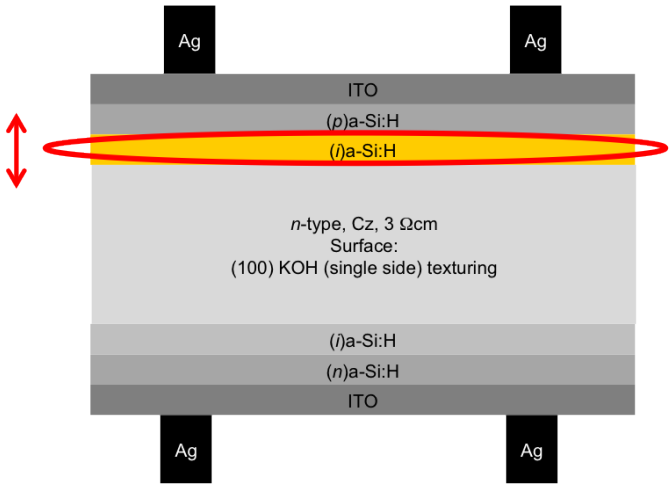

Figure 5.27: Front (i)-aSi:H variation - Schematic cross section of the solar cells fabricated in this experiment.

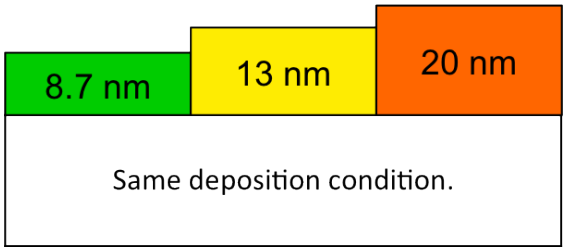

Figure 5.28: Different thickness - Different thicknesses for the (i)a-Si:H layer.

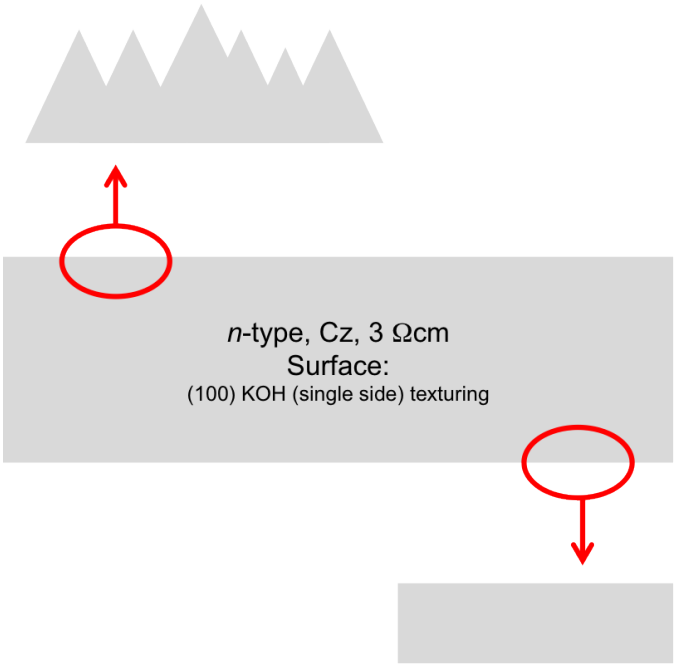

Figure 5.29: Single side - Single side textured substrate used for cell fabrication.

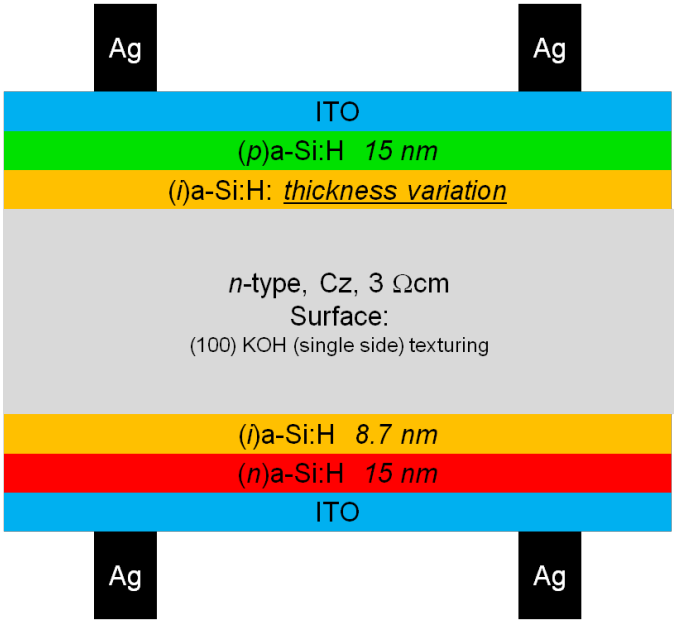

Figure 5.30: Cell structure - Overview of the cell structure in the experiment.

5.5.2 Results

Monitoring of the passivation quality in Fig. 5.31 shows the V_{OC} after: 1) (p)a-Si:H layer deposition (green circles); 2) ITO sputtering and annealing (blue triangles); 3) contact printing (black triangles).

It is possible to see:

1. A lot of V_{OC} scattering after a-Si depositions. This comes from plasma instability which hit the samples on the carrier not homogeneously.

2. Less scattering after annealing ITO, this is caused by thermal healing of the atomic structure.

3. Better passivation with a thicker $< i >$ layer, very clear especially after the (p)a-Si:H depositions (green circles in Fig. 5.31). After metallization, the improvement of V_{OC} with thickness becomes less evident but the trend remains the same. Analysis of FF and cell efficiency becomes now of major importance, especially to compare 13 and 20 nm cells.

FF analysis is shown in Fig. 5.32. The pFF seems to show that the best cell comes from the thickest $< i >$ layer. But FF and efficiency show instead the best value for a thickness of 13 nm, which is also coherent with the increment of series resistance with

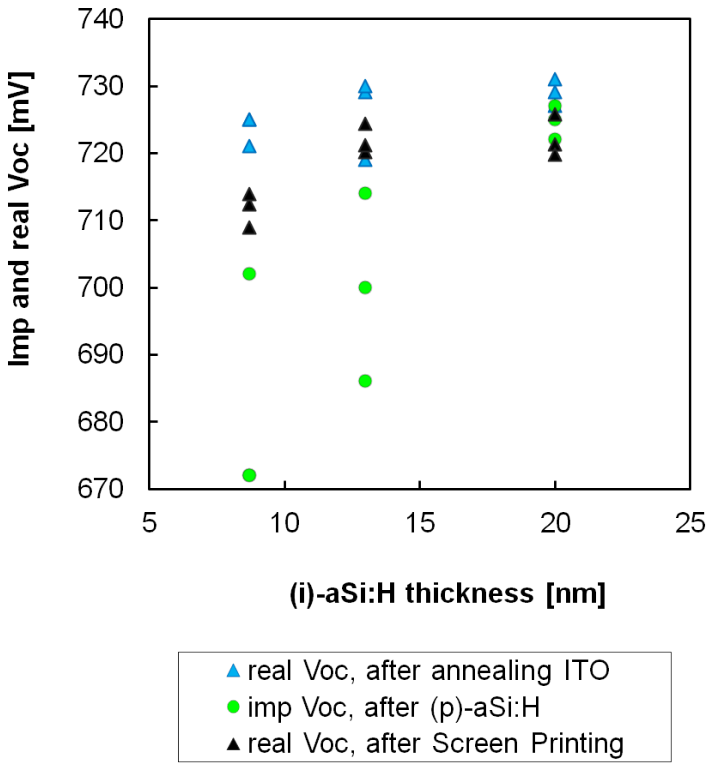

Figure 5.31: V_{OC} **monitoring** - V_{OC} monitoring for different thickness of the intrinsic front a-Si.

i-layer thickness, as shown in Fig. 5.33.
J_{SC} is shown in Fig. 5.34. The short-circuit current is slightly reducing while increasing the thickness of the intrinsic layer.

The pFF is related to the recombination properties of the interface. The thickest i-layer provides the best passivation and therefore produces the highest pFF. The *real* FF includes carrier transport through interfaces/layers. Therefore the FF of thinner layers should be better. Why then isn't the 8 nm layer the best? Because here already the recombination properties (pFF) limits the FF. We can observe that the absolute loss from pFF to FF is larger for 13 nm than for 8 nm, because with 13 nm we have more influence of the carrier transport through the layer (that can clearly be seen in the R series plot).
Why is 13 nm the best efficiency? The V_{OC} is nearly as good as for the 20 nm, the current is in the middle and the FF is the best. Why is the FF the best? Because the FF is a mix of pFF (e.g. recombination properties) and R_{series}. And the mix of these two aspects is the best for the 13 nm.

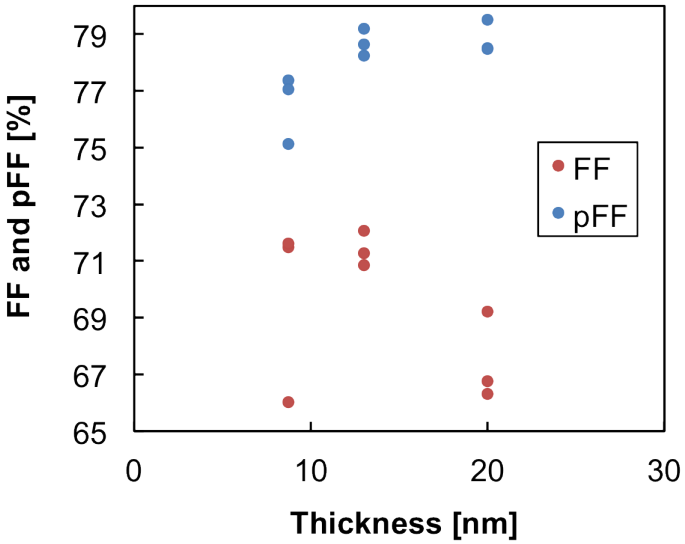

Figure 5.32: FF and pFF - Overview of FF and pFF in function of the thickness.

5.5.2.1 Considerations on screen printing

Some samples were affected by screen printing instabilities, i.e. interrupted fingers in the rear side and twisted fingers in the front side, see Fig. 5.35. The effects of those imperfections are not very clear, since samples unaffected show values of series resistance

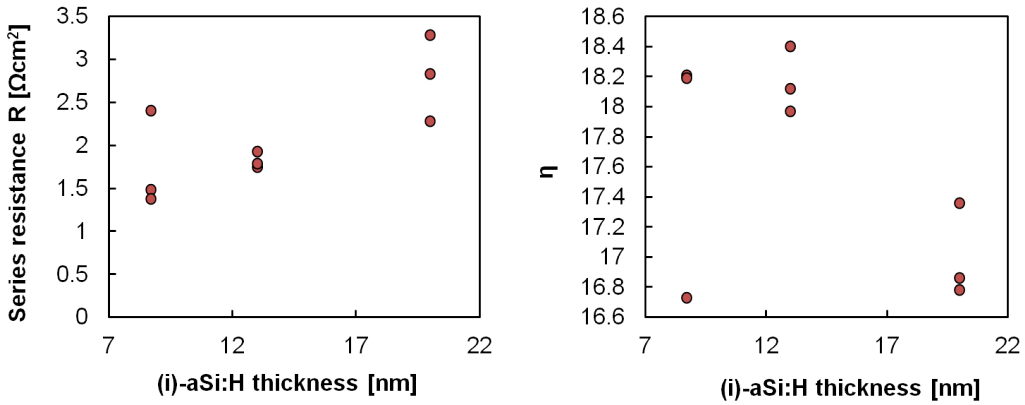

(a) Series resistance.

(b) Efficiency.

Figure 5.33: Analysis of the cells performance and series resistance.

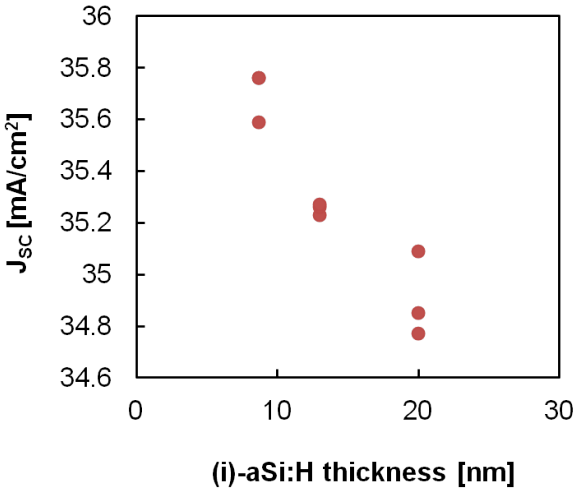

Figure 5.34: J_{SC} - J_{SC} overview in the FF.

similar to those affected. Anyway, to avoid wrong interpretations we do not consider imperfect samples.

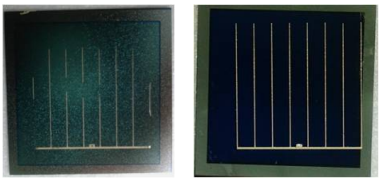

(a) Interrupted fingers (rear). (b) Twisted fingers (front).

Figure 5.35: Screen printing problems.

5.5.2.2 Series resistance analysis

Through the methods explained in section 3.2.4, it is possible to calculate the series resistance R as a function of voltage V. An example of the graph obtained is shown in Fig. 5.36. Those curves represent the values of resistance in function of voltage for the *same cell*, but with the different methods presented in section 3.2.4. We observe that the different methods accord very well with each other (except Double light). It is known that these methods to determine the R_{series} should not be applied for voltages lower than 300 mV.[1]

Once the calculation of $R = f(V)$ is provided for different samples (i.e. for different (i)a-Si thicknesses), it is possible to obtain R as a function of voltage V and thickness d (Figure 5.37 c):

$$R(V, d) \tag{5.2}$$

Figure 5.38 shows a schematic presentation of the way the graph is constructed.

In Fig. 5.37 (c) the series resistance is shown for different samples (different thickness of $< i >$ layer) for different voltages: each variation in the thickness correspond to a different sample, as explained in Fig. 5.37 (a) and (b). It appears that the series resistance increase with $< i >$ layer thickness and decrease while increasing the voltage applied. The resistance curves come from $Light - J_{SC}V_{OC}$ method. This choice can be modified with another method or with an average.

[1] J-V curve tends to become flat for low voltage and this may influence the comparison between different curves.

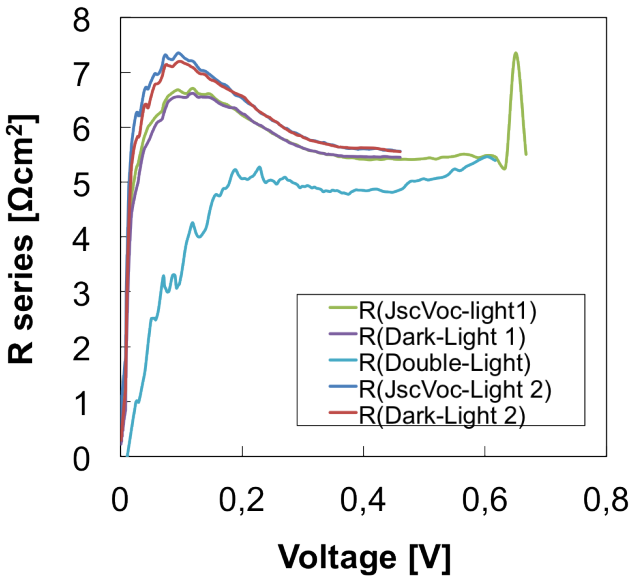

Figure 5.36: Series resistance - Series resistance calculated from different methods as a function of voltage.

5.5.2.3 Model evaluation

In order to proceed with the development of a model to estimate the contribution of the $< i >$ layer on the series resistance, some assumptions have to be done:

1. Series resistance is given by a sum of 2 different contributions:

$$R_S(V,d) = R_{<i>}(V,d) + R_{rest}(V) \tag{5.3}$$

where V is the voltage, d is the thickness of the $< i >$ layer, R_S is the series resistance measured, $R_{<i>}$ is the front $< i >$ layer contribution to the total resistance and R_{rest} is the resistance that comes from all the other contributions (this latter should not change with the variation of the thickness of the intrinsic a-Si layer!). Note that all the resistance are [Ωcm^2]. A qualitative presentation of eq. 5.3 is shown in Fig. 5.39.

2. The influence of $< i >$ thickness into $R_{<i>}$ is linear, so that:

$$R_{<i>}(V,d) = \rho_{<i>}(V) \cdot d \tag{5.4}$$

where d is still the thickness of the $< i >$ layer. In this way, $\rho_{<i>}(V)$ is the slope of the curves presented in Fig. 5.37 (c).

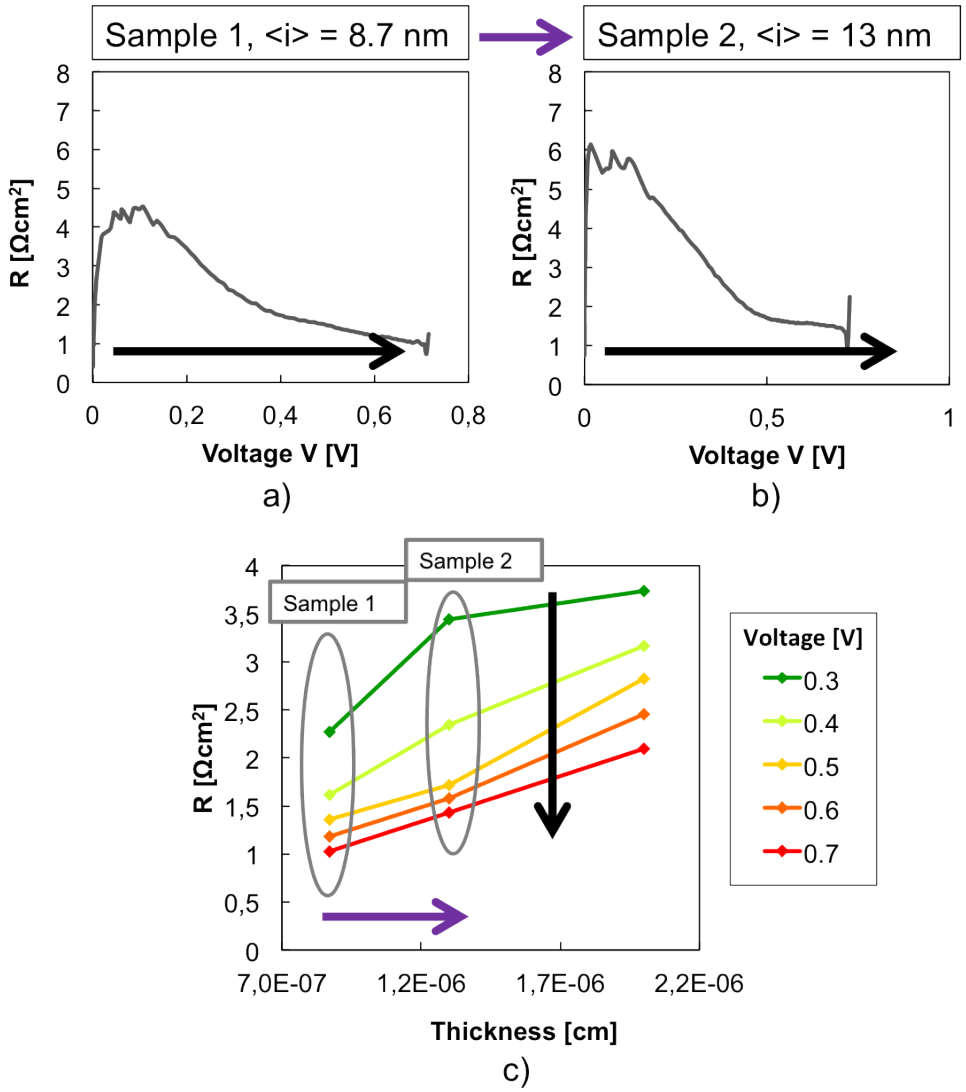

Figure 5.37: $R(V, d)$ - Method used to calculate the series resistance in function of voltage and thickness.

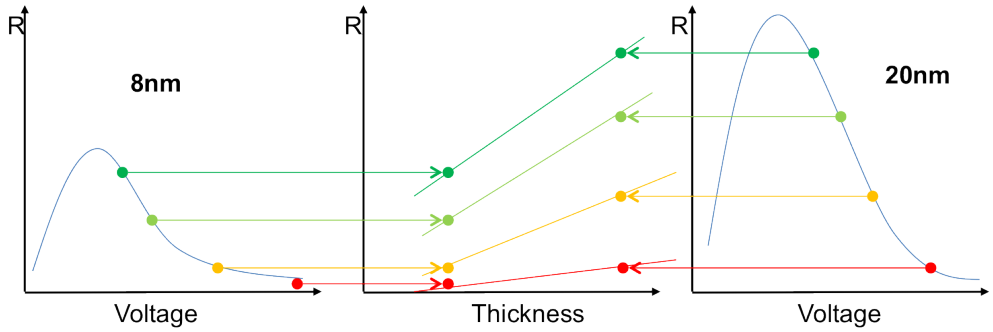

Figure 5.38: $R(V, d)$ **qualitative** - A schematic presentation of the series resistance as a function of voltage and thickness.

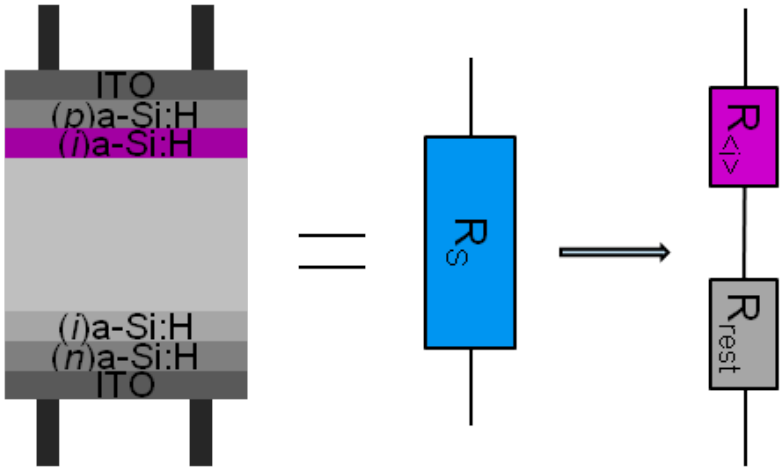

Figure 5.39: Resistance model - A graphic representation of the model used to describe the resistance contributions.

In fact, it is possible to consider:

$$\rho_{<i>}(V) = \frac{R_S(d_2,V) - R_S(d_1,V)}{d_2 - d_1} = \frac{R_{<i>}(d_2,V) + R_{rest}(V) - R_{<i>}(d_1,V) - R_{rest}(V)}{d_2 - d_1} \rightarrow \tag{5.5}$$

$$\rho_{<i>}(V) = \frac{R_{<i>}(d_2,V) - R_{<i>}(d_1,V)}{d_2 - d_1} = \frac{\rho_{<i>}(V)\cdot(d_2 - d_1)}{d_2 - d_1} \tag{5.6}$$

where d_1 and d_2 are two different values of thickness for the intrinsic layer. This value for ρ gives an estimate of the resistivity in the $< i >$ layer, and of the conductivity:

$$\sigma_{<i>}(V) = \frac{1}{\rho_{<i>}(V)} = q \cdot \mu(V) \cdot carriers(V) \tag{5.7}$$

where q is the elementary charge and μ is the mobility of the carriers, as a function of voltage.

From the previous statements, one should expect that the resistivity does not depend on the $< i >$ layer thickness of the samples. Through eq. 5.5, since $R_S(d,V)$ is measured, it is possible to estimate $\rho_{<i>}(V)$, which unfortunately change with the thickness chosen, see Fig. 5.40.
We remark that low voltages (i.e. less than 300-400 mV) should not be considered. The following check of consistency confirms this requirement.

This behaviour is anyway expected:

1. a variation of the $< i >$ layer changes the position of the Fermi level, causing different hydrogen bondings and defect concentration;

d_1 [nm]	d_2 [nm]	d_3 [nm]
8.7	13	20

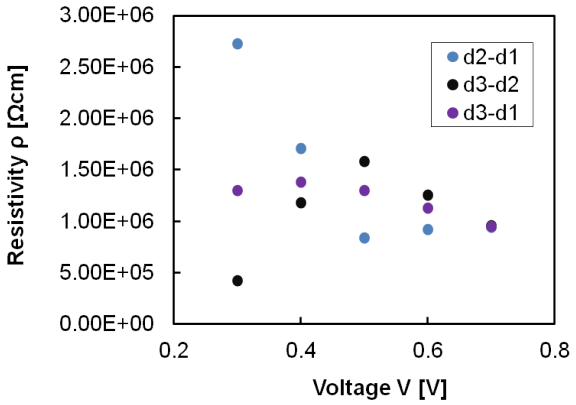

Figure 5.40: Consistency of ρ - Checking the consistency of the model for ρ. For the same voltage, the 3 points should coincide.

2. this causes a possible change of carrier concentrations in the transport bands, especially for low voltage when intrinsic carriers are much dominant;

3. influence of different carrier concentrations in the transport bands on mobility $\rightarrow \mu(V, d)$.

It is appropriated to modify eq. 5.7 in:

$$\sigma_{<i>}(V, d) = q \cdot \mu(V, d) \cdot carriers(V, d) \tag{5.8}$$

This is actually coherent with the previous considerations regarding the experiment of (i) and (p) variation thickness, namely how changing of the thickness affects the carrier concentrations in the high resistive intrinsic region. To avoid this problem **low voltage values are neglected**, considering excess carriers injected dominant respect carriers coming from other contributions.

Another check of consistency comes from eq. 5.3, which for clearness is reported here:

$$R_S(V, d) = R_{<i>}(V, d) + R_{rest}(V) \tag{5.9}$$

From the model, the term R_{rest} should be independent from the thickness of the $< i >$ layer. It is also possible to estimate the value of $R_{<i>}(d, V)$ from $\rho_{<i>}(V)$. Taking into account eq. 5.4 in fact:

$$R_{<i>}(V, d) = \rho_{<i>}(V) \cdot d \tag{5.10}$$

and

$$R_{rest}(V) = R_S(V,d) - \rho_{<i>}(V) \cdot d \tag{5.11}$$

where $R_S(V,d)$ is measured while $\rho_{<i>}(V)$ is estimated. The result for an 8.7 nm sample is shown in Fig. 5.41.

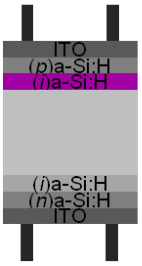

8.7 nm

V	R_S	$R_{<i>}$	R_{REST}
0,4	1,61	1,25	0,36
0,5	1,36	1,05	0,31
0,6	1,18	0,94	0,24
0,7	1,03	0,82	0,20

Figure 5.41: Check of consistency R_{REST} - Terms that in the model developed form the total series resistance.

R_{rest} is a small part of the total resistance compare to $R_{<i>}$. In this case also, the term R_{rest} includes an (i)-aSi on the rear which has the same thickness of the front. A way to explain this much smaller value is taking into account the fact that in the rear side, electrons are transporting the charge, which have higher mobility; also, the lower gradient between n-N junction cause less diffusion, which means less depletion and even more carriers in the $< i >$ layer. Further investigations which should measure the ITO and contact resistance contribution should be performed, in order to better evaluate a real value for R_{REST} to compare with the estimated one.

From eq. 5.7 the values of the average conductivity in the $< i >$ layer for different voltages are shown in Fig. 5.42. An increment of intrinsic conductivity comes while increasing the voltage. This can be explained thanks to the increment of carriers injected.

Aware of the previous issues regarding $\rho_{<i>}$ dependence from thickness, it is possible to make further estimations, but not much reliability is still guaranteed. Only voltages above 0.4 V are considered.

If conductivity is considered:

$$\sigma_{<i>} = q \cdot \mu_{<i>} \cdot carriers_{<i>} \tag{5.12}$$

where q is the elementary charge and $\mu_{<i>}$ is a fixed mobility for the carriers. Since $\sigma_{<i>}$ is already been calculated, it is possible to estimate the carriers concentration when fixing

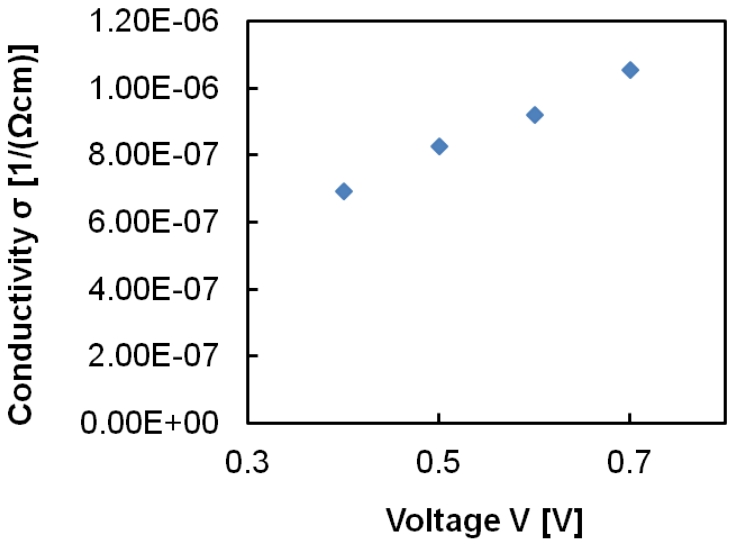

Figure 5.42: σ_i for different voltage - Average σ_i for different voltage.

the value of mobility μ.
More in details, considering that the main carriers in the (i)-aSi come from the $< p >$ layer:

$$\sigma_{<i>} = q \cdot \mu_p \cdot (\Delta p + p_0) \tag{5.13}$$

where

$$\Delta p = -\frac{p_0}{2} + \frac{1}{2}\sqrt{p_0^2 - 4n_i^2(1 - \exp\left(\frac{qV}{kT}\right))} \tag{5.14}$$

and p_0 is the intrinsic holes concentration and Δp are the excess carriers which are injected from the contacts. If eq. 5.5.2.3 is inserted into eq. 5.13, and if values for n_i and for μ_p are set, it is then possible to solve the equation in function of p_0. We chose values for $n_i = 10^6$ cm$^-$3 and for μ_p =5 cm/(Vs). A changing of these values cause a linear change of the values of p_0 estimated, so this cannot be considered precise, but the order of magnitude is still reasonably maintained.

From Fig. 5.43 average p_0 concentration in the intrinsic aSi layer is on the order of 10^{12}, while the excess carriers injected change from 10^5 to about 10^{12}.

5.5.2.4 Further considerations

The following considerations are not enough proved but are possibly cues for next investigations.

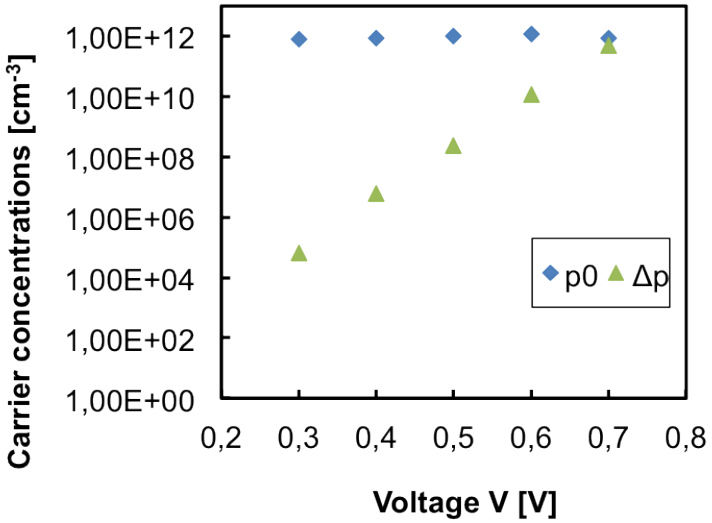

Figure 5.43: Estimate of p_0 and Δp - Estimate of p_0 and Δp for different voltage.

The measured data are not fully understood yet and a deeper analysis could help understanding better the physical behaviour of the cell. For example:

1. dependence of mobility from voltage;
2. influence of intrinsic layer thickness into the term R_{rest}, see eq. 5.3;
3. influence of light excess carrier and intrinsic carriers concentration into R dependence from voltage;

are only a few examples of features which are not very well understood.
For the last point in particular, the graph presented in Fig. 5.36 (which for convenience is reported below) could contain some interesting hidden informations. Two trend can be seen in this graph:

- **Dependence of series resistance from voltage**. Some graphs which clearly show the possible different behaviours of the series resistance are shown in Fig. 5.45, 5.46, together with Fig. 5.44. That means that the series resistance changes its dependence with the voltage. The effects of applying a voltage are several, we could consider a changing of the injected carriers as the main effect. As a consequence a more or less flat curve $R = f(V)$ could mean a more or less influence of the injected carries into the total resistance. The less dependence could be caused by an amount of intrinsic carrier concentration which is dominant respect to the injected carriers. The reason for having more intrinsic carriers is not clear yet since

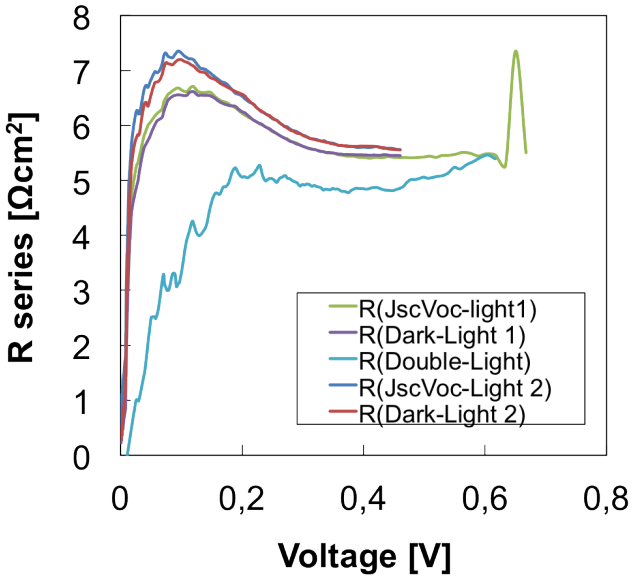

Figure 5.44: Series resistance - Series resistance calculated from different methods as a function of voltage.

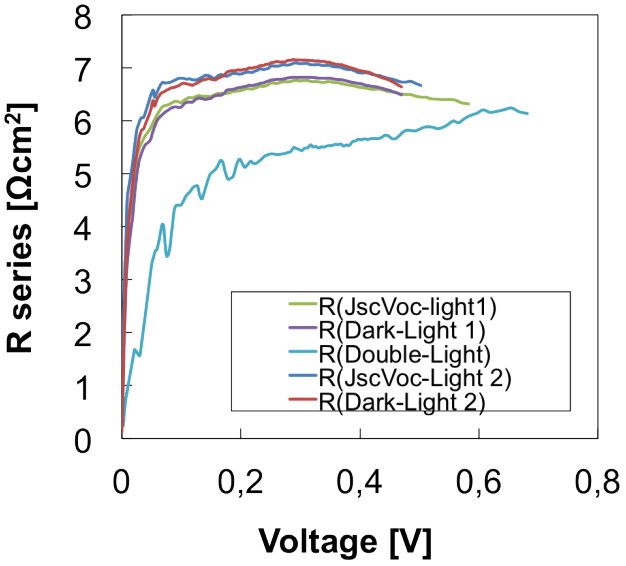

Figure 5.45: Series resistance - Series resistance calculated with different methods as a function of voltage.

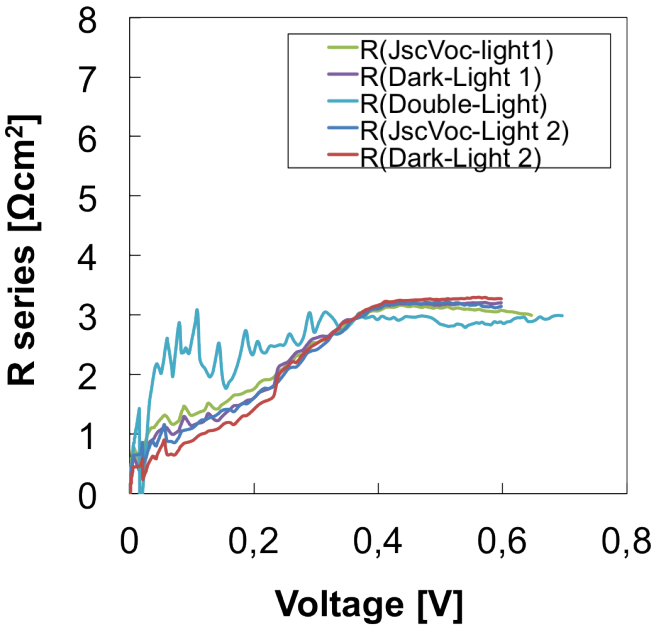

Figure 5.46: Series resistance - Series resistance calculated with different methods as a function of voltage.

no correlation of this dependence has been found with any particular condition, i.e. those trends appear to be random at the moment. The different dependence trends are more evident for lower voltages, in fact after a certain voltage the curve $R = f(V)$ appears to be more "flat". This could prove that the injected carriers become dominant in every condition after a certain voltage.

- Figure 5.44 shows an abrupt increment of the series resistance for low voltages, then it slightly decreases until arranging at values around 5 Ωcm^2;
- Figure 5.45 shows an abrupt increment of the series resistance for low voltages, then the curve appears to be quite flat, assuming values around 5-6 Ωcm^2;
- Figure 5.46 shows a light increment of the series resistance for low voltages, which then stabilizes at a value around 3 Ωcm^2.

- **Dependence of series resistance from light effects**. The different curves in Fig. 5.44, 5.45 and 5.46 appear to be more or less overlap and this congruence of the different methods used changes also in function of the voltage. Since the different methods use a comparison of curves calculated in light and dark conditions, the reason for having less coherence between those methods could come from light effects. It is known in fact how carriers injected and photogenerated could follow

different paths, see Fig. 5.47. The series resistance could then have different values. In this simplified picture, ITO should be the most effective cause for the different trends. More investigations could prove this or other statements.

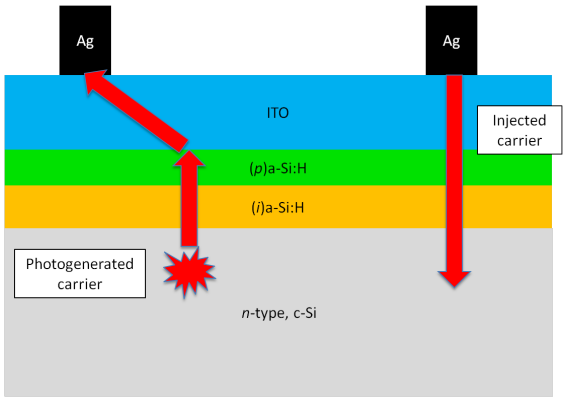

Figure 5.47: Different paths - Light effects into different paths.

5.5.3 Conclusions

Resuming, what we see from this experiment is that:

- $< i >$ layer thickness deeply influence current and series resistance. Even though V_{OC} and passivation quality seems to benefit less after a certain thickness, which is found to be around 20 nm.
- Conductivity of $< i >$ layer increases with voltage.
- The model presenting the average conductivity of $< i >$-layer is still very rough and needs refinement.

6

Conclusions

HIT solar cells offer great potential. The heterojunction advantages, the possible low cost process and the high efficiency which has been proved clearly confirm their value. The heterojunction still needs a deeper understanding that makes possible a more optimized use of the different layers which can give beneficial effects to the overall cell performance. The thickness of the intrinsic and (p)-doped a-Si:H layers deeply influence the quality of passivation and the transport properties.

Thickness of (p)-type amorphous silicon seems to influence the passivation quality of the heterojunction. A more effective p-type intrinsic layer (e.g. less depleted and/or more effectively doped) is expected to lead to more defects and worse passivation, since a Fermi energy position closer to the valence band has been proved to negatively influence hydrogen bondings. Previous experiments performed at the ISFH showed worse performance using thicker p layers. A positive influence from a thicker p-type must also be considered anyway. Analysing the carriers concentration of the simulations, a thicker $< p >$ layer seems to lead to more carriers in the intrinsic layer together with an higher electrical field. We can say that two different phenomenons influence the passivation quality and that they act differently in function of the different thickness of the layer. An optimal for the p layer must be close to 15 nm for the cell fabricated.[1].
We find optimal gas flux parameters for the deposition of the (p)a-Si:H layer.

An optimal thickness for the front (i)-aSi:H layer has been found. Below the optimum the open circuit voltages V_{OC} are still good but they can be improved sensibly with increasing the thickness. The enhancement is more evident for lower thickness. Series

[1]Different parameters during the deposition process such as temperature, hydrogen concentration etc, could very well lead to another optimal condition

resistance and J_{SC} have a quite constant dependence from the thickness of the $< i >$ layer (even if current has a much lower slope). An optimum appear to be at 15 nm ca. We present a rough model to estimate the conductivity of the intrinsic a-Si layer. We find that the conductivity is voltage dependent. The model allows also a calculation of the (excess) carrier concentration in the (i)-aSi:H layers.

The H_2 plasma post treatment does not improve the passivation quality of our cells. Oxygen bonding in the amorphous silicon network is not excluded after an HF treatment.

.

Bibliography

[1] R. Zallen.
The Physics of Amorphous Solids.
John Wiley, 1998. 6

[2] R. A. Street.
Hydrogenated Amorphous Silicon.
Cambridge University Press, 1991. 6, 7, 8, 9, 11

[3] M. A. Lieberman, A. J. Lichtenberg.
Principles of Plasma Discharges and Materials Processing.
Wiley, 2005. 12

[4] W. Luft , Y. Simon Tsuo Y.
Hydrogenated amorphous silicon deposition processes.
Marcel Dekker Inc., New York, 1993. 12

[5] J.P.M. Schmitt.
Fundamental mechanisms in silane plasma decompositions and amorphous silicon deposition.
Journal of Non Cryst. Solids 59-60, 649-457, 1983. 13

[6] J.P.M. Schmitt.
Towards high deposition rates of a-Si:H, the limiting parameters.
Journal of Non Cryst. Solids 37, 164-166, 1993. 13

[7] E. Amanatides, S. Stamou, D. Mataras.
Gas phase and surface kinetics in plasma enhanced chemical vapor deposition of microcrystalline silicon: The combined effect of rf power and hydrogen dilution.
Appl. Phys. 90, 5786-5798, 2001. 13

[8] P. Crouch, D. Martin.
Low energy electron-enhanced etching of Si(100) in hydrogen/helium direct-current plasma.
Appl. Phys. Lett. 66, 2476, 1995.

[9] Bouchoule.
Dusty Plasmas: Physics, Chemistry, and Technological Impacts in Plasma Processing.
Wiley, New York. 1999

[10] A. Kroely, R. Cabarrocas.
Negative corona discharge: application to nanoparticle detection in RF reactors.
Plasma Sources Sci. and Technol. 18, 015005, 2009.

[11] M. Stutzmann, D. K. Biegelsen, R. A. Street.
Detailed investigation of doping in hydrogenated amorphous silicon and germanium.
Physical review B, volume 35, number 11, 1987. 17, 18, 70

[12] T. Schulze.
Structural, electronic and trasport properties of amorphous/crystalline silicon heterojunction.
Helmholtz Zentrum Berlin, 2011. 14, 23, 91

[13] J.C. Knights.
Unknown title.
Japanese Journal of Applied Physics, 18:101, 1979. 16

[14] SintonInstruments User Manual.
WCT-120 Photoconductance Lifetime tester and Optional Suns- Voc, 2012.

[15] SintonInstruments User Manual.
WCT-120 Photoconductance Lifetime tester and Optional Suns- Voc, 2012. 25

[16] F. Dannhauser.
Unknown title.
Solid State Elec. Vol. 15, pp- 1371-1381, 1972.

[17] J. Krausse.
Unknown title.
Solid State Elec. Vol. 15, pp- 1377-1381, 1972.

[18] Kane, D E and Swanson, R M.
Measurement of the emitter saturation current by a contactless photoconductivity decay method.
Las Vegas : s.n. Proc. 18th IEEE PVSC, pp. 578-583, 1985.

[19] Altermatt, Heiser, Aberle, Wang, Zhao, Robinson, Bowden, Green.
Spatially Resolved Analysis and Minimization of Resistive Losses in High-eficiency Si Solar Cells.
Progress in photovoltaics: research and applications. Vol. 4, 399-414, 1996. 31

[20] A. Descoeudres, L. Barraud, Stefaan De Wolf, B. Strahm, D. Lachenal et al.
Improved amorphous/crystalline silicon interface passivation by hydrogen plasma treatment.
Published by the American Institute of Physics. Applied physics letters 99, 123506 (2011) 61, 65

[21] Schmitt, J.P.M.:
Fundamental mechanisms in silane plasma decompositions and amorphous silicon deposition.
J. Non Cryst. Solids 59-60, 649-657 (1983) 13

[22] Wikipedia: solar cell efficiency. 2

[23] Sanyo news.
http://us.sanyo.com/News/SANYO-Develops-HIT-Solar-Cells-with-World-s-Highest-Energy-Conversion-Efficiency. 1, 3

[24] M. I. Kabir, Z. Ibarahim, M. Alghoul, K. Sopian, M. R. Karim, N. Amin.
Bandgap optimization of absorber layers in amorphous silicon single and multijunction junction solar cells.
Chalcogenide Letters Vol. 9, No. 1, p. 51 - 59, 2012. 5

[25] G. Heiser, A. G. Aberle, A. Wang, J. Zhao, S. J. Robinson, S. Bowden, M. A. Green.
Spatially Resolved Analysis and Minimization of Resistive Losses in High-eficiency Si Solar Cells.
Progress in photovoltaics: research and applications. Vol 4, 399-414, 1996. 34

[26] R.A. Sinton, A. Cuevas.
A Quasi-Steady-State Open-Circuit Voltage Method for Solar Cell Characterization.
16th European Photovoltaic Solar Energy Conference, 2000. 25

[27] Dorkel
Carrier mobilities in silicon semi-emirically related to temperature, doping and injection level, solid state electron.
1981. 27

[28] G. Wilfried, M. Van Sark, L. Korte, F. Roca Physics and Technology of Amorphous-Crystalline Heterostructure Silicon Solar Cells.
2012 12, 14, 15, 20, 21

[29] C. Bittencourt, F. Alvarez.
Amorphous Silicon and its Alloys, chapter 3.8, pages 174-179.
INSPEC, edited by T. Searle, 1998. 21

[30] L. Korte, T. F. Schulze, C. Leendertz, M. Schmidt, B. Rech.
Band alignment at amorphous/crystalline silicon hetero-interfaces.
In Amorphous and Polycrystalline Thin-Film Silicon Science and Technology, volume 1321 of MRS Symposia Proceedings, pages A15-03, 2011. 21

[31] F.A. Rubinelli.
Amorphous-crystalline silicon anisotype heterojunctions: Built-in potential, its distribution and depletion widths.
Solid-State Electronics, 30(3):345-351, March 1987. 21

[32] M. A. Green.
Solar Cells Operating Principles, Technology and System Application.
The University of New South Wales, 1992. 22

[33] U. K. Das, M. Z. Burrows, M. Lu, S. Bowden, and R. W. Birkmire.
Surface passivation and heterojunction cells on Si (100) and (111) wafers using DC and RF plasma deposited Si:H thin films.
Applied Physics Letters, 92:063504-3, 2008. 22

[34] D. Diouf, J.P. Kleider, T. Desrues, and P.J. Ribeyron.
2D simulations of interdigitated back contact heterojunction solar cells based on n-type crystalline silicon. physica status solidi (c), pages 1033-6, 2010.

[35] U. Das, M. Lu, D. Xu, O. Jani, S. Bowden, S. Hegedus, and R. Birkmire.
Designing Rear Surface for Carrier Transport in all back contact silicon heterojunction solar cells.
In Proceedings of 18th Photovoltaic Solar Energy Conference, Kolkata, India, pages 1283-6, 2009. 22